# Polytechnic of Turin



College of Chemical and Materials Engineering
Master's Degree Program in Materials Engineering for Industry 4.0
Academic year: 2024/2025

# Microstructural Analysis and Modelling for an additively manufactured Nickel-Based superalloy for Gas Turbine applications

Thesis supervisor: Candidate:

Prof. Daniele Ugues Dr. Rocco Rubino

Prof. Emilio Bassini

# Index

Chapter 1	12
1.1 General theory about Superalloys Errore. Il segnalibro non è	definito.
1.1.1 Strenghtening mechanismErrore. Il segnalibro non è	definito.
1.2 Ni and Ni-based Superalloys	16
1.2.1 Alloying elements used in Ni-based superalloys	18
1.3 Microstructures in Ni-based Superalloys	20
1.3.1 γ phase matrix	21
$1.3.2 \gamma'$ - $Ni3(Al, Ti)$	22
1.3.3 γ" - Ni3Nb	24
1.4 Carbides	24
1.5 Borides	25
1.6 Topologically Close-Packed Phase	26
2.1. Metal Additive Manufacturing	28
2.1.1. Laser Powder Bed Fusion	29
2.2. Laser powder bed fusion of difficult to print $\gamma'$ Ni-based superalloys	34
2.2.1. Defect formation during LPBF of γ' Ni-based superalloys	35
2.2.2. Melt Pool	37
2.3. Approaches to PBF-LB of γ' Ni-based superalloys	43
2.3.1. Effect of PBF-LB process parameters on cracking density	43
2.3.2. Post Processing on micro-cracking defects	45
2.3.3. Effect of chemistry modification on cracking density	47
2.3.4. Chemistry modification in Inconel 738LC	48
2.3.5. The material object of this work	51
Chapter 3 . Materials and Methods	54
3.1. LPBFed SAM	54
3.2. Metallographic preparation of samples	54
3.3. Optical Microscope	55
3.3.1 Grain Size Analysy Errore, Il segnalibro non è	definito

3.4. Scanning Electron Microscopy (SEM)	57
3.5. Melt Pools Analysis	57
3.6. Differential Scanning Calorimetry (DSC)	58
3.7 Electron Backscatter Diffraction (EBSD)	59
Chapter 4. Microstructural Analysis	61
4.1 Phenomenological analysis of microstructure	61
4.1.1 Cubic Samples-Porosity	61
4.1.2 Cubic Samples- Microstructure	66
4.1.3 Cubic Samples-Melt pool	74
4.1.5 Coal Cart Samples-Microstructure	85
4.1.5 Coal Cart Samples-Melt pool	89
4.2 Quantitative analysis of microstructure	91
Chapter 5. Conclusion	98

# **Index of figure**

Figure 1: Classification of Superalloys	13
Figure 2: ultimate tensile stress (UTS) comparison among Superalloys [3]	14
Figure 3: Ni face centred cubic structure (FCC) [3]	16
Figure 4: alloying elements used in Ni-based superalloys	18
Figure 5: schematic of microtructure in $\gamma$ 'Ni-base superalloys after solution heat treatments	atment
above the $\gamma'$ solvus and aging [14] Errore. Il segnalibro non è de	finito
Figure 6: process stesp and schematic of the LPBF [23]. Errore. Il segnalibro non è de	finito.
Figure 7: schematic illustration of the key process parameters	32
Figure 8: main scanning patterns in a single layer. (a) undirectional scanning, Errore.	I
segnalibro non è definito.	
Figure 9: Factors contributing to solidification cracking	36
Figure 10: thermal phenomena occurring during LPBF	39
Figure 11: cross section view of single track simulation showing the temperature and vo	elocity
field of the melt pool as the laser scans.	40
Figure 12:schematic illustration of heat transfer history for a (a) conduction mode and (	b) key
hole mode	41
Figure 13: relationship between temperature gradient, solidification rate and the resulting	g grain
size and morphology of a solidifies microsturcture [41], [42]Errore. Il segnalibro	non è
definito.	
Figure 14: effect of VED on crack density for IN738LC.	44
Figure 15: Change of phase transformation and liquid phase mass fraction with resp	ect to
temperature for IN738LC(a), IN738LC+1%Hf(b), IN738LC+2%Hf(c) calculate	ed by
ThermoCalc, (d) the liquid phase fraction in the last 15% liquid of three composition [58]	8]49
Figure 16: The Scheil-Gulliver solidification curves for IN738LC, IN738LC+	1%Hf
IN738LC+2%Hf (a), and the solid phase fraction in the last 10% liquid of three compe	osition
(b) [58]	50
Figure 17: Metallography of as printed IN738LC (a), IN738LC+1%Hf (b)	, and
IN738LC+2%Hf (c)	50
Figure 18: schematic representation of the coal cart SAM built along the building direct	ion. 54
Figure 19: cross section showing typical defects in INCONEL738LC samples. (a) Formed	l crack
located at grain boundaries, (b) gas pore, (c) lack of fusion, (d) oxide inclusion [46]	56
Figure 20: microstructure of the as-built SAM cubic samples	62

_	re 45: Density distribution of pore diameters for samples 39, 37, and 32 along the XZ plan
	re 46: Optical micrographs of the grain structure of sample 37 (HIP) observed along the
XY	and XZ planes
Figu	re 47: Optical micrographs of the grain structure of sample 32 (HIP+SolHT+Age) observe
alon	g the XY and XZ planes
Figu	re 48: SEM micrographs of sample 39 (as built): thin wall observed on the XZ plane, deta
of th	e thin wall, and thick wall in the central region
Figu	re 49: SEM micrographs of sample 37 (HIP): thin wall observed on the XZ plane, deta
of th	e thin wall, and thick wall in the central region
Figu	re 50: SEM micrographs of sample 32 (HIP+SolHT+Age): thin wall observed on the X
plan	e, detail of the thin wall, and thick wall in the central region
Figu	re 51: comparison between the indivual melt pool profiles (grey) and the average profi
(red)	of sample 39, fitted with a second order polynomial Errore. Il segnalibro non è definit
Figu	re 52: comparison between the indivual melt pool profiles (grey) and the average profi
(red)	of sample 39, fitted with a second order polynomial Errore. Il segnalibro non è definit
Figu	re 53: Correlation between quadratic coefficient a and volumetric energy density (VEI
	ubic samples 28, 29, and 30. The regression shows a positive trend but limited reliability = 0.6485)
Figu	re 54: Correlation between quadratic coefficient a and volumetric energy density (VEI
for c	subic samples 28, 29, 30, 7 and 17. The regression quality improves significantly (R <sup>2</sup>
0.94	16), confirming the robustness of the model
Figu	re 55: Correlation between melt pool width-to-depth ratio and VED for samples 28, 29, 30
7, ar	ad 17. A strong negative trend is observed ( $R^2 = 0.9705$ ), indicating deeper and narrow
pool	s at higher VED9
Figu	re 56: Correlation between quadratic coefficient a and linear energy density (LED). The
low	regression quality ( $R^2 = 0.3209$ ) highlights the inadequacy of LED as a predictor of me
pool	curvature
г.	re 57: Correlation between quadratic coefficient a and laser power. The weak regression

# **Index of table**

Table 1: Materials that impact different mechanical properties [11]	20
Table 2: Properties imparted by addition of alloy elements in Ni [11]	
Table 3 Nickel-based Superalloy SAM chemical composition [59].	54
Table 4 Values of Volumetric Energy Density (VED) applied to cubic samples	61
Table 5:Values of Volumetric Energy Density (VED) applied to Coal Cart samples	78

# **Abstract**

The aim of this thesis is to investigate the relationships between process parameters, microstructure, and defect formation in a Ni-based superalloy produced by Laser Powder Bed Fusion (LPBF). Particular attention was given to the quantitative analysis of melt pool geometry, porosity, and grain morphology, using optical and electron microscopy. Results showed that volumetric energy density (VED) is the most reliable parameter to describe melt pool geometry, with higher VED leading to deeper and narrower pools, while models based solely on laser power or linear energy density proved inadequate. Porosity analysis highlighted a higher susceptibility in thin-wall samples, whereas post-processing heat treatments reduced defects and promoted more homogeneous equiaxed microstructures. Overall, this work provides a methodological framework for the predictive control of melt pool stability and for the optimization of LPBF processes, supporting the development of advanced superalloy components for high-performance applications.

# **Chapter 1**

# 1.1 Genearl theory about Superalloys

The term "Superalloy" refers to a group of alloys based on nickel, cobalt or iron-nickel with superior strength properties provided by reinforcing intermetallic phases such as  $\gamma$ ' and  $\gamma$ ". They initially emerged for military gas turbines during the Second World War and the early 1950s, but they have since undergone constant development and the introduction of numerous novel materials. These materials are employed in many different fields, such as power geneartion, aircraft, and other specialized industries, such premium automotive component .

Superalloys can be defined as follows: "A superalloy, or high-performance alloy, is an alloy typically based on Group VIII B (typically consisting of various combinations of Fe, Ni, Co, and Cr) elements that exhibit excellent long-time strength, creep resistance, corrosion and erosion at temperature above 650 °C, good surface stability, corrosion and oxidation resistance," according to metallurgists. The aerospace and power sectors have been the main drivers of superalloy development, which has mostly depended on chemical and technological advancements [2].

Superalloys typically have moduli of elasticity in the vicinity of 207 GPa ( $30 \times 10^6$  psi), although moduli of specific polycrystalline alloys can vary from 172 to 241 GPa (25 to 35 ×  $10^6$ psi) at room temperature, depending on the alloy system. Processing that leads to directional grain or crystal orientation can result in moduli of approximately 124 to 310 GPa (about 18 to  $45 \times 10^6$  psi), depending on the relation of grain or crystal orientation to testing direction. Physical properties (electrical conductivity, thermal conductivity, and thermal expansion) tend to be low compared to other metal systems. These properties are influenced by the nature of the base metals (transition elements) and the presence of refractory metal additions.

The capacity to maintain high mechanical strength at high temperatures—typically up to 80% of their absolute melting temperature—is one of their most intriguing properties.

They also have the advantage of being highly resistant to oxidation and hot corrosion, making them appropriate for use at extremely high service temperatures (up to 1000 °C).

Superalloys are known to have rather complex chemical compositions and are usually classified according to their base element and strengthening mechanisms, as shown in Figure 1.

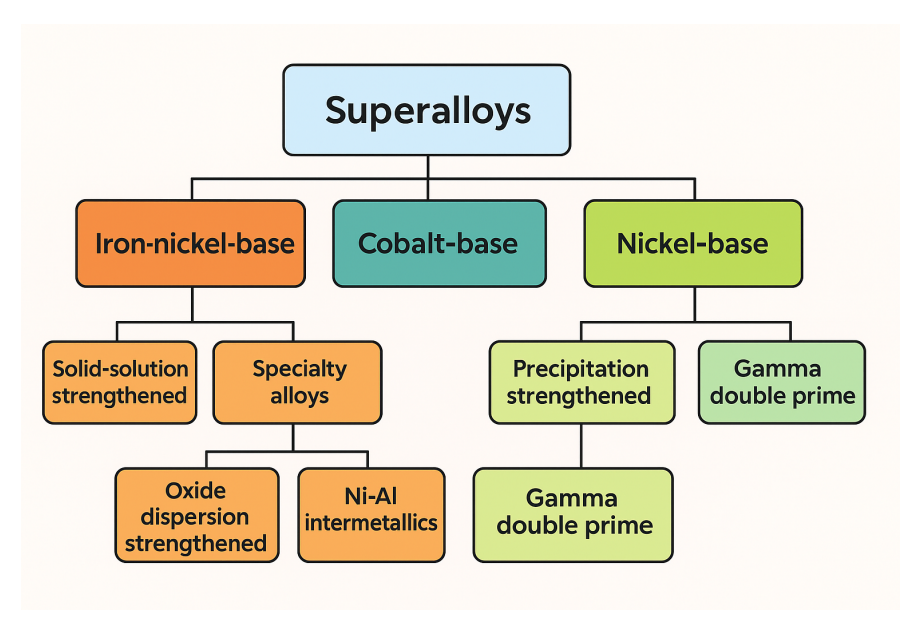


Figure 1: Classification of Superalloys

The superalloy family can be classified into three major groups:

- 1. Ni-based superalloys.
- 2. Ni-Fe-based superalloys.
- 3. Co-based superalloys.

Fe and Ni based alloys have a face-centered cubic (FCC) crystal structure, also known as the gamma ( $\gamma$ ) phase, instead Co based alloys have a hexagonal closed packed structure.

At room temperature, Fe- and Co-based superalloys have a body-centered cubic (BCC) structure. However, adding Nickel can keep the austenitic FCC structure. Ni-based superalloys have an austenitic FCC ( $\gamma$ ) matrix phase at room temperature and a variety of secondary phases, including FCC gamma prime ( $\gamma$ ') and body-centered tetragonal (BCT) gamma double ( $\gamma$ ''). The iron-nickel-base superalloys are an extension of stainless-steel technology and genearly are wrought, whereas cobalt- and nickel-base superalloys may be wrought or cast, depending on the application/composition involved.

Adjustments in composition and processing (including heat treatment) can influence properties, and finished products have outstanding strength at elevated temperatures. Figure 2 compares

stress rupture behavior between three alloy classes. Superalloys have several applications, including casting, rolling, extruding, forging, and powder-processing. The shapes produced include sheets, bars, plates, tubing, shafts, airfoils, disks, and pressure vessels (cases). Metals have several applications, including gas turbines, nuclear reactors, airplane skins, spacecraft constructions, petrochemicals, orthopedic and dental prostheses, and environmental protection. Although designed for high-temperature applications, some are employed at cryogenic temperatures while others are used at normal temperature. Applications continue to increase, although at a slower rate than in prior decades. In terms of volume, aerospace remains the most popular application.

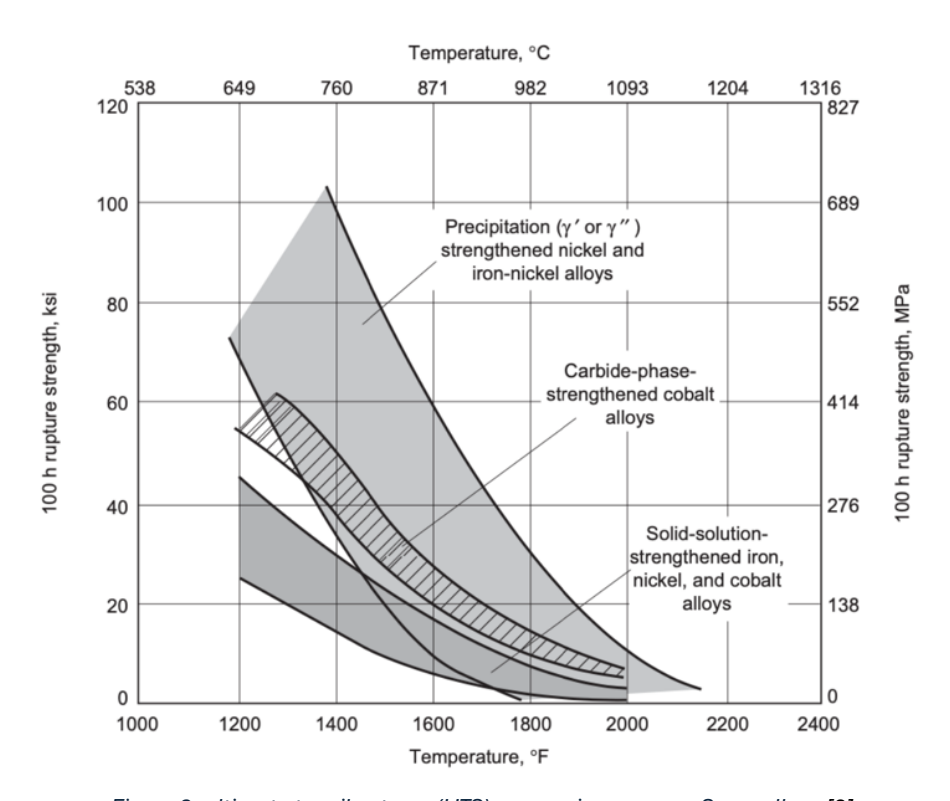


Figure 2: ultimate tensile stress (UTS) comparison among Superalloys [3].

#### 1.1.1 Strengthening mechanism

Superalloys undergo several processes to enhance their mechanical characteristics. They are strengthened by three principal mechanisms: solid solution hardening (SSH), precipitation hardening (PH) and dispersion strengthening:

1. **Solid-Solution Strengthening**: consists in alloying nickel with other elements in order to increase the strength of the matrix; atoms of different elements occupy interstitial sites within the crystalline lattice of nickel or reticular sites when replace the nickel

atoms of the crystal lattice. Elements that undergo in solid solution present dimensional atomic variations respect to nickel atom of the order of 1 to 28% [4], this atomic radius mismatch leads to a distortion of the atomic lattice that increase the Young modulus and inhibits the movement of dislocations. Furthermore, this type of reinforcement reduces the stacking fault energy (SFE) in the crystal lattice, hence inhibiting dislocation cross slip, the most important deformation mechanism for defective crystals at high temperatures. The reduction in SFE makes it more difficult for dislocations to modify the slip plane[5].

Aluminum provides a significant contribution to solid solution strengthening, followed by tungsten, molybdenum, and chromium. Iron, titanium, vanadium, and cobalt do not offer considerable reinforcement in solid solutions. Iron in solution is often used to lower product costs.

- 2. Precipitation Strengthening: Nickel-base alloys may contain niobium, titanium, and/or aluminum, and use  $\gamma'$  and  $\gamma''$  precipitates for strengthening. The most commonly used strengthening mechanism is precipitation of intermetallic second phases known as  $\gamma$ , in genearl indicated with the chemical formula  $Ni_3X$  where X = Ti, Al, Nb, Ta. Ni3Al presents the FCC elementary unit structure with nickel atoms at the center of the cube faces and aluminum at the vertices of the cube. Ti, Nb and Ta genearte intermetallic phases too, in particular: Ni3Ti has a compact hexagonal lattice (µ), Ni3Nb has an orthorhombic or body-centered tetragonal lattice  $(\gamma'')$ , and has a body-centered tetragonal lattice. Precipitates have the same crystal lattice as the matrix phase  $\gamma$  (FCC) but slightly different cell parameters. In this situation, the two phases  $\gamma$  and  $\gamma'$  are coherent at the interface and are not separated by grain boundaries. The difference between the cell parameters introduces misfits in the overall structure that genearte elastic tensions at the interface making tough the dislocation motion. The addition of elements such as Ti, Ta, and Nb instead of Al in the intermetallic phase structure significantly alters the cell parameter and makes it incoherent with regard to the matrix lattice. In nickel-titanium/aluminum alloys, the strengthening precipitate is  $\gamma'$ . In nickelniobium alloys, the strengthening precipitate is  $\gamma''$ . The effectiveness of these hardening precipitates is determined by different factors:
  - the amount of misfit genearted;
  - the precipitates particle size. The optimal sizes for γ' precipitates vary from 200 to 500 nm;
  - the shape and the distribution of the phases;

• the homogeneity of the precipitate distribution.

The inclusion of cubic or spheroidal  $\gamma'$  precipitates inside the matrix enhances the blocking impact on dislocation motion by forcing dislocation lines to transit through channels genearted by the precipitates. In iron-nickel-base superalloys, strengthening precipitates often deteriorate at moderate temperatures (650 to 760 °C), creating structures and precipitate morphologies that are less effective in strengthening the alloy.

3. **Dispersed oxides strengthening**: in this case the strengthening agent is added to the alloy rather of precipitating from it. Oxide particles typically have dimensions ranging from 25 to 50 nm. The integration of oxides in the matrix improves the alloy's mechanical resistance and creep qualities, ensuring long-term stability. Oxides improve alloy oxidation resistance by acting as nucleation agents for protective oxides, resulting in a smooth oxide layer [8].

### 1.2 Ni and Ni-based Superalloys

Nickel has a face centered cubic (FCC) crystalline structure showed in Figure 3 which means that Ni elementary unit cell arranges 8 atoms on the vertices of a cube and other 6 atoms in the center of the cube faces.

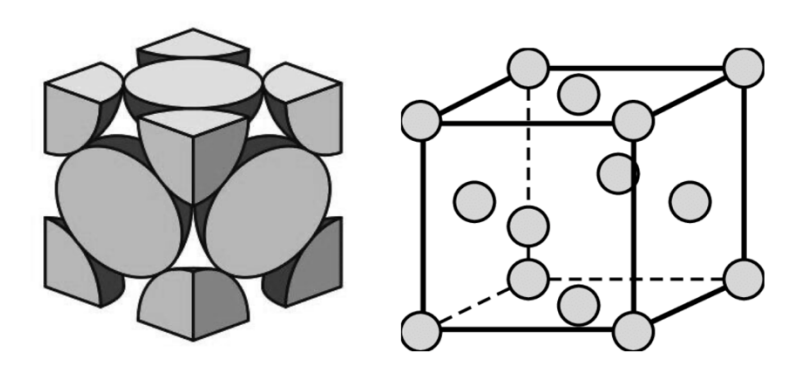


Figure 3: Ni face centred cubic structure (FCC) [3]

The most important end use for nickel is as the base metal for a wide variety of alloy systems. Nickel and nickel-base super alloys are vitally important to modern industry because of their ability to withstand a wide variety of severe operating conditions tions involving corrosive environments, high temperatures, high stresses, and combinations of these factors. There are several reasons for these capabilities. Pure nickel is ductile and tough because it possesses a face-centered cubic (FCC) structure up to its melting point (1453 °C). Therefore, nickel and nickel alloys are readily fabricated by conventional methods such as wrought, cast, and powder metallurgy (P/M) products are available and they offer freedom from the ductile to brittle transition behavior of other metals and alloys, including steels.

Nickel has good corrosion resistance in the normal atmosphere, natural freshwaters, and deaerated nonoxidizing acids, as well as great resistance to caustic alkalies. As a result, nickel provides great corrosion resistance and acts as an excellent basis for the development of specialized alloys that can take use of the unique qualities of specific alloying elements. Nickel alloys have a microstructure of FCC solid-solution austenite ( $\gamma$ ), which can form dispersoid and precipitate particles due to its high solid solubility in various alloying elements. Nickel forms a complete solid solution with copper and is nearly completely soluble with iron. It can dissolve approximately 35% Cr, 20% molybdenum and tungsten, and 5–10% aluminum, titanium, manganese, and vanadium.

Thus, the tough, ductile fcc matrix may dissolve large amounts of elements in diverse combinations, resulting in solution hardening and increased corrosion and oxidation resistance. The degree of solution hardening has been related to the atomic size difference between nickel and the alloying element, and hence the solute's ability to interfere with dislocation motion. When aluminum is left in solution, tungsten, molybdenum, niobium, tantalum, and aluminum are strong solution hardeners. Tungsten, niobium, tantalum, and molybdenum are also effective at temperatures above 0.6 Tm (Tm is melting temperature), where diffusion controlled creep strength is important. Iron, cobalt, titanium, chromium, and vanadium are weaker solution hardeners.

Finally, unique intermetallic phases can form between nickel and some nickel alloying elements. For example, aluminum and titanium are usually added together for the age-harden- ing  $\gamma$  ' precipitate  $Ni_3(Al,Ti)$ . This enables the formation of alloys with very high strengths for high-temperature services [3].

### 1.2.1 Alloying elements used in Ni-based superalloys

The major alloying elements that may be present in nickel-base superalloys are illustrated in Figure 4, where the height of the element blocks represents the amounts that may be present.

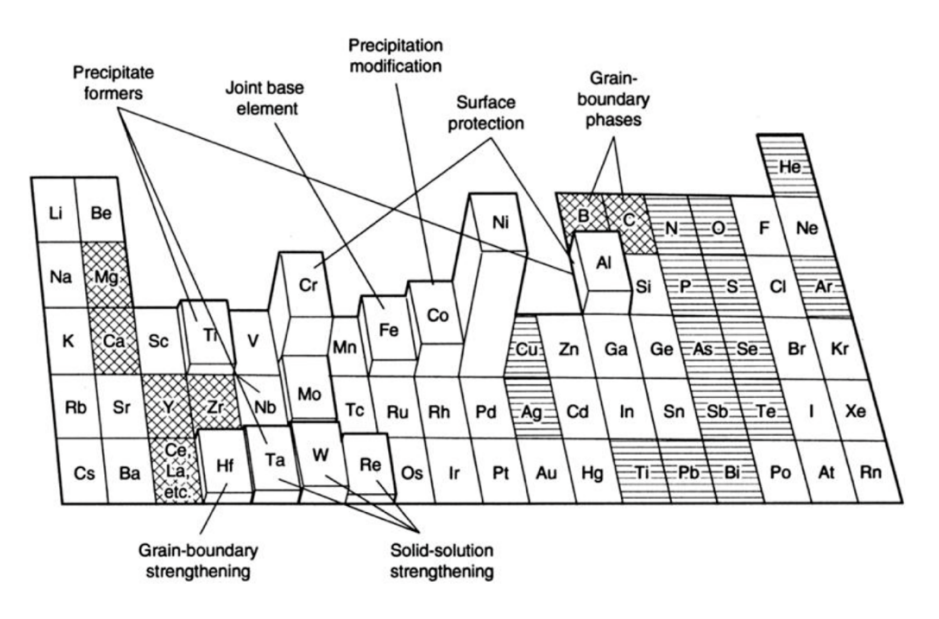


Figure 4: alloying elements used in Ni-based superalloys

Nickel, chromium, iron, and molybdenum are commonly used alloying elements in superalloys. In addition, modest amount of aluminum, tungsten, copper and titanium act as substitutional alloying elements, whereas carbon and sulfur are interstitial. While the former genearlly contribute positively to the strengthening mechanisms of the alloy, interstitial sulfur is particularly detrimental due to its tendency to cause embrittlement and hot corrosion. Alloying with chromium enhances resistance to higher temperature oxidizing and sulphidation. The addition of molybdenum significantly increases resistance to non-oxidizing acids such as hydrochloric (HCl), hydrofluoric (HF), and phosphorous acid (). Iron controls thermal expansion and increases resistance to carburization. Tungsten also resists localized corrosion, increases strength, and improves weldability. Carbon reduces corrosion resistance but increases strength at high temperatures. At higher temperatures, aluminum oxide scale develops, providing resistance to oxidation, chlorination, and carburization. Along with Ti, it upholds age hardening in some alloys. The susceptibility to intergranular corrosion can be minimized by combining Ti and C, since titanium has a stronger affinity for carbon than chromium, thus promoting the formation of stable titanium carbides instead of chromium carbides, and

preserving chromium in solid solution. The resistance to sulphidation and carburization by the addition of Co due to the solubility of carbon in nickel-based alloys.

Minor additions of B, C, Hf, and Zr tend to genearte borides or carbides, which are usually observed along grain boundaries. These components play an essential role for controlling grain size during wrought processing and minimizing damage accumulation at grain boundaries in service. The importance of B in weldability is well recognized, and this element has a significant negative impact on solidification and liquation cracking susceptibility. Low B heat has considerable cracking resistance, while high B heat cracks easily.

The negative influence of B is due to its tendency to segregate and produce an  $M_3B_2$  phase at low temperatures of around 1200 °C [11]. Carbon has a strong affinity for elements such as Hf, Zr, Ti, Nb, W, Mo, V, and Cr, and it forms primary MC (metal atom) carbides straight from the liquid during the solidification of Ni-based superalloys. The carbides are especially important in the grain boundaries of poly-crystal cast alloys for producing the appropriate strength and ductility properties [9].

A consolidated list of materials that provide the basic mechanical properties like strength, toughness and machinability when alloyed with different metals is shown in Table 1: Materials that impact different mechanical properties [11]. Minor amounts of the rare-earth metals like yttrium improves the resistance to oxidation either the alloys based on nickel or cobalt. Yttrium provides the alloy with comprehensively persistent aluminium oxide film. This film provides resistance from oxidation, carburization and chlorine attack through 1205 °C. Because of the  $\gamma'$  nature of the alloy, it has excellent strength properties through 925 °C.

Main requirements in materials for gas turbines and related high-temperature applications are high melting point, micro-structural stability at high temperature, high-temperature performance, good oxidation/corrosion behaviour, low density, high stiffness and easy to process. Table 2: Properties imparted by addition of alloy elements in Ni [11]gives the information pertaining to the properties that can be imparted by adding alloying elements with nickel in superalloys [10].

Table 1: Materials that impact different mechanical properties [11]

Hardenability	Strength	Toughness	Machinability
Molybdenum	Chromium	Calcium	Lead
Carbon	Cobalt	Cerium	Manganese
Titanium	Manganese	Chromium	Phosphorus
Manganese	Molybdenum	Magnesium	Selenium
Chromium	Copper	Molybdenum	Sulphur
Boron	Carbon	Nickel	Tellurium
Phosphorus	Nickel	Niobium	
	Niobium	Tantalum	
	Phosphorus	Tellurium	
	Silicon	Vanadium	
	Tantalum	Zirconium	
	Tungsten		
	Vanadium		

Table 2: Properties imparted by addition of alloy elements in Ni [11]

Nickel when alloyed with	Provides
Chromium, Molybdenum, Iron, Tantalum, Tungsten	Higher strength
Boron, Zirconium, Carbon	Creep resistance
Chromium, Aluminium, Tantalum	Oxidation resistance
Aluminium, Titanium	High temperature strength
Hafnium	Ductile at intermediate temperatures, Prevents oxides flaking

# 1.3 Microstructures in Ni-based Superalloys

Superalloys consist of the austenitic fcc matrix phase plus a variety of secondary phases. Secondary phases of value in controlling properties are the FCC carbides MC,  $M_{23}C_6$ ,  $M_6C$ , and  $M_7C_3$  (rare) in virtually all superalloy types; gamma prime ( $\gamma'$ ) FCC ordered  $Ni_3(Al,Ti)$ ; gamma double prime ( $\gamma''$ ) bct ordered  $Ni_3Nb$ ; eta ( $\eta$ ) hexagonal ordered  $Ni_3Ti$ ; and the delta ( $\delta$ ) orthorhombic  $Ni_3Nb$  intermetallic compounds in nickel- and iron-nickel-base superalloys. The  $\gamma'$ ,  $\gamma''$ , and phases also are known as geometrically close-packed (GCP) phases. In addition to grain size and morphology, (plus occasional cold work) it is the production and control (manipulation) of the various phases that give superalloys their unique characteristics. Superalloys get their strength mostly from solid-solution hardeners and precipitated phases. Iron-nickel- and nickel-base superalloys contain the principal strengthening precipitate phases,  $\gamma'$  and  $\gamma''$ . Carbides can provide modest strengthening directly (via dispersion hardening) or indirectly (by stabilizing grain boundaries against severe shear). Carbides are present in all three

superalloy classes. The  $\delta$  and  $\eta$  phases help control the structure of wrought iron-nickel and nickel-base superalloys during processing. The extent to which they contribute directly to strengthening varies according to the alloy and its processing. In addition to the elements which lead to solid solution hardening and/or carbide formation, other elements (such as boron, zirconium, and hafnium) are added to improve mechanical or chemical properties.

These minor elements are not commonly found in most cobalt-base alloys. Some carbide-forming elements may also have a major impact on chemical characteristics. Borides can occur in iron-nickel and nickel-based superalloys. Detrimental phases also develop in superalloys. Topologically Close-Packed phases (TCP) include  $\sigma$  (FeCr, FeCrMo, CrCo),  $\mu$ , and Laves, which are brittle and negatively impact the mechanical properties of superalloys, especially nickel-base superalloys. These phases can also develop in superalloys based on iron, nickel, and cobalt. Early investigations on stainless steels suggest that modifications in alloy chemistry can influence these phases, especially the  $\sigma$  phase. Furthermore, these phases aren't always undesirable. Evidence suggests that even small amounts of  $\sigma$  may improve creep-rupture strength [12].

## 1.3.1 y phase matrix

For a number of reasons, the fcc  $\gamma$ -phase matrix is perfect for high-temperature structural alloys.

- 1. The densely packed fcc matrix is perfect for use at high relative temperatures (T/TM) due to the low diffusivity of alloying elements;
- 2. The fcc matrix has a broad solubility of secondary elements that enables the dissolution of high melting point refractories and the precipitation of intermetallic compounds, such as  $\gamma'$  and  $\gamma''$  for strengthening;
- 3. The fcc matrix has optimal mechanical properties (tensile, rupture, creep, and thermomechanical fatigue) due to its high modulus and multiple slip systems.

The matrix-phase composition is mainly made up of the super-alloy base metal, but it also includes a significant amount of solid-solution elements such as cobalt (or nickel in cobalt-base superalloys), chromium, molybdenum, tungsten, tantalum, and rhenium. These elements contribute to the matrix's hardening properties.

# $1.3.2 \gamma' - Ni_3(Al, Ti)$

The  $\gamma'$  -Ni<sub>3</sub>(Al, Ti) precipitate is undoubtedly the most useful and important strengthening phase in superalloys. Its yield strength increases with temperature up to 800 °C, and it is the main strengthening constituent in a wide variety of nickel and nickel iron base superalloys. However, in nickel—iron base alloys the  $\gamma'$  phase is only metastable and, during long-term exposure at elevated temperatures, it may lose coherency with the  $\gamma$  matrix or transform into more stable phases such as  $\eta$ -Ni<sub>3</sub> Ti, which constitutes a drawback to the use of iron as a base element. The phase develops as a coherent precipitate inside the  $\gamma$  matrix, with different morphologies depending on heat treatment and content.  $\gamma'$  disperses throughout the matrix, however filmlike  $\gamma'$  can develop at grain boundaries following high-temperature exposure, which is considered to be beneficial to creep-rupture qualities. Tetragonal distortion maintains the coherence of the  $\gamma'$  phase and fcc  $\gamma$  matrix. As a result, it is feasible to nucleate homogenous precipitates with low surface energy and remarkable long-term stability. The presence of such precipitates is especially advantageous in alloys designed for high-temperature exposure because it permits the ideal microstructure to be kept for a longer period of time at high temperatures.

The compatibility between  $\gamma$  and  $\gamma'$  is quantified by the lattice misfit  $\delta$ :

$$\delta = \frac{\alpha_{\gamma'} - \alpha_{\gamma}}{\left(\frac{\alpha_{\gamma'} + \alpha_{\gamma}}{2}\right)}$$

The lattice mismatch significantly impacts the shape of the  $\gamma'$  precipitate. A lattice mismatch magnitude of 0 to 0.2 percent results in a spherical precipitate; between 0.5 and 1.0 percent, a cuboidal precipitate; and above 1.25 percent, a platelike precipitate [13]. Increasing the lattice misfit between  $\gamma/\gamma'$  enhances creep life in single-crystal nickel-base superalloys. The  $\gamma/\gamma'$  interface limits mobile dislocations and hinders plate thickening owing to dislocation pile-up. As the lattice mismatch increases, the interfacial dislocations become increasingly closely spaced, forming a strong barrier to mobile dislocations shearing through the interface. It follows that for alloys with high values of lattice mismatch, the number of interfaces should be maximized to attain optimal properties. Alloys with lower values of lattice mismatch have weaker interfaces, and in these alloys, the number of interfaces appears to have less effect on creep properties. The size of the  $\gamma'$  precipitate is important for proper precipitation hardening, as hardening normally increases with particle size until it reaches a critical size. Beyond this

size, the dislocation movement mode flips from cutting to bypassing, resulting in a reduction in hardness and strength. The  $\gamma'$  phase's yield strength increases with temperature from 196 to 800 °C. The relationship between yield strength and temperature is mainly reliant on the aluminum concentration in the  $\gamma'$  phase. The magnitude and position of the peak in flow stress are regulated by the presence of alloying elements such as titanium, chromium, and niobium. The volume fraction of the  $\gamma'$  phase influences the alloy's strength and creep properties, as well as the manufacturing processes available for a certain component. Alloys with significant  $\gamma'$ volume fractions, having been subjected to supersolvus solutionizing (at temperatures exceeding the  $\gamma'$  solvus), followed by aging, develop secondary cuboidal  $\gamma'$  precipitates. These precipitates are dispersed throughout the  $\gamma$  (gamma) nickel matrix, as shown in Figure 5: schematic of microstructure in  $\gamma$ 'Ni-base superalloys after solution heat treatment above the  $\gamma'$ solvus and aging. Their effectiveness stems from impeding dislocation motion. This hindrance is linked to the necessity for dislocations to create antiphase boundaries when traversing the ordered  $\gamma'$  structure, coupled with the locking effect on dislocations during cross-slip occurrences. Further resistance arises from the formation of spheroidal tertiary  $\gamma'$  within the  $\gamma$ channels, leading to a bimodal  $\gamma'$  size distribution. In alloys where a subsolvus solutionizing step is performed instead of the supersolvus solutionizing, the primary  $\gamma'$  that forms during the manufacturing process and during the heat treatment's temperature ramp up remains in the microstructure. The  $\gamma'$  phases after a subsolvus heat treatment tend to have a less uniform shape and are typically larger in size.

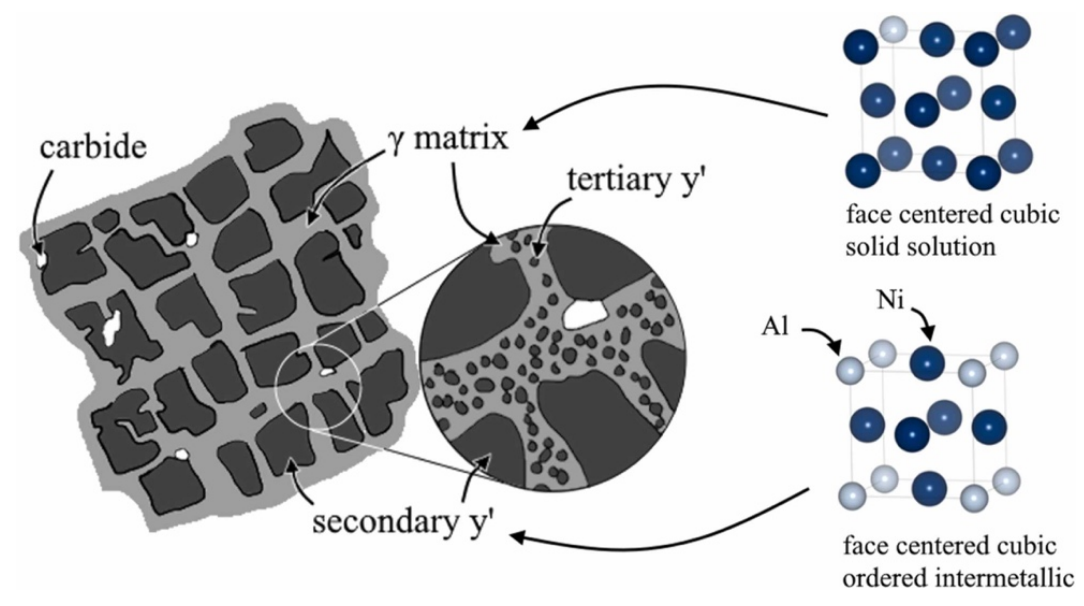


Figure 5: schematic of microstructure in  $\gamma$ 'Ni-base superalloys after solution heat treatment above the  $\gamma$ ' solvus and aging .

Alloys can be hot wrought at low  $\gamma'$  volume fractions, but above 40 to 45 percent volume fraction of  $\gamma'$  (60 percent for powder materials), forging is no longer feasible and the component must be made by casting. The drawback of  $\gamma'$  strengthened alloys is that the component's service temperature and life are eventually limited by the coarsening and dissolution of the  $\gamma'$  precipitates. The binary nickel-aluminum phase diagram shows that the phase completely dissolves at around 1400 °C. In practice, lower solvus temperatures for  $\gamma'$  can be observed due to the influence of other elements in the alloy. Heat treating precipitation-hardened alloys becomes more challenging when the  $\gamma'$  solvus temperature approaches the alloy's incipient melting point [15]

## 1.3.3 γ" - Ni3Nb

Although not as commonly used as the  $\gamma'$  precipitate, the  $\gamma''$  precipitate is a useful strengthening phase, mainly in such nickel-iron-base superalloys as alloys 718 and 706.

One of the main disadvantages of  $\gamma''$  as a strengthening phase in comparison to  $\gamma'$  is its lower solvus temperature. Alloys hardened through  $\gamma''$  precipitation have a rapid decrease in strength above 650 °C, caused by the loss of the strengthening  $\gamma''$  phase as it transforms to  $\delta$ . Nickeliron-base alloys are particularly susceptible to the transformation of  $\gamma''$  to at temperatures above 650 °C [15].

#### 1.4 Carbides

Carbides have a complex role in superalloys, increasing or decreasing alloy characteristics depending on their location, composition, and shape. Carbides are found in all superalloy families and tend to locate at grain boundaries, particularly in nickel-base superalloys. In genearl, carbides have a positive influence on rupture strength at high temperatures if they are of the proper type (composition) and shape. The shape of carbides also affects alloy ductility. Carbides have an indirect negative effect on the chemical stability of their matrix because they deplete carbide-forming components locally. Primary carbides, such as MC (where "M" stands for tantalum, titanium, zirconium, or tungsten), are genearted as discrete blocky particles or eutectic phases during casting solidification and often have a fcc crystal structure. These carbides come up during solidification as discrete particles dispersed heterogeneously throughout the alloy, both intragranular and intergranular, and frequently form between

dendrites. These carbides act as a significant source of carbon for the alloy during heat treatment and service. The recommended order of carbide formation in superalloys is HfC, TaC, NbC, and TiC, in order decreasing stability. Secondary chromium-rich carbides form mainly at grain boundaries and typically appear as irregular, discontinuous, blocky particles, however plates and regular shapes have also been reported. carbides also precipitate in blocky form on grain boundaries, forming Widmanstätten structures. However, both types of carbides can form from the degeneartion of MC carbides or from soluble residual carbon in the alloy matrix. The carbides display a complex cubic structure, which, if the carbon atoms were removed, would closely approximate the structure of the tcp  $\sigma$  phase. The critical location of along grain boundaries imparts a significant increase of stress rupture strength, apparently through inhibition of grain boundary sliding. Rupture failure can eventually initiate either by fracture of these grain-boundary carbides or by loss of cohesion at the interface. The carbides also have a complex cubic structure but form at slightly higher temperatures of 815 to 980 °C than carbides. Because of their higher formation temperature in comparison to that of, carbides are more beneficial as a grain boundary precipitate for controlling grain size during processing of wrought alloys. Carbides also provide microstructural refinement during cooling from heat treatment and during fabrication. The mechanical properties most directly affected by carbides are stress rupture strength and tensile strength. The main benefit of primary MC carbides is indirect in that they provide a relatively stable source of carbon for precipitation of secondary carbides. However, scriptlike grain boundary primary MC carbides serve both as crack initiation sites and crack propagation paths and are therefore considered detrimental.

#### 1.5 Borides

Borides are hard refractory particles which vary in shape from blocky to half-moon. Boron's small atomic radius and low solubility in the matrix phase lead to its concentration at grain boundaries, where they are most commonly found. Borides, like carbides, can be used to strengthen nickel-iron and nickel-base alloys, as well as increase an alloy's hot workability. Even though boron content is strictly monitored in new-geneartion superalloys, borides can be found in brazed superalloy joints when low melting point Ni-Cr-B brazing alloys are used. Boron can lead to cracking of the heat affected zone in the welding of nickel base superalloys, even at concentrations as low as a few parts per million.

# 1.6 Topologically Close-Packed Phase

Topologically close-packed phases are undesirable, and considerable effort is made to avoid compositional ranges that will cause their precipitation during heat treatment or service. In these phases, the atoms are close-packed in layers that are separated by intervening layers of relatively large atoms. They often form as platelike or needlelike precipitates. The tcp phases observed in superalloys include  $\sigma$ -AxBy,  $\mu$ -Ax By, and Laves-A2B phases, where A is iron, nickel, or cobalt, and B is niobium, molybdenum, tantalum, or chromium. The formation of these phases reduces rupture strength and ductility. To form TCP phases, specific compositions and relatively large amounts of chromium, molybdenum, and tungsten are necessary. Thus, to avoid the potentially detrimental consequences of these phases, overall contents of chromium, molybdenum, and tungsten must be controlled [15].

TCP phases are very detrimental because of two main factors. At first, when they nucleate and grow, they deplete the  $\gamma$ -matrix phase from solid solution strengtheners. This leads to decreased creep resistance of the material. Further, TCP phases are brittle and exhibit a complex lath or plate like morphology, which evolves with time. Thus, cracks are easily nucleated. As a consequence the fatigue life-time and tensile ductility of the material will be decreased [12] Techniques have been developed to determine the susceptibility of any particular alloy to tepphase formation. In particular, the electron vacancy method (Nv), embodied in PHACOMP (Ref 33), has been used to predict  $\sigma$ -,  $\mu$ -, and Laves-phase formation in superalloys (Ref 14, 34 to 36). Themethod is based on the correlation between tep-phase formation and the number of electron vacancies in the  $\gamma$  matrix [15].

# Chapter 2

# 2.1. Metal Additive Manufacturing

Metal additive manufacturing involves manufacturing techniques that build metallic objects by progressively adding powder, genearlly in successive layers. This technology's considerable expansion is, in part, fueled by its potential for both business advantages and performance improvements, especially within the aerospace sector. Key possibilities offered by metal additive manufacturing include: substantial cost and turnaround time decreases, the ability to employ innovative materials and distinctive design approaches, weight reduction in components thanks to highly effective and lightweight designs, and the integration of multiple parts for the purpose of enhanced performance or risk mitigation – for instance, through internal cooling mechanisms in components subjected to thermal stress, or by eradicating conventional joining processes.

Compared to traditional subtractive manufacturing techniques, additive manufacturing distinguishes itself through its layer-by-layer manufacturing. It relies on a common feedstock, often in the form of powder or wire. A heat source melts or fuses this material, which then solidifies. The final geometry emerges according to a digitally specified trajectory followed by the heat source [19].

By utilizing the design freedom of metal AM, it is possible to optimize the material distribution, reducing mass while maintaining the mechanical and other performance requirements of the component. It is also possible to combine components, reducing risk and cost for multiple components and reducing potential failure modes across joint. Beyond these advantages, superior performance, compared to traditional manufacturing methods, can be achieved. This

is accomplished through the utilization of mechanical, thermal, and other optimization techniques. The design of complex components, once unachievable, is now within reach. Examples include integrated internal features like conformal cooling channels in combustion chambers or turbine blades [20].

The basic principle of AM is to build up components layer-by- layer directly from 3D model data created using Computer-Aided Design (CAD) to near net or final shape. This is a complex procedure as a large multitude of process parameters have possible effects on the quality of produced components. Numerous factors, such as the power level, the velocity of the scanning beam, hatch spacing or over-lap between tracks, and also the scanning approach itself (e.g., employing contours, varying the orientation of hatch tracks per layer, etc.), are process parameters that can impact the overall procedure, and in turn, the final properties and the quality of the manufactured components. These aspects, in detail, involve surface roughness, the existence of pores, leftover stress that builds up and the related fractures or distortions the items may undergo, along with unique arrangements at the microscopic level, and the material's property of anisotropy

Further disadvantages of AM include limited materials, uncertainty in material properties, specific design constraints inherent to AM, post-processing requirements, waste geneartion (used powder, build plates, failed builds), increased requirements of design skills to allow lower-mass components with feasible complex designs, often utilizing time-consuming topology optimization software workflows, as well as the need for strict quality control and certi- fication of the process.

Additive manufacturing encompasses seven process groups which include directed energy deposition (DED) and powder bed fusion (PBF). Both of these enable the creation of metal parts with near full density. Laser powder bed fusion (L-PBF) stands out and is increasingly popular in industrial settings. It gaining traction in industry due to its ability to produce parts with high resolution and quality, merging the ability to produce fine features with the appropriate build volumes suitable for many different part sizes required

#### 2.1.1. Laser Powder Bed Fusion

The Laser Powder Bed Fusion (LPBF) consists of several steps, from computer-aided design (CAD) model preparation to removing fabricated parts from the build platform. Prior to the upload of the CAD data into the LPBF machine to produce parts, it is essential to process the stereolithography (STL) files. This step involves the creation of supportive structures for any

overhanging aspects and the geneartion of slice data, which governs the laser's scanning behavior across each individual layer. The printing process starts with the application of a thin metal powder layer upon a substrate plate, this is achieved via a recoater, either a roller or blade. Subsequent to the powder's deployment, one or more high-energy density laser sources are used to fuse specific areas of the powder. Once the laser scanning is completed, the build platform is lowered, and the next layer of powder is deposited on top. The laser then scans a new layer, and the process is repeated until the parts are completely printed. Throughout the printing process, the build chamber is shielded with a consistent flow of an inert gas, such as argon or nitrogen, so as to avoid oxidation. Furthermore, the uniform gas stream that moves across the build region also aids in eliminating any condensate, such as spatters and vaporized metal that has condensed, genearted during the process of powder fusion, an activity critical in affecting the standard and the operational characteristics of the resultant parts.

Upon conclusion of the process, any unbound powder is extracted from the chamber, allowing the separation of the components from the substrate plate, which can be done manually or by electrical discharge machining. The entire process is automated, except for the CAD data preparation process and the removal of the printed parts from the build platform . Schematic illustrations of the LPBF machine is presented in Figure 6: process steps and schematic of the LPBF .

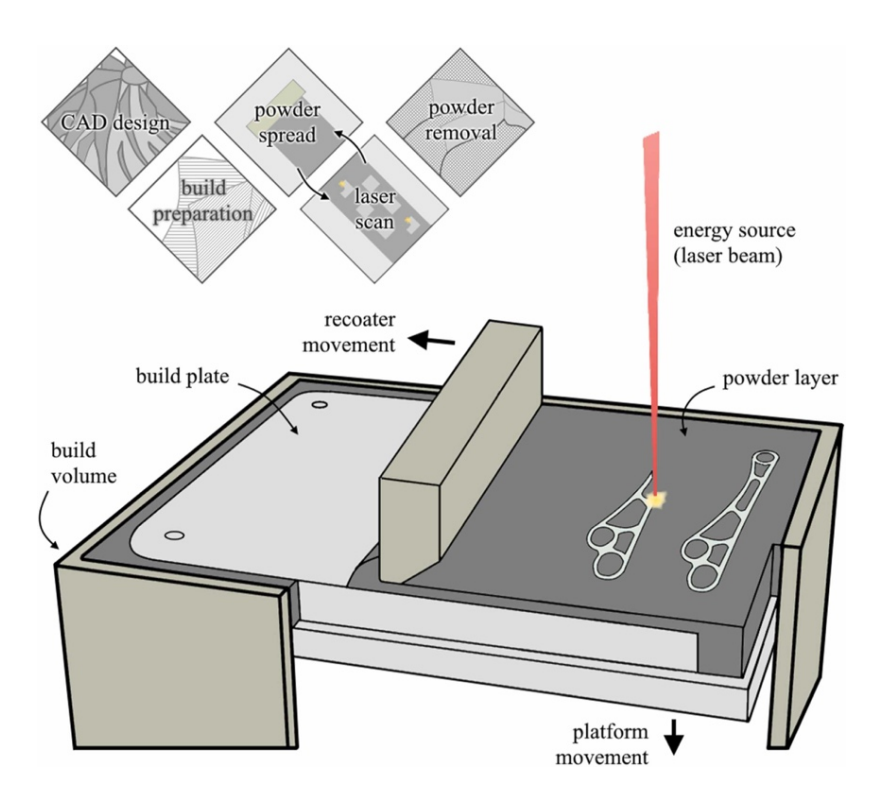


Figure 6: process steps and schematic of the LPBF.

#### The main advantages of LPBF are:

- A high-quality, focused laser beam is a crucial component of this method. The laser's
  energy is potent enough to fuse metals, thus ensuring a high degree of accuracy in the
  printing process. The process's inherent precision lends itself perfectly to the direct
  fabrication of intricate geometries. These often feature delicate details and surfaces that
  exhibit minimal roughness.
- 2. The resulting melt pools exhibit incredibly rapid cooling. These cooling rates, which are influenced by both the specific process settings and the material used, can range from 10<sup>3</sup> to 10<sup>8</sup> Kelvin per second. The extraordinarily quick cooling gives rise to exceedingly fine microstructures, which directly translate into excellent mechanical performance characteristics for the produced components.
- 3. This technique enables the fabrication of parts characterized by significant relative density, exceeding 99%. It works with an extensive range of metallic materials. These materials encompass titanium and its associated alloys, a spectrum of iron and steel alloys, nickel-based alloys, cobalt-based alloys, aluminum-based alloys, and copper alloys. As a result, a high level of structural integrity can be achieved in the finished components.
- 4. The overall cost and time frame associated with the manufacturing process are considerably reduced. This advantage is particularly significant when producing high-value components in smaller batches, offering notable efficiencies.

#### Meanwhile, the limitations of LPBF are:

- 1. Significant internal stress builds up within components due to considerable temperature differences. Consequently, a subsequent heat treatment step is frequently implemented to eliminate these stresses.
- 2. Components with projecting features need the addition of support structures, and manual removal of these supports is a post-process requirement.
- 3. The overall dimensions of printed elements are constrained by the build chamber's capacity.
- 4. The selection of usable powder materials is restricted. Furthermore, printing highly reflective materials, such as unalloyed copper and aluminum, presents difficulties when using infrared lasers.

5. A slower manufacturing rate is typical of this method due to the repeated powder application procedure.

The Laser Powder Bed Fusion (LPBF) method, illustrated in Figure 7. These are: (1) laser-related parameters (laser power, beam spot size, pulse duration, pulse frequency, etc.), (2) scanning-related parameters (scanning speed, hatch spacing, scanning strategy, etc.), (3) powder bed-related parameters (powder bed density, layer thickness, etc.), and (4) temperature related parameters (powder bed temperature, substrate temperature, etc.).

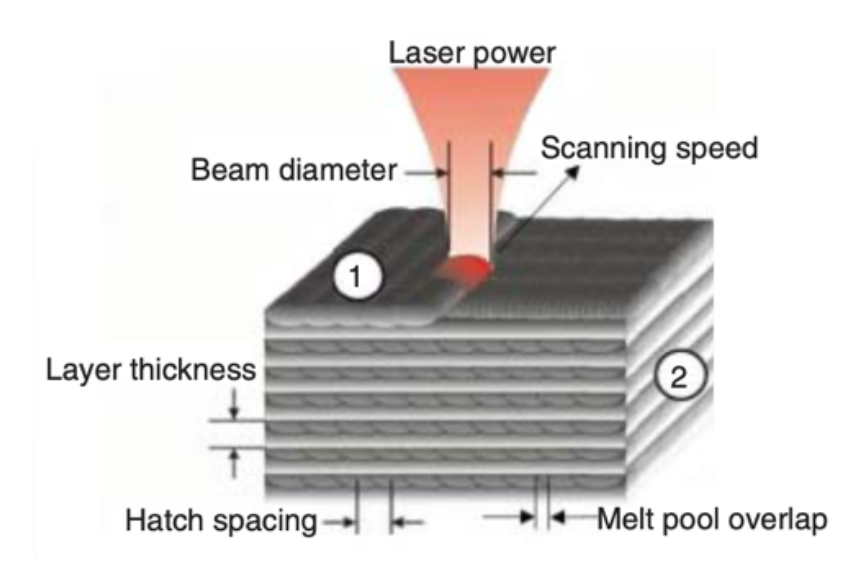


Figure 5: schematic illustration of the key process parameters

The specific laser wavelength, dictated by the chosen laser type, governs how well a powder material absorbs the laser's energy. Three types of lasers are commonly used in LPBF equipment: CO2 lasers, fiber lasers, and diode-pumped Nd:YAG lasers. The degree to which adjacent melt tracks overlap is characterized by the hatch spacing, impacting the quality of metallurgical bonding that forms between them. When hatch spacing is small, an excess of overlap is frequently observed, which adds to the overall fabrication time. Conversely, excessively wide hatch spacing restricts the maximum attainable layer thickness and elevates the risk of gaps appearing due to insufficient bonding within each layer. The layer thickness selected has to be sufficient in size to enable the part to be fabricated layer by layer, cumulatively. But, going over a certain point in layer thickness can promote the geneartion of metallurgical defects, such as ballingand lack of fusion, thus degrading the structural integrity and properties of the printed part. The laser power controls the amount of energy delivered to their radiated material.

In addition to regulating the melting efficiency, the laser power plays a key role in determining the dimensions and continuity of each melt track, which subsequently has implications for the strength and overall quality of the part. The velocity at which the laser scans impacts both the melting and cooling rates. When the scanning rate is slow, the region impacted by the laser remains in a molten state for a longer duration, thus slowing the cooling down and influencing the resulting microstructure as well as the size of the melt track. Typically, parameters such as the powder employed, the size of the laser beam, and the thickness of each layer remain constant for a particular build. This leaves the optimization of the laser power, scanning speed, and hatch spacing as the primary avenues for improvement.

The scanning strategy defines the spatial movement pattern of the laser beam. Various scanning strategies have been developed in pursuit of printing components with near-full density and controllable crystallographic texture. In the Laser Powder Bed Fusion (LPBF) method, four fundamental layouts – specifically, unidirectional, bidirectional, stripe/paintbrush scanning, and island/chessboard/checkboard scanning – are regularly utilized on a layer-by-layer basis (Errore. L'origine riferimento non è stata trovata.).

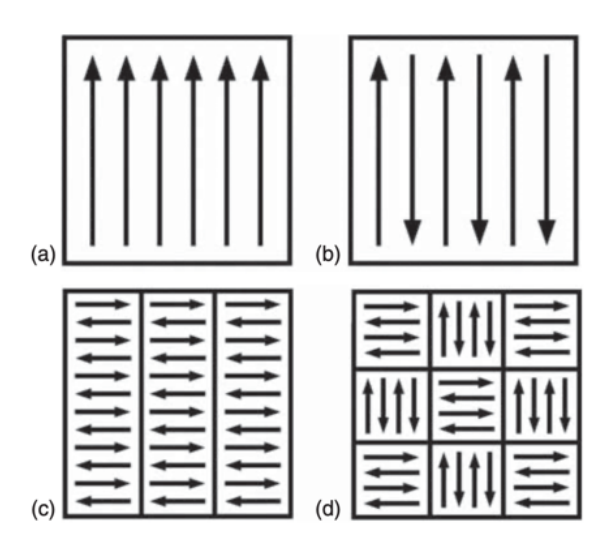


Figure 8: main scanning patterns in a single layer. (a) unidirectional scanning,

(b) bidirectional scanning, (c) stripe/paintbrush scanning, (d) island scanning.

- a. Unidirectional Scanning: this scanning approach follows the most direct path: the scan consistently moves in a single direction. This typically results in the lowest material compaction, yet concurrently yields the most robust texture observed on the fused material.
- b. Bidirectional Scanning: contrarily, bidirectional scanning operates by alternating scan directions across adjacent lines, resulting in a zig-zag layout. The lines alternate in their travel direction during the scanning operation.

- c. Stripe Scanning: Stripe scanning is carried out by scanning bidirectionally within each parallel stripe.
- d. Island Scanning: Island scanning adopts a checker board pattern of alternating bidirectional fills, which reduces temperature gradients in the scan plane by uniformly distributing the process heat [22].

# **2.2.** Laser powder bed fusion of difficult to print $\gamma'$ Ni-based superalloys

Alongside the development of PBF-LB technologies, considerable effort has been dedicated to material development and certification. Nonetheless, the selection of alloys approved by PBF-LB system producers is considerably less than those accessible for subtractive and forming methods. This constraint restricts the application of PBF-LB in several areas. A particularly noticeable gap within the PBF-LB material range is the lack of high-strength, high-temperatureresistant  $\gamma'$  (gamma prime) Ni-based superalloys. The commonly printed Ni-based superalloys are either primarily  $\gamma''$  strengthened and therefore limited to intermediate temperatures (i.e., Inconel 718 has only a minor strength contribution from  $\gamma'$ ) or are primarily solid solution strengthened alloys with comparatively poor mechanical properties (Inconel 625 and Hastelloy X). Contrastingly,  $\gamma'$  precipitation-strengthened Ni-based superalloys are a class of alloys widely used in the power geneartion, aerospace, and automotive sectors. These materials are selected for components that must endure temperatures exceeding 700°C. These are crucial in the hot sections of power and aerospace turbine engines (within turbine blades, vanes, and disks) or in high-performance automotive turbochargers (turbine wheels). Whilst these alloys were originally tailored for casting processes, a rising interest exists in leveraging the capabilities that PBF-LB provides, utilising these established, high-temperature-resistant materials. Unfortunately, these alloys are notoriously difficult to weld, and many of the same challenges have appeared when attempting to additively manufacture them using PBF-LB. In the five years since 2019, there has been a steady increase in the attention given to the processing of  $\gamma'$  Ni-based superalloys using PBF-LB both in academic research and in industry. Progress has even been made on the qualification and release of print parameters for the less challenging  $\gamma'$  Ni-based superalloys by PBF-LB machine vendors. Alloys 282, 939, 738, and 247 are the most frequently studied with respect to their PBF-LB processability.

## 2.2.1. Defect formation during LPBF of y' Ni-based superalloys

Gamma prime ( $\gamma'$ ) Nickel-based superalloys, suffer from the typical void formation present in other welding and fusion AM processes, including lack of fusion or keyhole porosity. When the energy introduced is too low, the powder feedstock may not fully melt, leading to inadequate bonding between adjacent material tracks, thus causing a lack of fusion. Conversely, an excess of energy can lead to keyhole porosity. This happens when excessively deep melt pools with high aspect ratios become unstable, leading to material vaporization. This process traps gases, ultimately forming spherical pores within the solidified alloy. Genearlly, between these two conditions, a process parameter window can be identified for most materials where highly dense, mostly defect- free material can be printed. Nevertheless, certain alloys—particularly  $\gamma'$  Ni-based superalloys—are susceptible to cracking of different varieties. Consequently, the operating window of process parameters for the production of sufficiently defect-free microstructures shrinks considerably. The predominant mechanisms for cracking include solidification cracking, liquation cracking, strain age cracking, and ductility dip cracking. These cracking events can happen under two distinct scenarios: at full solidification, known as cold or solid-state cracking, or when some liquid is still present, known as hot cracking.

Solidification cracking arises from a confluence of elements that become active during the solidification process of an alloy, specifically within the "mushy zone" Figure 6 as it cools and transforms from a liquid to a solid phase. The segregation of solute is a primary instigator, wherein solute elements preferentially migrate into the remaining liquid. This concentration forms a thin layer of low-melting-point liquid along the boundaries of both subgrains and grains; these areas solidify last. Concurrent with this, the melt pool material is subjected to tensile stresses and strains, brought about by thermal effects and the solidification itself. The material shrinks as it changes phase from liquid to solid and as the already solidified material cools further. Consequently, the weakened, less ductile, solute-concentrated material – the last to solidify – exhibits an increased likelihood of cracking [25].

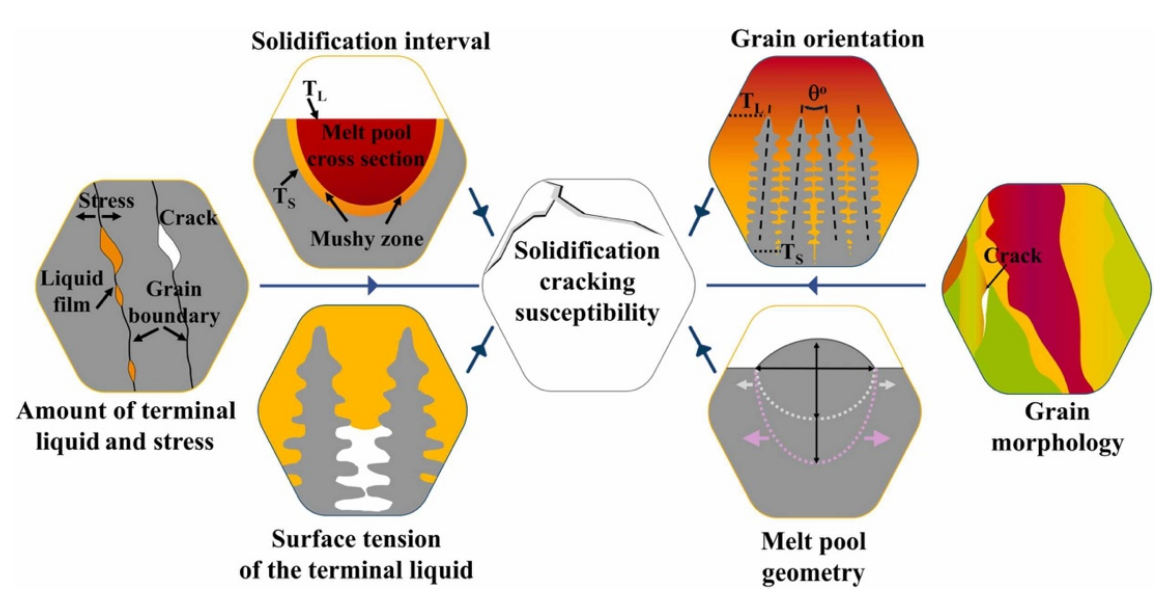


Figure 6: Factors contributing to solidification cracking

Comparable to solidification cracking, **liquation cracking** similarly stems from the creation of phases with low melting points, or the segregation of solutes along subgrain or grain margins. The distinctive trait, however, is that cracks appear within material that has already solidified. This happens when neighboring paths or successive layers are laid down. The already hardened material is then warmed once more to a temperature above the eutectic temperature but below the liquidus temperature of the matrix, leading to localized melting of the low-melting-point phases. Since liquids can't support any stress, the regional decrease in material strength, if merged with tensile stresses, can divide the boundaries and induce crack formation [26]. Strain age cracking in  $\gamma'$  Ni-based superalloys is frequently witnessed exclusively after the Powder Bed Fusion-Laser Beam (PBF-LB) procedure, specifically during thermal treatments. These thermal treatments genearly commence with a solutionizing phase. Solutionizing typically involves high temperatures exceeding 1100 °C. This stage is responsible for stress relaxation, dissolution of any y' particles formed during the PBF-LB's cyclical heating and cooling, mitigation of microsegregation at grain and subgrain interfaces, and the possibility of recrystallization. Subsequently, as the alloy cools from solutionizing,  $\gamma'$  phase nucleation takes place, leading to an aging step. The aging treatment, usually conducted above 800 °C, aims to enlarge the  $\gamma'$  phase to its ideal dimensions and morphology for optimized mechanical behavior. However, aging temperature is below the solutionizing treatment temperature. When the solutionizing heating ramp-up is too slow,  $\gamma'$  precipitation and growth become possible. Several key elements contribute to strain age cracking. These include an increase in strain due to volume

changes from  $\gamma'$  precipitation, strain increases caused by lattice misfit between the  $\gamma'$  phase and the  $\gamma$  matrix, the existing residual stresses introduced during PBF-LB, and the embrittlement related to growing intragranular  $\gamma'$  and intergranular carbide development -.

In some PBF-LB systems, the use of high temperature build-plate heating capabilities may cause growth of the  $\gamma'$  phase that leads to strain age cracking during the PBF-LB process. However, these systems are not widespread and face barriers when it comes to industry adoption. These barriers include higher system costs, reduced build plate size resulting in uneconomical batch sizes or restrictive part size limitations, and powder reuse challenges that arise from the higher oxygen and nitrogen pickup at elevated temperatures.

**Ductility dip cracking**, much like strain age cracking, represents a solid-state process. This phenomenon involves a notable reduction in the material's ductility, observable within a limited temperature range, situated between the solidus temperature (T s) and half of that value (0.5T s). Unlike strain age cracking, its manifestation is possible during the PBF-LB procedure, affecting both precipitation-strengthened and solid solution-strengthened alloys. Alloy composition is a key factor influencing susceptibility; certain alloys are forecasted to be more prone [28].

#### 2.2.2. Melt Pool

The Laser Powder Bed Fusion (LPBF) process is characterized by intricate heat transfer and fluid dynamics; a key aspect of the process is the melt pool. The melt pool's stability is paramount, as it greatly influences the final microstructure, mechanical attributes, and corrosion resistance exhibited by metal components manufactured via LPBF. The melt pool, defined as the region of molten material genearted by the laser's action, plays a vital role in governing the fluid movement and consequently the microstructure and final properties of the material. Consequently, investigating the mechanisms of formation and stability of both single-track and multi-track melt pools derived from LPBF processes has the potential to unveil solutions and understanding that can address defects, enhance properties, and accelerate innovation within the realm of diverse metallic materials.

The fundamental action of a laser beam in this process lies in its ability to induce melting and subsequent fusion of powder particles through focused heat. This involves complex physical and thermal dynamics. A moving Gaussian laser beam creates a melt pool which is far from stable and is undergoing continuous change, subject to forces such as those arising from

material ejection (recoil), surface adhesion (wetting), the interaction between liquid and boundaries (capillary), and the gravitational force. The liquid metal's tendency to move within the melt pool, shaped by its surface tension and viscosity, is predominantly steered by the capillary forces that affect its hydrodynamic behavior and result in the constant fluctuation in the pool's size and shape during the LPBF. Variations in the melt pool's form can range from subtle deviations linked to a state approaching equilibrium to extensive fluctuations with constantly changing irregular geometries, depending on the specific processing settings chosen. The final structure of the material after it has re-solidified is substantially influenced by the interaction of the molten material with the surrounding powder; i.e., wetting. Deficient wetting or melting leads to the formation of spherical particles, a phenomenon identified as balling, which arises due to the Plateau-Rayleigh instability [31]. These structural anomalies have the potential to impact the uniformity of the next powder layer significantly. This is because an irregular, corrugated surface on the previous layer can then promote typical process defects, especially defects related to insufficient bonding between layers. Effectively eliminating these imperfections to produce a solid interface between subsequent layers calls for a stable and wellmanaged melt pool. This is achieved by using optimized manufacturing settings to achieve the remelting the appropriate amount of the preceding layer.

In Laser Powder Bed Fusion (LPBF), the process gives rise to several intertwined thermal phenomena (as shown in Figure 10), all of which substantially influence the way the build solidifies, the resulting microstructure, and the material characteristics of the final component. These thermal phenomena incorporate how the laser and powder interact, the quick heating process, the Marangoni effect, and the ways heat is transferred through conduction, convection, and radiation. Crucially, these thermal events also significantly affect the stability, movement, and solidification dynamics of the molten pool. The LPBF method produces intense temperature gradients inside the molten pool, leading to complex, temperature-dependent hydrodynamic flows. These flows, in turn, can cause the formation of spatter. In particular, the high-velocity liquid at the surface may splash over onto the surrounding powder layer during the laser scanning of the molten track. This is a consequence of the surface tension influences stemming from the vigorous surface convection flow, commonly known as the Marangoni convection effect, especially in the transitional area. When this spatter re-solidifies, it can cause surface imperfections or uneven fusion on subsequent tracks, since the spatter may not become completely incorporated into the previously built layer. Further, the recoil force, or pressure, which is created from the metal vapor genearted by the laser, also drives the melt flow. When

there is sufficient energy to vaporize metallic elements and produce plasma, external forces from the recoil momentum disrupt the flow and create surface depressions.

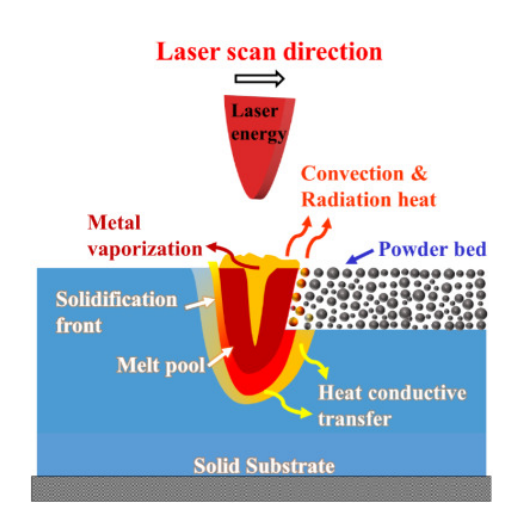


Figure 7: thermal phenomena occurring during LPBF

Melt pool models are indispensable for thoroughly simulating the LPBF manufacturing process, serving to forecast defect formation like lack of fusion, porosity, residual stress build-up, and cracking. They also aim to predict the resulting microstructure and mechanical attributes of the final component. To meet these objectives, melt pool models integrate several influential parameters. They consider aspects like laser scan velocity, laser power output, powder bed characteristics, and powder particle characteristics to anticipate the shape, dimensions, and temperature distribution fluctuations within the melt pool. Furthermore, the models factor in the heat exchange dynamics between the melt pool and the surrounding powder bed, along with the solidified material. The numerical outcomes demonstrated that the laser energy density plays a significant role in influencing the geometric properties, irregularities, and the presence of discontinuity boundaries within the melt pool. For example, simulations confirm that inadequate energy densities can lead to discontinuities and irregularities in individual melt tracks, arising from lack of fusion. Conversely, excessively high energy densities can cause over-burning and the creation of voids because of metal fluid evaporation and the subsequent disruption in the melt track formation within the melt pool. Furthermore, excessive energy input can initiate turbulent flow inside the melt pool, leading to compromised surface finish owing to the spattering effects driven by recoil pressure. Consequently, a planar flow of molten liquid within the melt tracks can enhance the overall stability of the melt flow. Therefore, achieving an optimized energy density is critical; doing so allows a stable, planar fluid flow to be achieved

in the melt pool. This, in turn, fosters superior wettability between the substrate and the melt layer, resulting in a smooth scan track [34].

Figure 8 presents a simulation of a single-track melt pool's creation, viewed in cross-section. This emphasizes the development of depression zones and their temperature variations within the melt pool itself. The region directly below the laser spot experiences the strongest recoil pressure. This pressure's dominance stems from its exponential relation to temperature. This includes the process of the formation and subsequent collapse of these indentations. Also, this results in an uneven flow pattern and can contribute to the creation of pores, a consequence of the melt pool's asymmetrical cooling. As the surface temperature climbs near the boiling point, the recoil pressure intensifies, exerting a substantial force perpendicularly against the surface. This drives the liquid away from the melt pool's center at an accelerated rate. The sides of the melt pool, where liquid spills, trap and draw in nearby particles. They get incorporated behind the depression, which forms a "denudation zone" along the track's edges, characterized by the removal of powder [35], [36].

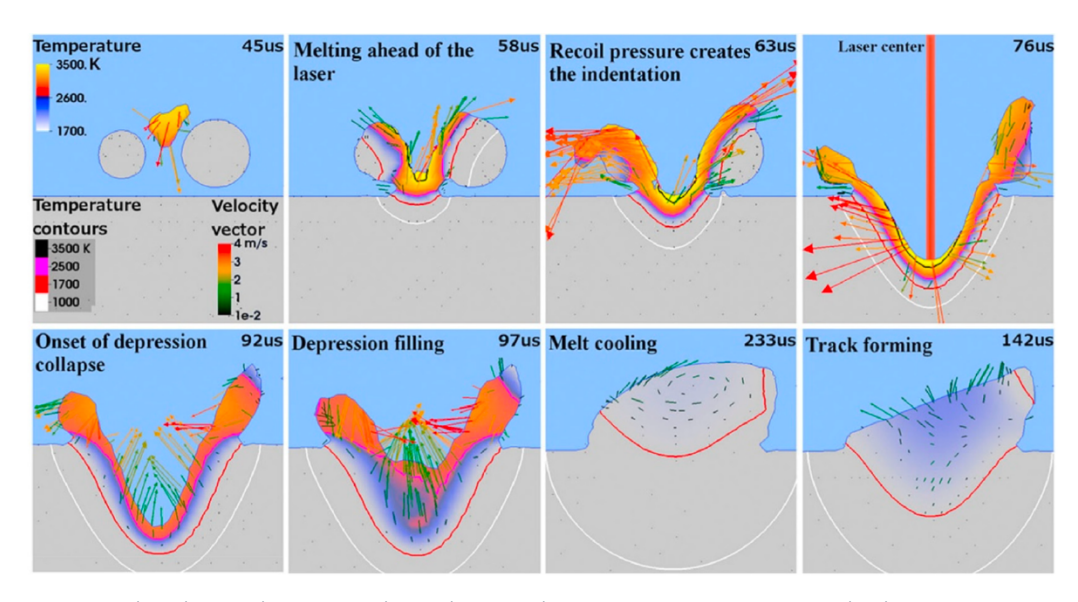


Figure 8: cross section view of single track simulation showing the temperature and velocity field of the melt pool as the laser scans.

The characteristics of the melt pool critically influence how the powder melts, solidifies, and interacts with the solid powder particles through wetting. These highly dynamic melt pools arise due to diverse processing parameters that contribute to the various melt pool types [37]. Figure 9 (a) and (b) visually present the conduction mode and the keyhole mode of the melt pool, respectively. Compared to the conduction mode, the keyhole mode features a more

extensive zone of remelting, significantly influencing the solidified layer properties dependent on the existing melt pool mode. The conduction mode corresponds to lower energy density while the keyhole mode is linked to higher energy density. The specific form of the melt pool fundamentally governs the direction of the thermal gradient, namely perpendicular to the melt pool's boundary. This directional influence leads to distinct microstructure formation variations [38].

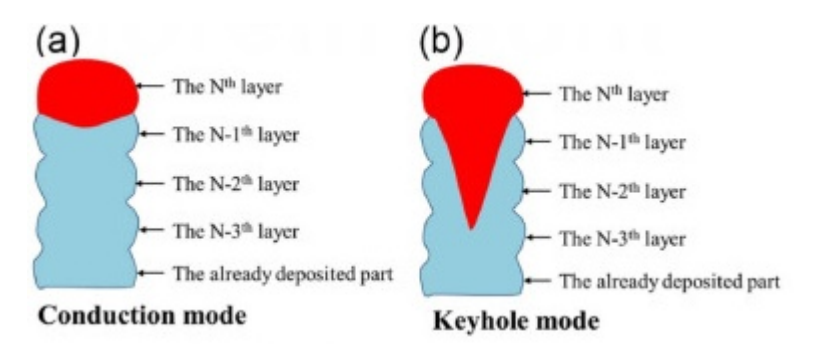


Figure 9:schematic illustration of heat transfer history for a (a) conduction mode and (b) key hole mode.

The solidified melt pool exhibits a variety of microstructures, including equiaxed grains, columnar dendrites, dendrites, cellular structures, and planar structures (see Figure 13). It is worth noting that cellular or columnar dendritic microstructures are frequently observed in conventionally processed metal alloys, which is attributable to moderate temperature gradients and solidification rates. Grain development within the melt pool is significantly impacted by the temperature gradient and the rate of solidification, representing two main thermal parameters. The temperature gradient (G) influences the direction in which grains grow, while the solidification rate (R) dictates the size of the grains [105]. A solidification map can be genearted using G and R, combining G \* R and G/R. The grain morphology of the solidified structure is determined by the slope (G/R) of this graph, while the grain size is determined by the product of G \* R . Based on the genearted solidification map, elevated cooling rates result in finer microstructures, and conversely, reduced cooling rates result in coarser structures.

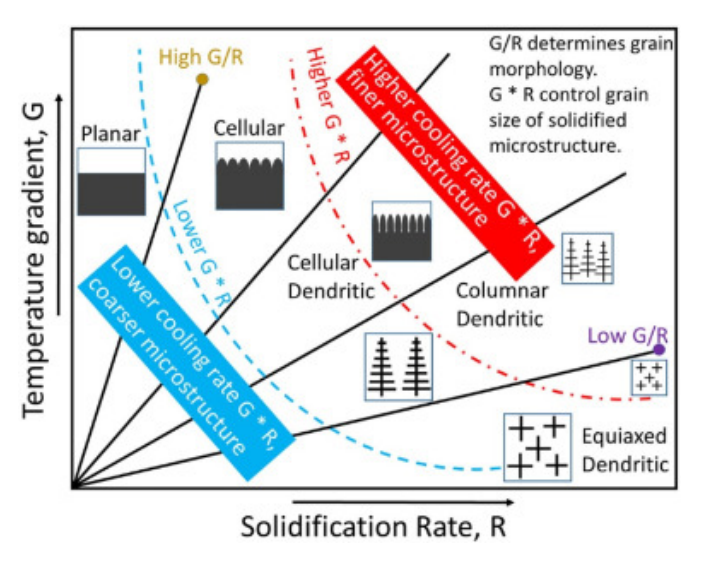


Figure 13: relationship between temperature gradient, solidification rate and the resulting grain size and morphology of a solidifies microstructure

Laser Powder Bed Fusion (LPBF) technology, as a rule, employs metallic powders as its feedstock, culminating in a component fabricated via complete melting of that powder. Notably, the characteristics of the powder, encompassing its type, granulometry, particle form, chemical make-up, melting point, and boiling point, can significantly influence the melt pool's depth, size and shape [43]. These factors contribute directly to the emergence of imperfections during the LPBF procedure. By carefully fine-tuning the powder particles, the viscosity of the molten pool can be elevated, thus refining the excellence of the build part [44]. Furthermore, the attribute of effective powder flowability is indispensable for accomplishing a uniformly consistent spread, whilst a favorable powder packing density supports the creation of a consolidated powder layer, leading to enhanced component density.

## 2.3. Approaches to PBF-LB of γ' Ni-based superalloys

### 2.3.1. Effect of PBF-LB process parameters on cracking density

Several studies in scientific publications have investigated the impact of the pivotal PBF-LB process variables on the crack density observed within  $\gamma'$  Ni-based superalloys. Broadly, the tendencies concerning crack density in relation to the principal parameters, specifically power, laser scan speed, and hatch spacing, aree in agreement acrosso the literature. An increase in power levels demonstrably intensify the cracking issues prevalent in these specific alloy types. Decreasing power forms a shallower and narrower melt pool as well as a lower peak temperature that results in decreased crack density.

Evidence distinctly indicates a negative correlation involving laser scan speed; when the scanning velocity is increased, the resulting melt pool becomes less deep and less wide. This modified pool tends to stretch out in the direction of the scan. As a rule, this adjustment leads to a lower concentration of cracks. Furthermore hatch spacing and layer thickness were both positively correlated to crack density, in fact low crack densities were genearly observed when low hatch spacing or low layer thickness was used.

Energy densities provide a mechanism for merging principal PBF-LB settings into one metric, maintaining physical meaning, which is then often employed for process improvement. The Volumetric Energy Density (VED) constitutes one such type, especially pertinent when analyzing multi-layer constructions. This is calculated using  $VED = \frac{P}{vht}$ , where the laser power (P) is divided by the laser speed (v), hatch spacing (h), and layer thickness (t), and has units of  $J/mm^3$ . VED increases as more energy is added into a specific volume, either with an increase in laser power, decrease in laser scan speed, decrease in hatch spacing, or decrease in layer thickness. The variable is frequently shown to predict the typical defects formed in PBF-LB, such as lack of fusion defects at low VED and gas porosity at high VED [45].

.

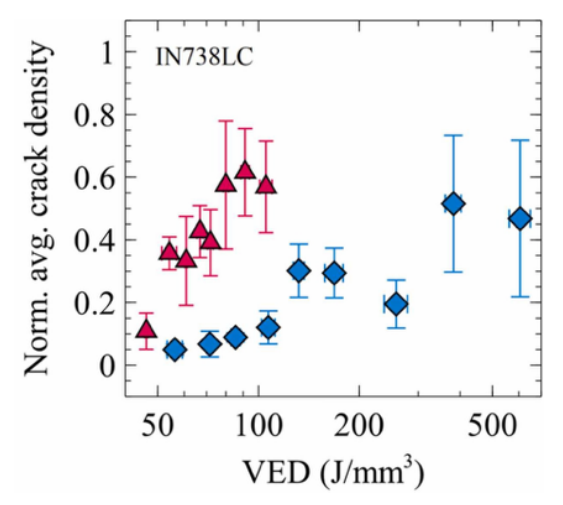


Figure 10: effect of VED on crack density for IN738LC.

Several research explore the connection between process parameters and strain age cracking, which is a phenomenon that appears during the post-process heat treatments. It has been discovered that a reduced Volumetric Energy Density (VED) offered dual benefits. Specifically, it contributed to a lower concentration of both solidification and liquation cracks during the PBF-LB method. Moreover, lower residual stress levels were also observed as a result. Because of this, the lower residual stress will limite the degree of strain age cracking that may subsequently occur during the heat treatment stage.

It is advisable to adopt a cautious approach when considering volumetric energy density (VED) as the sole parameter for reducing crack density in PBF-LB processes. Specifically, the formation of highly porous material due to lack of fusion at low VED has been reported. These voids effectively fill spaces that, by conventional crack density assessments, would be classified as "crack-free." Furthermore, these voids mitigate residual stress within the material, thereby diminishing the propensity for cracks to develop in the more compact regions [47]-[48].

### 2.3.2. Post Processing on micro-cracking defects

Although low γ' Ni-based superalloys can be processed with PBF-LB to form dense, crack-free material, higher  $\gamma'$  Ni-based superalloys typically require post-processing to address internal defects. These additional treatments are typically applied alongside the standard heat treatments already deemed essential. The initial step usually involves hot isostatic pressing (HIP). Hot isostatic pressing (HIP) is usually performed first, in which a high pressure and high temperature environment are used to soften and compress a material, closing internal defects. Subsequent to this, a solutionizing stage homogenizes the material's microstructure, and an aging process develops the  $\gamma'$  strengthening phase. This strengthening phase arises from nucleation during the cooling phase following the solutionizing treatment. Hot isostatic pressing has demonstrated its effectiveness in mending flaws within even the most cracksusceptible y' Ni-based superalloys. Nonetheless, instances of surface-connected cracks were detected within the alloy following HIP. Various researchers have highlighted this surfacerelated constraint associated with the application of HIP to cracking defects. A common solution revolves around ensuring cracks are small and kept separate. The crack width, representing the spatial separation between crack faces, is a crucial factor in determining the success of crack healing. Cracks less than 6 µm wide in a PBF-LB IN738LC alloy showed complete closure, in contrast to wider cracks which persisted post-HIP. This discrepancy was linked to the distance limitations intrinsic to the diffusion mechanism that acts to close cracks during HIP. In genearl, even when HIP is effective, the post- HIP microstructure is not completely free of defects.

A new form of low pressure HIP reminiscent of the supersolidus liquid state sintering sometimes used to post-process binder jetted parts was demonstrated on an IN738LC alloy. The advantage of this particular technique is its capability to handle surface-connected cracks, a type of defect that traditional HIP methods struggle to mend. This method, known as liquid-induced healing (LIH), subjects the material to vacuum heating, bringing its temperature above the melting point of the grain boundary's low-melting-point eutectic, followed by the application of minimal pressure and subsequent cooling. Since solidification and liquation cracks necessitate tensile stress to develop, the slight isostatic pressure being applied induces a helpful compressive stress, effectively stopping cracks from reforming [51].

The presence of defects is affected by solutionizing and subsequent aging heat treatments. It has been observed that solutionized and aged IN738LC, or directly aged IN738LC, demonstrated fewer micro-cracks in contrast to the as-built state. This diminished number of sharp features was explained by a "sintering effect", yet no changes were detected in pore

defects. The lowest micro-cracking severity occurred after 2 hours at 850 °C, with a subsequent rise in crack density below and above this temperature. Cracking at lower temperatures was associated with a ductility dip cracking mechanism, whereas cracking at elevated temperatures was linked to strain age cracking. Neither investigation revealed fully healed material, making a hot isostatic pressing step essential for most researchers to achieve a dense, crack-free material . Macroscopic cracks, larger in size, have also been observed to develop during thermal processing; a strain age cracking mechanism has been proposed as the root cause. The growth of large cracks along high angle grain boundaries in an IN738 alloy has been documented. The combination of residual stresses, inherently present due to the PBF-LB technique, with stresses arising from the precipitation of  $\gamma'$  during the heat treatment phase, caused the localized grain boundary strength of the alloy to be exceeded, leading to crack formation. Despite the high solutionizing temperature which is intended to relieve PBF-LB induced residual stresses, the process of ramping up to the designated hold temperature subjects the PBF-LB material to a temperature range conducive to  $\gamma'$  precipitation and subsequent enlargement. Possible solutions for this problem include the adjustment of processing parameters to diminish post-PBF-LB residual stresses, utilizing extremely swift ramp-up periods to minimize excessive  $\gamma'$  growth, or implementing surface peening treatments.

### 2.3.3. Effect of chemistry modification on cracking density

Chemistry modification has also been proposed in literature to enable the processing of  $\gamma'$  Nibased superalloys using PBF-LB, which focuses on the role of minor alloying elements and trace elements in cracking. Besides, there have been attempts to create new alloy chemistries using computer simulations. The main goal is to improve the material's workability, aiming at the reduction of cracks without a performance compromise. An important parameter impacting solidification cracking is the solidification temperature range. This range manifests as a "mushy zone," which encompasses solid and liquid phases. Within PBF-LB, this mushy zone usually contains solid cells or dendrites surrounded by a liquid phase, which has higher concentrations of low-melting elements. Genearlly, an extended solidification temperature range corresponds to a physically more expansive mushy zone, therefore heightening vulnearbility to solidification cracking as a result of elevated localized strains, as well as inefficient backfilling.

In order to reduce the size of the mushy zone and the solidification range, alloy modification is frequently studied. The primary goal is often to minimize the presence of low melting point elements. These elements tend to preferentially concentrate in the liquid phase during solidification, consequently lowering the effective solidus temperature. But, given that Ni-based superalloys possess very complex compositions, the kind and proportions of alloying elements can differ greatly depending on the specific alloy. Consequently, evaluating the impact of each alloying element necessitates a comprehensive view of both how the alloy behaves during manufacturing (processability) and its eventual effects on the alloy's strength and behavior.

In this context, the IN738LC alloy represents a valuable reference. This nickel-based superalloy, hardened through precipitation, excels in high-temperature applications such as gas turbine components, due to its excellent creep resistance and oxidation behavior. Notably, it shares a similar chemical composition and phase architecture with the SAM alloy, which is the main subject of this thesis. Importantly, IN738LC has a chemical composition and phase architecture analogous to SAM, which forms the core subject of this thesis. SAM, a nickel-based superalloy created by Siemens Energy, is deployed in critical structural components within turbines. These components endure significant thermomechanical stresses, mandating materials with exceptional characteristics.

For this reason, a detailed analysis of the alloying strategies applied to IN738LC, particularly those aimed at reducing crack density, can provide meaningful insight into the design rationale behind SAM's composition. In particular, the addition of hafnium (Hf), identified as a promising alloying element for improving crack resistance in LPBF-processed IN738LC, will

be examined. The incorporation of Hf was specifically intended to mitigate strain age cracking, a critical issue for these alloys during post-processing heat treatments. This same element has also been introduced into the SAM alloy formulation, making the comparison between the two systems especially relevant and consistent.

## 2.3.4. Chemistry modification in Inconel 738LC

Nickel-based superalloys, strengthened by  $\gamma'$  precipitates, present welding challenges; cracking is a common issue. The elevated levels of Al and Ti in these alloys (like RD88T and IN738LC, typically around 6–7 wt.% combined) are a primary contributing factor [55].

Liquation cracking and solidification cracking are widely recognized as the dominant cracking mechanisms in precipitation-hardened superalloys like IN738LC during Selective Laser Melting (SLM). During the repetitive heating and cooling experienced in SLM, liquid films develop at grain boundaries, ultimately leading to cracks under tensile stress. Consequently, it becomes critical to mitigate the persistence of even a small fraction of residual liquid phase across a broad temperature range within IN738LC. This holds true whether the liquid films originate from the direct liquation of eutectic phases or through constitutional liquation.

Suppressing cracking in SLM-fabricated IN738LC might be achieved by adequately replenishing the molten metal during the SLM process itself. In the context of joining and welding nickel-based superalloys, Hafnium (Hf) functions as a melting point depressant [56]. Incorporating Hf lessens the propensity for cracking within the Heat Affected Zone (HAZ) of these alloys. Furthermore, it expands the mushy zone and maintains a liquid link between the micro-scale molten pools, a critical factor in deterring cracking within SLM-processed IN738LC. The advantageous fluidity of the Hf-enriched melt permits crack closure at a comparatively lower temperature, consequently imparting favorable castability to the alloy [57]. SLM processing, characterized by its repetitive rapid melting and solidification cycles, bears a similarity to multi-pass welding techniques. Within this study, utilizing a uniform mixture of IN738LC powder with Hf micro-particles is anticipated to prevent macroscopic segregation in the as-printed sample. Moreover, this approach ensures a consistent reduction in melting point and a corresponding uniform enlargement of the mushy zone.

The inclusion of Hf brings about a reduction in the temperature range associated with the liquid phase mass, specifically the fraction under 2% (Figure 11). This diminished temperature window for the small portion of remaining liquid phase is crucial, as a broad range is detrimental to preventing cracks. In IN738LC, this range, representing less than 2% liquid

phase, is approximately 29 °C. However, the addition of Hf leads to a substantial decrease in this range. Specifically, with a 2% Hf addition, the range is sharply curtailed to 10.5 °C. Concurrently, the temperature range where the liquid phase exceeds 5% expands considerably, going from 62.7 °C in IN738LC to 116.9 °C when 1% Hf is present and reaching 164.8 °C with a 2% Hf concentration. Furthermore, the Scheil-Gulliver solidification diagrams (Figure 12) illustrate how Hf additions expand IN738LC's solidification interval. This range grows from 249 °C to 577 °C with the inclusion of 1% Hf, and further to 669 °C with 2% Hf. Consequently, the alloy's ability to be refilled with molten material is enhanced. This is achieved by enlarging the temperature window where a significant portion of the material remains liquid, while simultaneously shrinking the region where only a minimal liquid fraction persists [58].

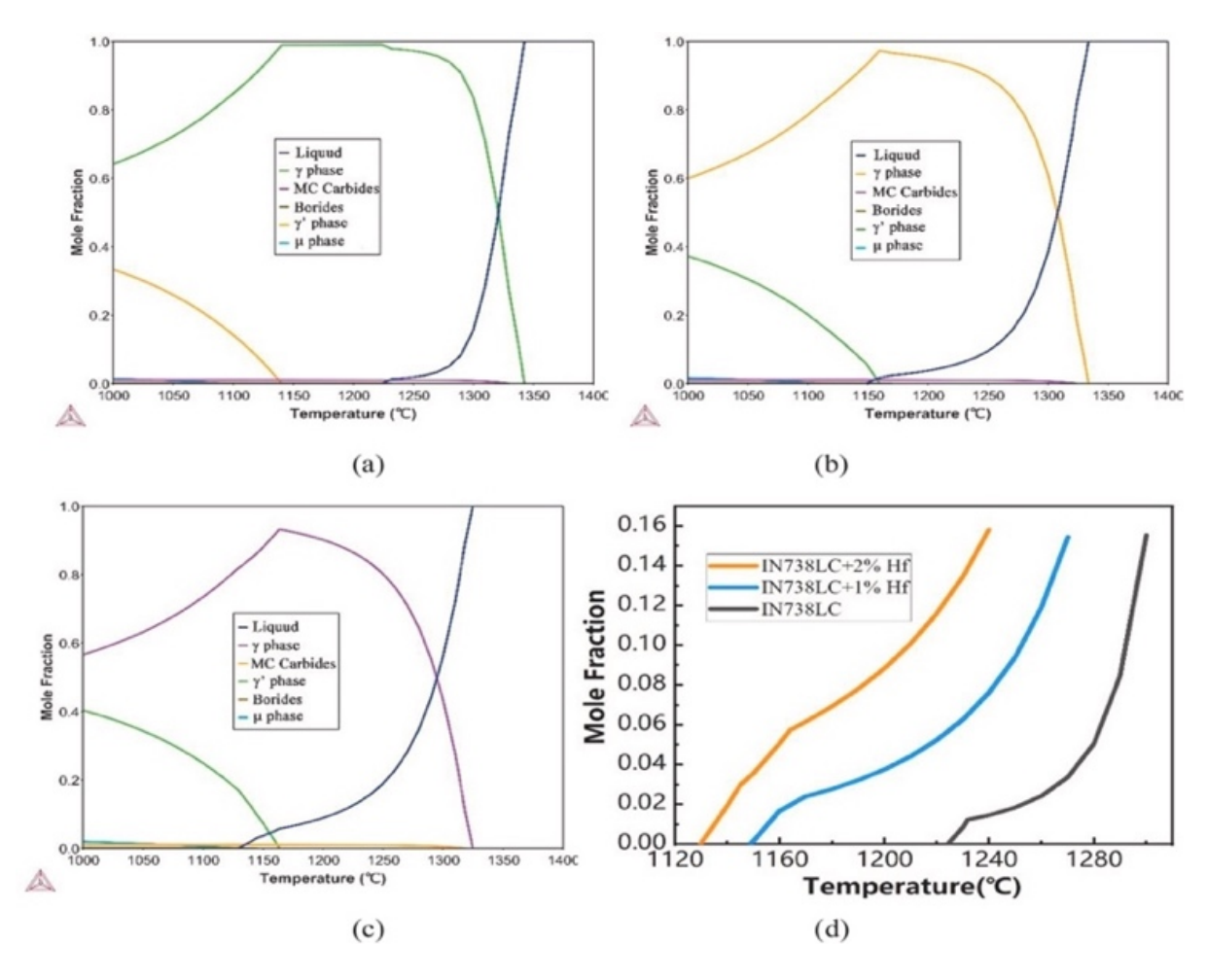


Figure 11: Change of phase transformation and liquid phase mass fraction with respect to temperature for IN738LC(a), IN738LC+1%Hf(b), IN738LC+2%Hf(c) calculated by ThermoCalc, (d) the liquid phase fraction in the last 15% liquid of three composition [58].

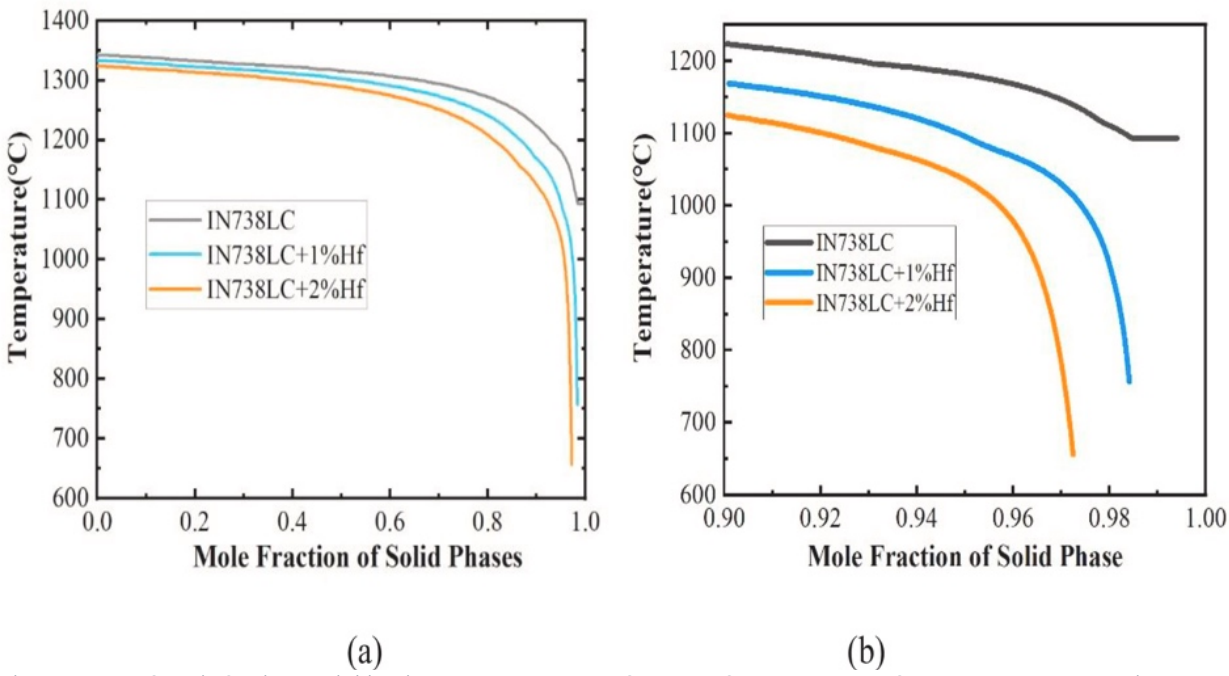


Figure 12: The Scheil-Gulliver solidification curves for IN738LC, IN738LC+1%Hf, IN738LC+2%Hf (a), and the solid phase fraction in the last 10% liquid of three composition (b) [58].

Pure Hafnium, with a melting point set at 2227 °C, far surpasses the liquidus temperature of IN738LC, hovering around 1340 °C. This temperature difference implies that the energy required to initiate both the melting process in the combined powder form and the subsequent interdiffusion will need a greater energy supply. The insufficient energy input induces the incomplete melting. The addition of Hf even deteriorate the microstructure and reduce the relative density. However, once the energy input is sufficient to melt the mixed powder, the cracks are eliminated by the Hf additive (Figure 13) and the relative density dramatically enhanced.

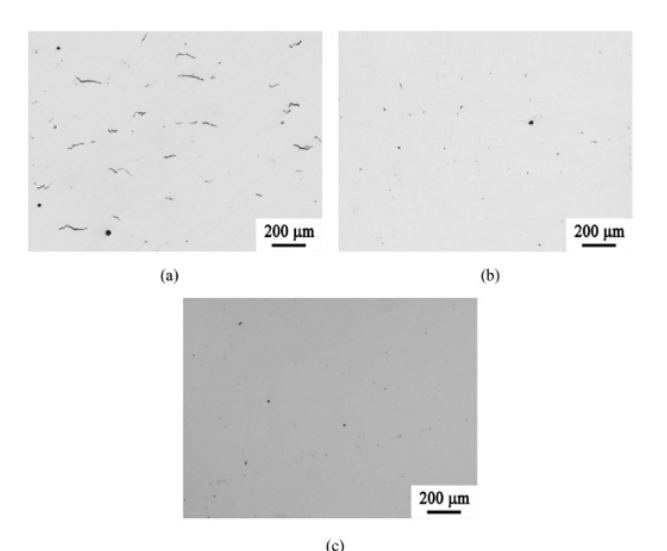


Figure 13: Metallography of as printed IN738LC (a), IN738LC+1%Hf (b), and IN738LC+2%Hf (c).

The nickel-based superalloy IN738LC, strengthened by  $\gamma'$  precipitation, is a common choice for turbine blades operating at temperatures below 900°C. Consequently, the focus is the high-temperature mechanical behavior achieved through standard heat treatment. The inclusion of Hf in the as-printed IN738LC effectively mitigates cracking across a broad spectrum of manufacturing parameters. As a result, the IN738LC+1%Hf variant demonstrates tensile properties at 700 and 850°C that are reasonably favorable, mirroring the characteristics of its cast counterpart, even when non-optimal processing parameters are applied. Further analysis shows the tensile properties are similar to those achieved with the IN738LC alloy under optimized parameters. Precise control over parameters during SLM is essential for IN738LC; however, this strictness is alleviated through the addition of Hf.

By introducing Hf, crack formation is suppressed, and the tensile properties are improved over a wide parameter range, thereby significantly enhancing the SLM processing feasibility of IN738LC. These findings present a genearl approach for curtailing the formation of cracks in  $\gamma$  precipitation strengthened nickel-based superalloys.

## 2.3.5. The material object of this work

Building upon the knowledge acquired from analyzing the IN738LC alloy, this study now shifts its attention to a closely related material: the SAM superalloy, which is the principal subject of this study. This nickel-based superalloy, SAM, was created by Siemens Energy with the purpose of serving high-temperature structural roles in gas turbines. In such applications, parts encounter substantial thermal and mechanical stresses. Similar to IN738LC, SAM exhibits a propensity to cracking when processed via the laser powder bed fusion (PBF-LB) method; strain age cracking is a primary concern in  $\gamma'$ -strengthened alloys. To tackle this issue, an alloying technique was utilized that emulates the strategy employed for IN738LC. It involved the carefully considered addition of hafnium (Hf). The presence of Hf is intended to improve the alloy's resistance to crack formation by influencing grain boundary cohesion and mitigating stress-induced damage during post-processing heat treatments.

This nickel-based superalloy primarily contains nickel (balance), cobalt (18.5-19.5%), and chromium (13.5-14.8%) for high-temperature strength and corrosion resistance. Key alloying elements include tantalum (8.5-9.5%), aluminum (2.8-3.15%), molybdenum (2.2-2.9%), tungsten (2.3-2.8%) and hafnium (1.25-1.65%). Minor additions of boron, carbon, and zirconium enhance grain boundary strength, while trace elements like yittrium support

oxidation resistance. Impurities such as iron, nitrogen, and sulfur aree strictly limited to ensure optimal performance in high temperature environments, such as turbine engines.

The ensuing chapters will deliver a comprehensive review of the SAM alloy's chemical makeup, its microstructural traits, and the rationale behind its design. This examination will pay particular attention to how SAM counteracts cracking during additive manufacturing and thermal processing.

## Chapter 3. Materials and Methods

#### 3.1. LPBFed SAM

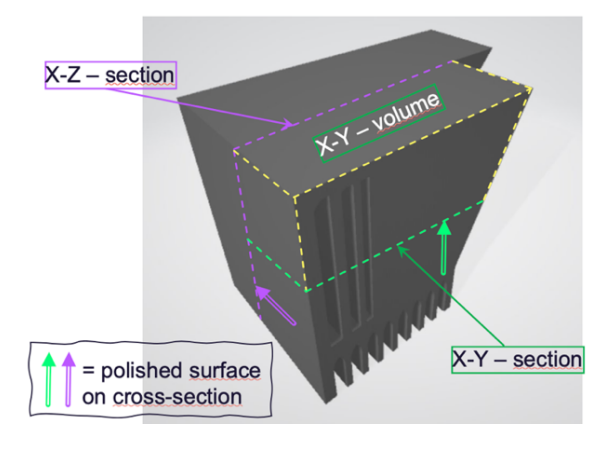
The material in this thesis work is the nickel-based superalloy SAM, produced via Laser Powder Bed Fusion (LPBF) and supplied by Siemens. The chemical composition of the alloy is presented in the table 3 below [59]. Siemens manufactured both cubic shaped and geometrically complex samples, named "Coal Carts", using LPBF process. The production was carried out on an EOS M290 machine under a protective argon atmosphere, with a layer thickness of approximately 40 micrometres. All processing parameteres employed are the result of Siemens' internal development and optimization strategies.

Table 3 Nickel-based Superalloy SAM chemical composition [59].

Powder chemical composition (wt.%)												
Element	Al	В	С	Co	Cr	Hf	Mo	Ta	W	Y	Zr	Ni
Typical	3.0	0.0085	0.025	19.0	14.0	1.45	2.5	9.0	2.5	0.04	0.03	Balance

## 3.2. Metallographic preparation of samples

In order to investigate the porosity, grain size, melt pools, thus the microstructure of the material, metalographic preparation of the samples is required. Siemens provided both cubic samples and complex-shaped samples. The cubic samples, measuring 12x12x12 mm, were sectioned along the XZ, YZ and XY planes by using a disc saw. The complex samples (referred to as coal carts), with dimension of 12x15x19.8 mm were cut along the XZ and XY plane, also using a disc saw as illustrated in Figure 14.



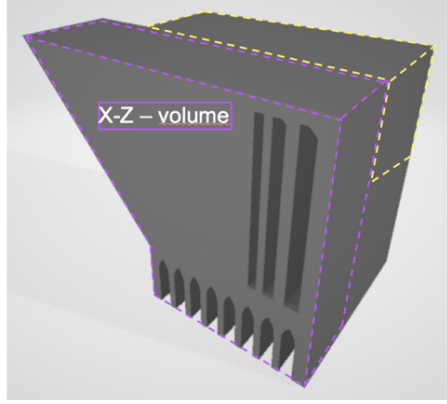


Figure 14: schematic representation of the coal cart SAM built along the building direction.

After the sectioning process, the samples were subjected to metallographic embedding to ensure stability and facilitate subsequent surface preparation. Each specimen was embedded in 20ml of phenolic resin, which was then ehated 155 °C for a duration of 30 minutes to allow proper curing and hardening of the mounting material. This step ensured the samples were securely enclosed and could withstand the mechanical stresses involved in grinding and polishing. Once the embedding was completed, the mounted samples underwent a sequential grinding process using specialized abrasive papers. The grinding was performed manually and semi-automatically, starting with a coarse grit size of 180  $\mu$ m and progressively moving to finer grits up to 2400  $\mu$ m. This step was crucial to remove surface irregularties and any deformation layers introduced during cutting. Subsequently, the specimens were subjected to a multi-step polishing process using a colloidal silica suspension to achieve a high quality, deformation free surface suitable for microstructural analysis. The polishing was carried out in three sequential steps, beginning with a suspension containing particles of 6  $\mu$ m, followed by 3  $\mu$ m, and finally 1  $\mu$ m. Each stage aimed to refine the surface further, eliminate scrathces from previous steps, and prepare the sample for high resolution optical or electron microscopy.

## 3.3. Optical Microscope

Following the embedding process, the specimen were etched using Kalling's reagent No.2 prior to microscopic analysis. They were then examined using a Leica MEF4 optical microscope operated in incident light mode, without the use of polarized filters. The observations were carried out at a magnifications ranging from 50x to 200x. For the as-built cubic samples, a total of 10 micrographs were acquired for both the XZ and XY planes. In the case of the coal cart samples, 10 micrographs were collected from the central region of the sample and in correspondence with the fin structures. Once captured, the images were further processed and evaluated using ImageJ, an open-source image analysis software. This tool enables the conversion of standard micrographs into binary images, which distinguish between two phases:

- 1. White regions, corresponding to defects, sush as pores or possible cracks.
- 2. Black regions, indicating areas of fully dense material.

Through the use of ImageJ, it is possible to identify and quantify defects such as pores, cracks and lack of fusion within metallographic images. In particular, once the image is binarized, ImageJ's analysis tools allow fort the measurement of individual features such as: area, shape,

aspect rario, roundness and perimeter. By applying threshold filters and morphological criteria, it is possible to classify the different types of defects (Figure 15):

- Porosities: genearlly, appear as rounded white regions with relatively high circularity.
- Cracks: tend to be elongated features with low aspect ratios and may exhibit branching patterns.
- Lack of fusion: are typically irregular in shape, often larger and more angular, and may be aligned along the melt pool boundaries.

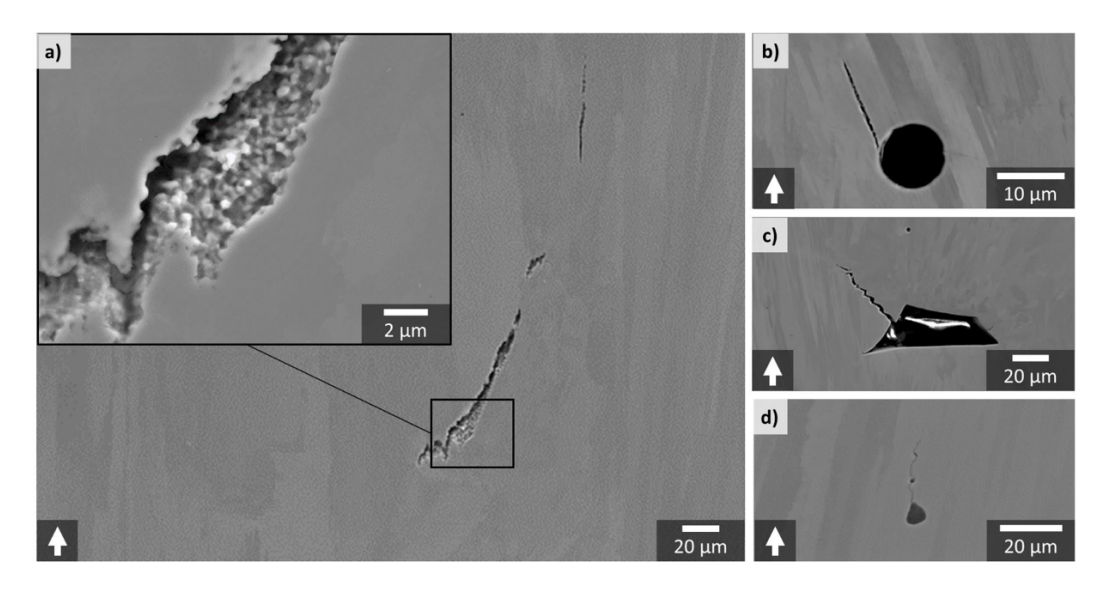


Figure 15: cross section showing typical defects in INCONEL738LC samples. (a) Formed crack located at grain boundaries, (b) gas pore, (c) lack of fusion, (d) oxide inclusion [46].

These classifications are further supported by calculating statistical distributions and visualizing the spatial distribution of the defects, which provides insights into the quality and reliability of the manufactured parts.

### 3.3.1 Grain Size Analysis

In order to determinate the average grain size, five micrographs were acquired for each cubic and coal cart sample. The analysis was conducted using ImageJ software. Grain size measurements were carried out in accordance with the ASTM E112-13 (2021) standard, specifically employing the intercept method.

In this technique, a series of test lines is superimposed on the microstructural images. The number of intersections between the test lines and the grain boundaries is then counted.

According to the standard procedure, when a grain boundary crosses a line, it is countend as one intercept. Grains that are intersected by the end points of the lines are typically counted as half grains, to avoid overstimation. This approach ensures statistical acuracy and corrects for edge effects. The mean lineal intercept lenght is then calculated by dividing the total lenght of all test lines by the total number of counted intercepts. This value is subsequently converted into the ASTM grain size number using standardized equations.

## 3.4. Scanning Electron Microscopy (SEM)

For the purpose of Scanning Electron Microscopy (SEM) analysis, the samples were electrolytically etched using a 10% oxalic acid solution in distilled water. This preparation step was essential to reveal the microstructural features of interest. The SEM investigation was carried out using a Zeiss EVO Scanning Electron Microscope, with the primary aim of analyzing  $\gamma$ ' precipitates and the carbides present in the microstructure. Micrographs were acquired using both secondary electron (SE) and backscattered (BSE) imaging modes, at magnification ranging from 5.000x to 20.000x. In addition, an Energy Dispersive X-ray Spectroscopy (EDS) probe was employed to obtain elemental composition data, allowing for a more detailed identification of the various phases and precipitates present within the alloy.

## 3.5. Melt Pools Analysis

The primary objective of this thesis is the analysis of melt pool geometries resulting from the additive manufactuirng process. In particular, five optical microscope images were acquired along the XZ growth direction for each of the three cubic samples. The images were captured at varying magnifications, ranging from 50x to 200x, in order to enusre a representative and sufficiently detailed dataset. From each image, five distinct melt pools were selected, and their geometrical characteristics, such as width and depth, were quantitatively measured using the software ImageJ. In addition to these dimensional measurements, the profile of each melt pool was reconstructed by manually identifying ten equally spaced points along the melt pool boundary. This approach allowed for a consistent and reproducibe representation of the melt pool morphology. Each reconstructed profile was subsequently interpolated using a second degree polynomial function of the form:  $y = ax^2 + x + c$ . This mathematical representation

was chosen due to its suitability in capturing the characteristics parabolic shape of the melt pools. The interpolation process was carried out for every individual melt pool profile, and the goodness of fit was evaluated by calculating the coeffcient of determination  $R^2$ . As will be demonstrated in the following chapter, the polynomial fitting yielded consistently a high  $R^2$  values, often approaching unity, which indicates an excellent agreement between the experimental data and the fitted curve. From the fitted polynomial equations, the average value of the quadratic coefficient "a" was extracted for each sample. This coefficient, which reflects the curvature of the melt pool profile, was then correlated with the Volumetric Energy Density (VED) applied during the manufacturing process. In addition to the curvature analysis, the width-to-depth ratio (W/D) of each melt pool was also calculated. This ratio serves another key descriptor of the melt pool shape and was similiarly evaluated in relation to the VED. By comparing these metrics across the different samples and processing conditions, valuable insight were obtained regarding the influence of energy input on melt pool formation and stability. A detailed analysis and discussion of the results will be provided in the next chapter, highlighting the observed trends and their implications for process optimization.

## 3.6. Differential Scanning Calorimetry (DSC)

Differential Scanning Calorimetry (DSC) is a thermoanalytical technique used to measure heat flow associated with phase transitions in materials as a function of temperature. It is effective for determining the solidus temperature and the onset of incipient melting in metallic alloys. During the DSC analysis, samples and a reference are subjected to a controlled temperature program. As temperature increases, the instrument detects endothermic or exothermic events based on the difference between the samples and the reference. The onset of incipient melting is identified by the beginning of an endothermic peak, which corresponds to the first detectable melting of low melting phases. The solidus temperature is typically associated with the end of this transition, where complete melting of the solid phase begins.

The test was conducted in a Setaram DSC/TGA furnace starting from 20 °C up to 1400 °C. Both heating and cooling were performed with a scan rate of 20 °C/min.

## 3.7 Electron Backscatter Diffraction (EBSD)

Electron Backscatter Diffraction (EBSD) is a microstructural characterization technique performed in a scanning electron microscope (SEM) to obtain crystallographic infromation from a material's surface. It allows for the analysis of grain orinetation, grain size, phase identification and crystallographic texture at the microscale. In EBSD the quality of the diffraction pattern strongly depends on the surface condition of the sample. One crucial step in the preparation processi s the use of an ultrasonic bath, typically perfromed after the final polishing stage. The ultasonic bath serves primarly to remove any residual contaminants left on the sample surface. It works by genearting high-frequency sound waves in a liquid (commonly acetone). These waves produce small cavitation bubbles that implode near the sample surface removing particles and contaminants without mechanically demaging the sample. This process ensures a clean surface which is essential for accurate pattern formation.

# Chapter 4. Microstructural Analysis

### 4.1 Phenomenological analysis of microstructure

The starting point of this work was the microstructural analysis of cubic samples with the aim of assessing the printability of the alloy and identifying any potential defects. It is worth mentioning that those cuibc samples were in a Design of Experiments (DoE) for printing parameter optimization purposes. Therefore, no relevant microstructure modifications were foreseen, particularly in terms of melt pool morphology, which should ideally be replicated in the coal charts samples. Since this assumption needed to be verified, the core of my work focused on evaluating wheter the transfer of these optimized parameters was successful or not.

### 4.1.1 Cubic Samples-Porosity

Porosity analysis was carried out on three as-built samples: N.28, N29 and N.30. Each sample was fabricated using different sets of processing parameters. The Table 4 Values of Volumetric Energy Density (VED) applied to cubic samplesbelow reports the corresponding values of Volumetric Energy Density (VED) applied to each sample.

Table 4 Values of Volumetric Energy Density (VED) applied to cubic samples

Sample	Type	Heat treat	VED
ID#			J/mm³
28	Cube	As-printed	53.6
29	Cube	As-Printed	62.5
30	Cube	As-Printed	58.0

Figure 16: microstructure of the as-built SAM cubic samples shows the microsructure of the as-built SAM cubic samples, observed along two othogonal planes: XY and XZ. Various defects can be identified within the microstructure, primarly gas porosities and lack of fusion.

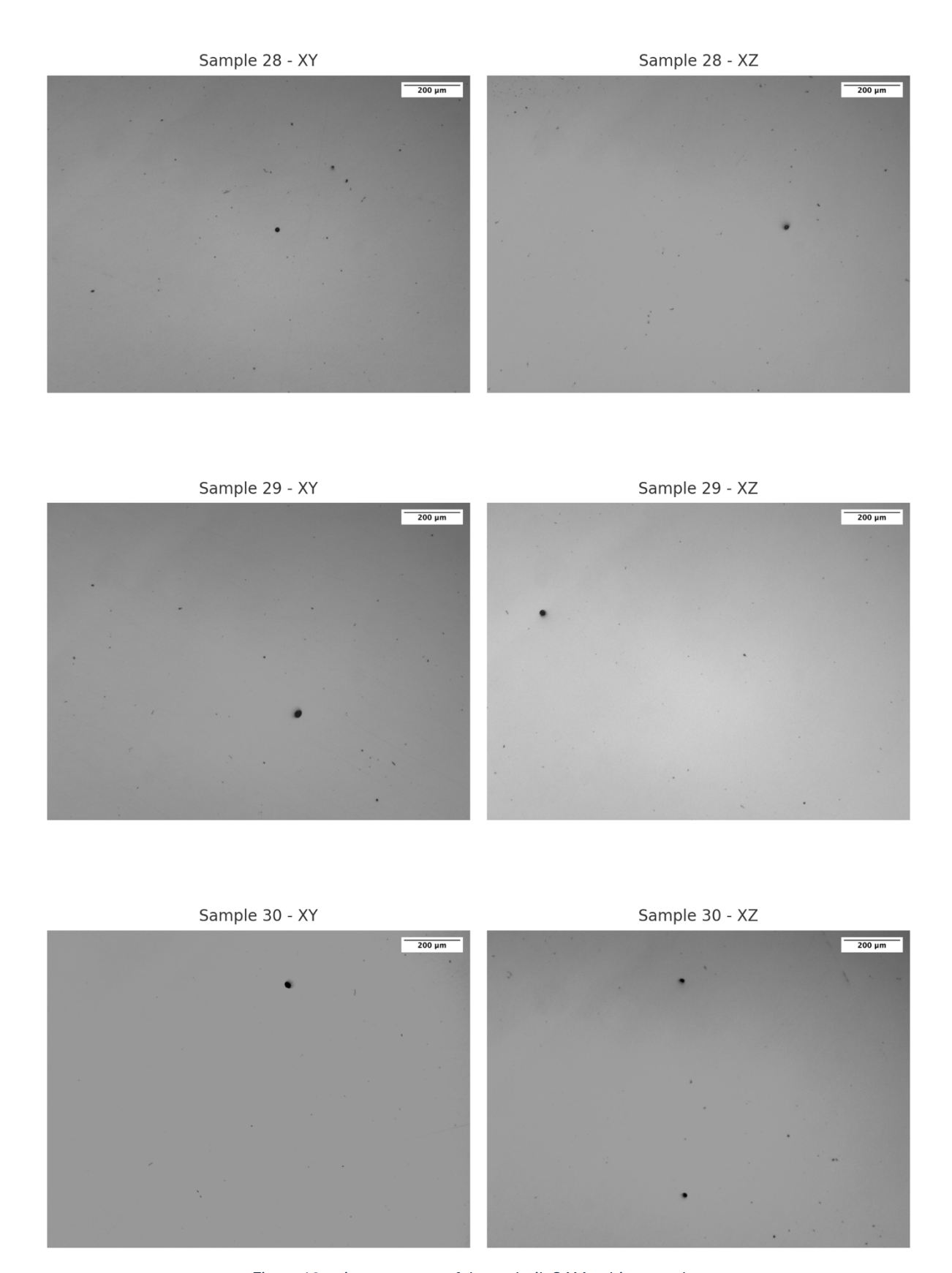


Figure 16: microstructure of the as-built SAM cubic samples

Based on optical microscopy images, it was possible to evalueate both the concentration and morphology of these defects. In particular, data were collected on the pore diameter distribution and the aspect ratio in both the XY and XZ planes for all three samples.

With regard to the aspect ratio, the corresponding histogram (see Figure 17) presents the comparison between the mean aspect ratio of pores and the corresponding standard deviation for samples 28,29 and 30.

For sample 28, the mean aspect ratio is higher in the XY direction (2.24) than in the XZ direction (1.75), and a broad distribution in pore shape is supported by a high standard deviation for the XY direction (1.83). This would suggest that pores in this samples favor elongation in the XY direction and take on more anisotropic shapes. Conversely, for the XZ direction, the smaller value for the standard deviation (0.80) supports a more isotropic shape for the pores. Sample 29 has a reversed tendency, and both planes have similar mean values (1.69 in XY and 1.84 in XZ). The standard deviation is, however, less for the XY plane (0.65) compared to the XZ plane (1.01), thus pores for this sample are more equiaxed in the XY plane. Sample 30 has comparable mean aspect ratios between the XY and XZ sections (1.77 and 1.58 respectively). The respective standard deviations (0.89 in XY and 0.76 in XZ) are indicators of moderate variability and therefore pores tend to have compact and nearly equiaxed shapes for both orientations. These results demonstrate that pore morphology is not isotropic and can vary depending on the observation plane. These anisotropic behavior, linked to the process parameters and manufacturing process, can influence the mechanical behavior of the material acting as preferential sites for stress concentration and crack initiation.

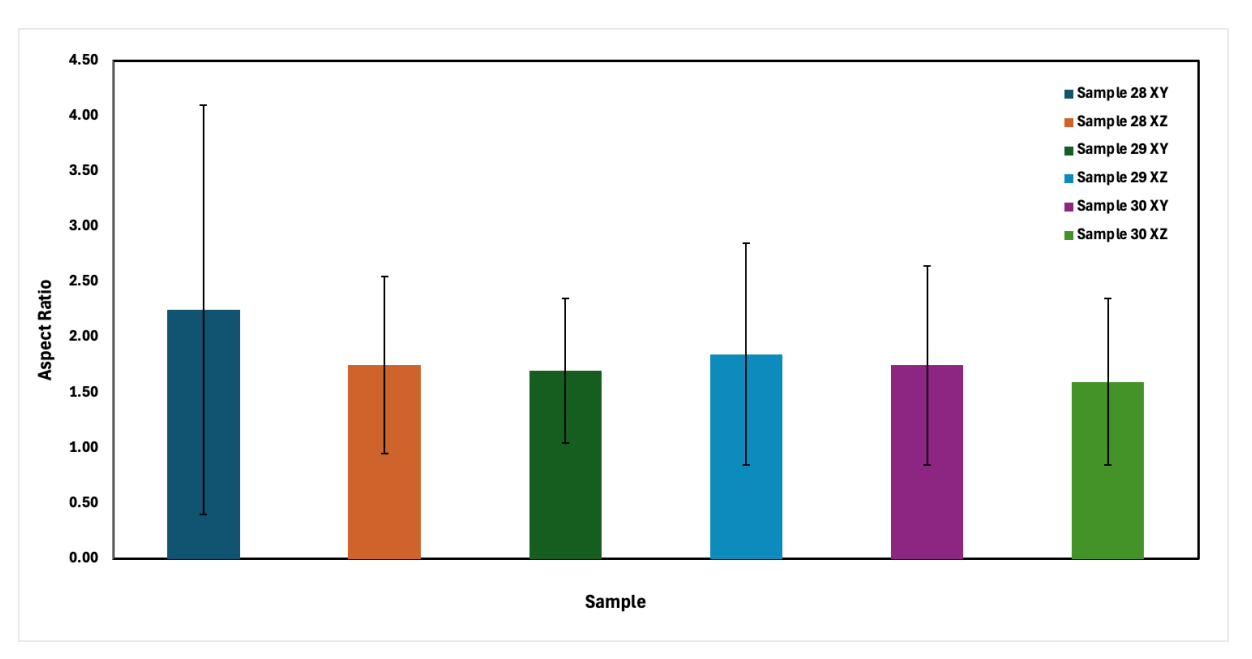


Figure 17: mean pore aspect ratio with standard deviation for Samples 28, 29 and 30 in the XY and XZ planes.

The pore diameter distribution is presented in the subsequent graphs (Figure 18-Figure 19).

All three samples exhibit a lognormal trend with a pronounced maximum in the range of approximately 4–6 units, which represents the most frequent pore size. Sample 30 (green curve) displays the sharpest peak, indicating a narrower distribution and a higher concentration of pores within this interval. In contrast, sample 28 (blue curve) presents a broader distribution with a lower maximum frequency. A secondary peak can be observed in the 12–14 unit range, most evident in sample 29 (orange curve), suggesting the presence of a smaller population of larger pores.

Figure 23 reports the pore size distribution along the XZ-plane. In this case, the distributions are characterized by a marked maximum between 3 and 5 units. Sample 28 (blue curve) exhibits the most pronounced and narrow peak, closely followed by sample 29 (orange curve). Sample 30 (green curve), on the other hand, shows a broader and less intense peak, indicating a more heterogeneous pore structure. These observations suggest that samples 28 and 29 are dominated by finer and more uniformly distributed pores, whereas sample 30 contains a wider variety of pore sizes.

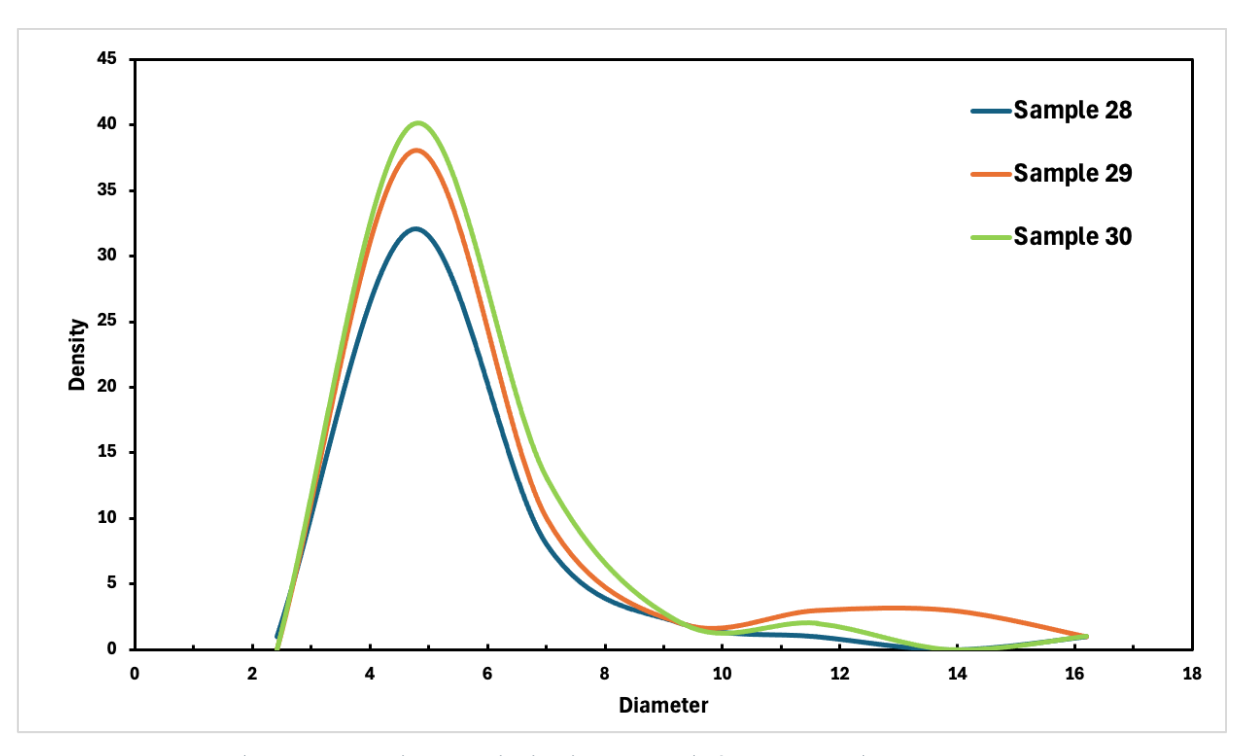


Figure 18: Pore diameter distribution of as-built SAM samples in the plane  $\it XY$ 

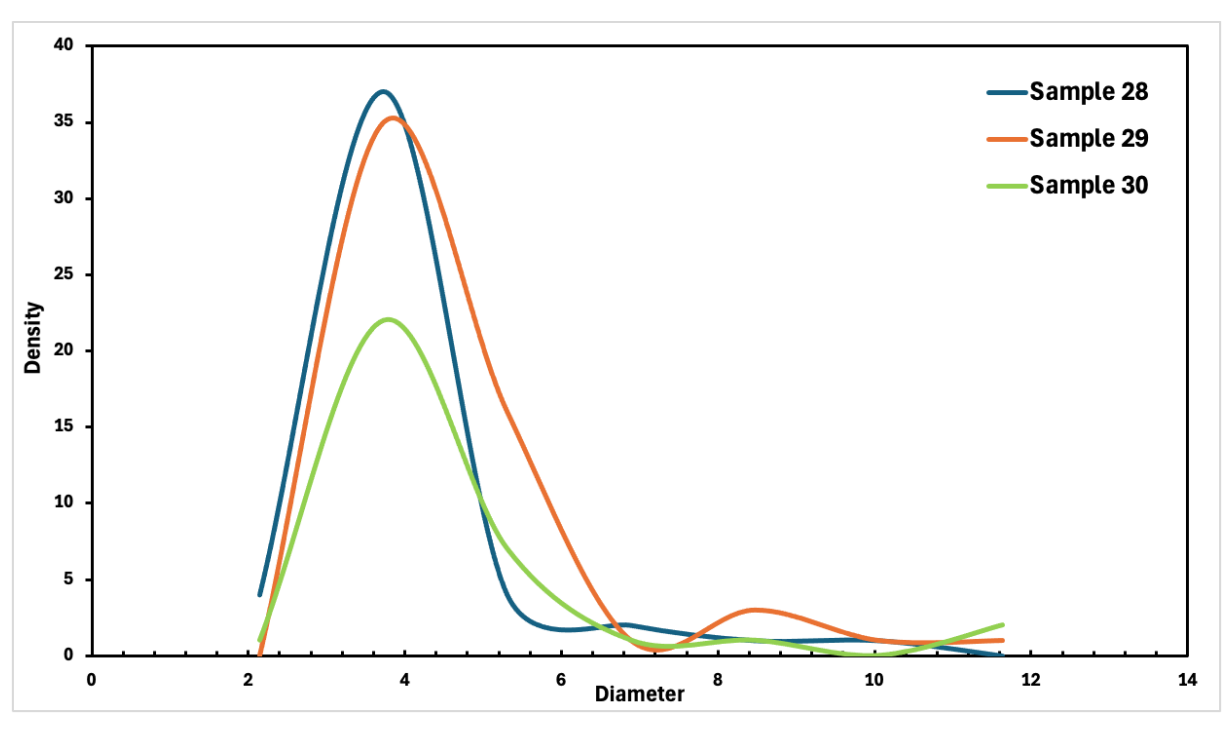


Figure 19: Pore diameter distribution of as-built SAM samples in the plane XZ

### 4.1.2 Cubic Samples- Microstructure

Following the porosity analysis, a detailed analysis of the grain structure within the microstructure was carried out. To this end, cubic samples were etched to reveal the metallographic features typical of components produced via Laser Powder Bed Fusion (LPBF). The microstructure of each sample is subsequently analyzed in detail by combining different approaches: frist through optical microscopy, then by Scanning Electron Microscopy (SEM), and finally by Electron Backscatter Diffraction (EBSD) imaging.

The analysis begins with sample 28: Figure 20 shows the microstructure of sample 28 observed along the XY-plane by optical microscopy. The image reveals the characteristic layered melt track morphology, resulting from the overlapping scanning strategy of the LPBF process. The tracks are visible as elongated, arc-shaped patterns, arranged in a overlapping sequence which refelects the laser scan path and hatch distance. The microstructure appears homogeneous with no evidence of lack of fusion defects, but at the same time local variations in track width can be observed.

Conversely, on the XZ plane (Figure 21) which is parallel to the building direction, the microstructure is dominated by elongated columnar grains. In addition, in this section, the characteristic melt pools formed during LPBF process can be distinguished. They appear as semicircular features aligned along the building direction. The repeated thermal cycles associated with the layer-by-layer process have produced regions with varying contrast, highlighting the extent of remelting and the bonfing achieved between adiacent layers.

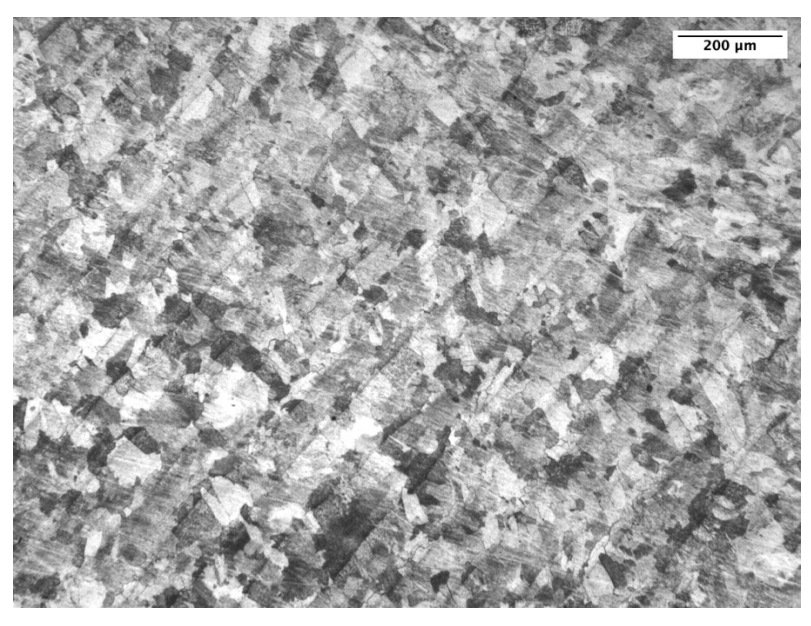


Figure 20: microstructure of sample 28 observed along the XY-plane

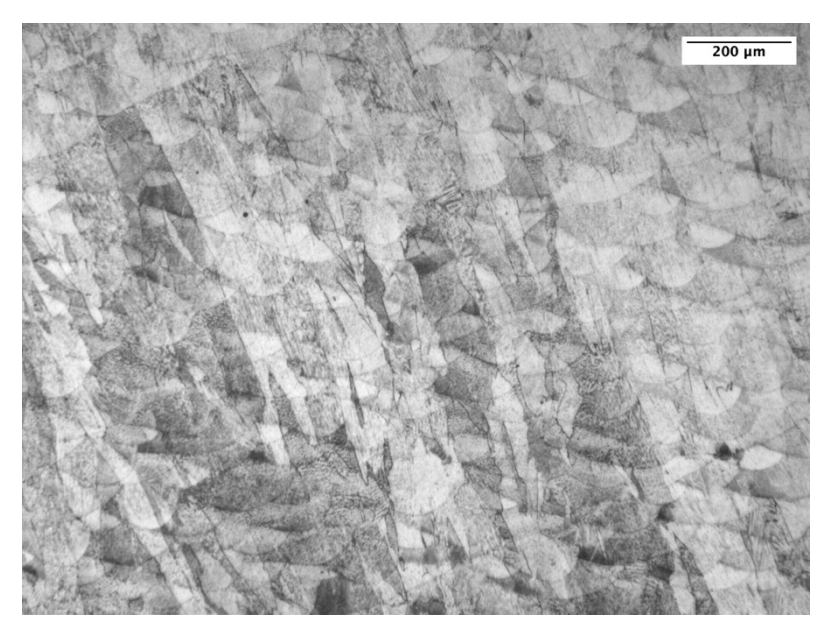


Figure 21: microstructure of sample 28 observed along the XZ-plane

In addition to the observations performed by optical microscopy, a SEM analysis was carried out in order to investigate the microstructural features and to identify possible secondary phase. SEM examination of the sample 28, across the XZ plane revealed a complex microstructure. Besides the predominant columnar grain structure aligned with the build direction, the Figure 22 (a-b) show the presence of melt pools. At the boundaries of the melt pools, contrast variations are observed, associated with segregation phenomena that have promoted the formation of Hf oxides. These precipitates are preferentially located along the interfaces rather than within the pool cores. This finding is consistent with the behavior of Hf in Ni-based superalloys: although it is added to mitigate strain age cracking, it exhibits a strong tendency to segregate in oxygen rich regions leding to the formation of stable oxides.

The microstructure is characterized by a visible and coarser cellular structure, which becomes evident within and around the melt pools. This morphology is influenced by segregation and by the loca variation in thermal gradients during solidification.

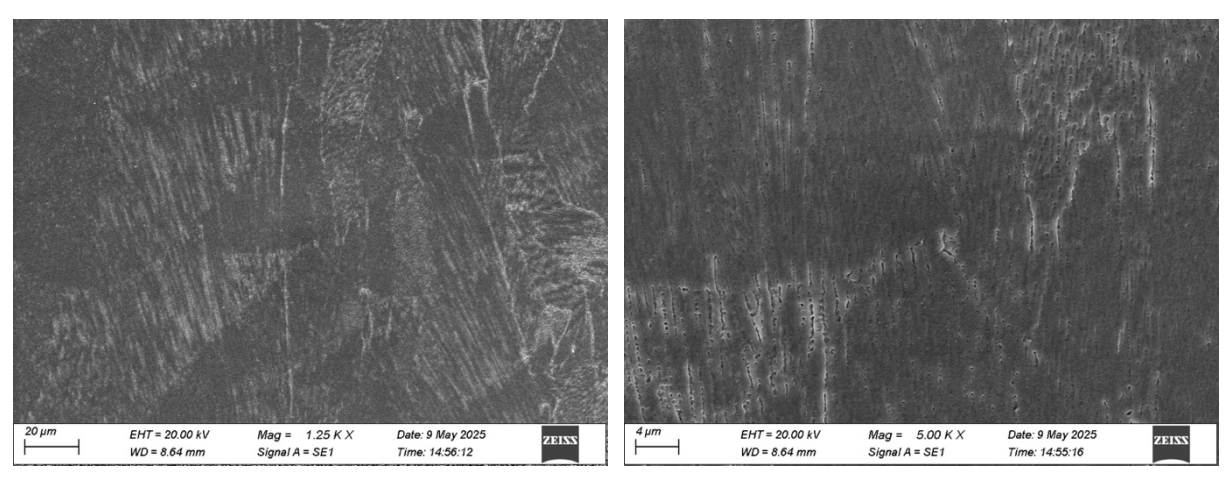


Figure 22: SEM images of sample 28 along the XZ Plane (a)-(b)

The three EBSD maps captured on sample 28 (Figure 23) provide information on crystallographic orientation, grain boundary distribution and intragranular lattice distortoin. On the initial map (BC+IPF+GB+GROD-ANG) the IPF colouting delineates grains of different orientation, howeer, GB overlayes highlight the network of grains. The GROD-ANG measure (Grain Reference Orientation Deviation, Angle) of map reflects the level of intragranular misorientation relative to a provided reference for a given grain. The map indicated that despite well definied grains, a level of internal distortion persists in the regions of the microstructure. In reference to the second map (BC+IPF+GB+KAM), KAM (Kernel Average Misorientation) ditribution of the map provides an approximation of local lattice curvature. Regions of high KAM distribution are concentrated near boundaries and at intragranular bands. The IPF and GB overlayes testify that these regions do not correspond a provided crystallographic colour but to gemoetric sites were strain is likely to accumulate. The third map (BC+IPF+GB) finally higlights the topology of boundaries and morphology of the grains. The microstructure contains a combination of a combination of equiaxed and weakly elongated grains. The preponderance of high-angle boundaries means that a percentage of the microstructure is severed by misoriented interfaces wherein the appearance of low angle boundaries delineates sub-grain partitions.

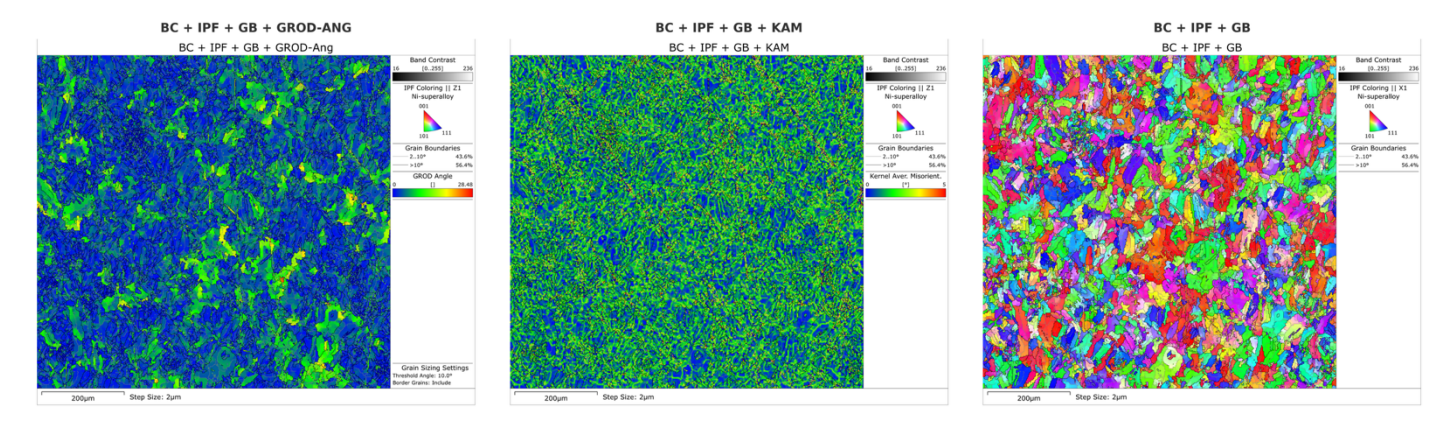


Figure 23: EBSD maps of sample 28

Following the analysis carried out on sample 28, the microstructural investigation is now extended to sample 29. The optical microscopy observation on the XY-plane of sample 29 (Figure 28-a) reveals the layered melt track patterns genearted by the laser scanning strategy. In this case the melt tracks appear less regular, with more pronounced variations in contrast across the observed area. This heterogeneity suggests a grater local variability in the width and overlap of melt tracks. On the XZ-plane (Figure 28-b), in this sample, the melt pools show a more pronounced curvature and a less homogeneous distribution compared to sample 28. The columnar structure is still evident along the build direction, although some local variations in the orientation of the melt pool can be observed.

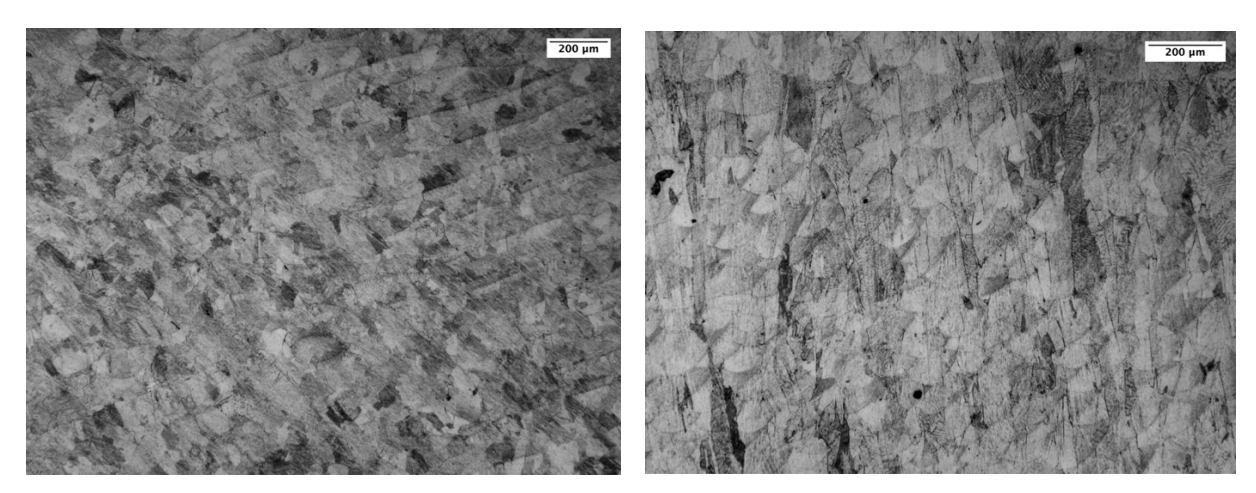


Figure 24: microstructure of sample 28 observed along the XY-Plane (a); : microstructure of sample 28 observed along the XZ-Plane (b)

Sample 29 was examined by Scanning Electron Microscopy (SEM) on the XZ section. Sample 29 shows a continuous columnar morphology aligne with the build direction (Figure 25). Across the field there is good interlayer continuity and no evident lack of fusion defects. At

high magnification, what particularly drew attention was the presence of Hf-oxide microsegregations, appearing as very fine bright precipitates distributed along cellular boundaries and at melt-pool interfaces. Their sub-micrometric size and discontinuous distribution justify referring to the mas micosegregation rather than an extended second phase.

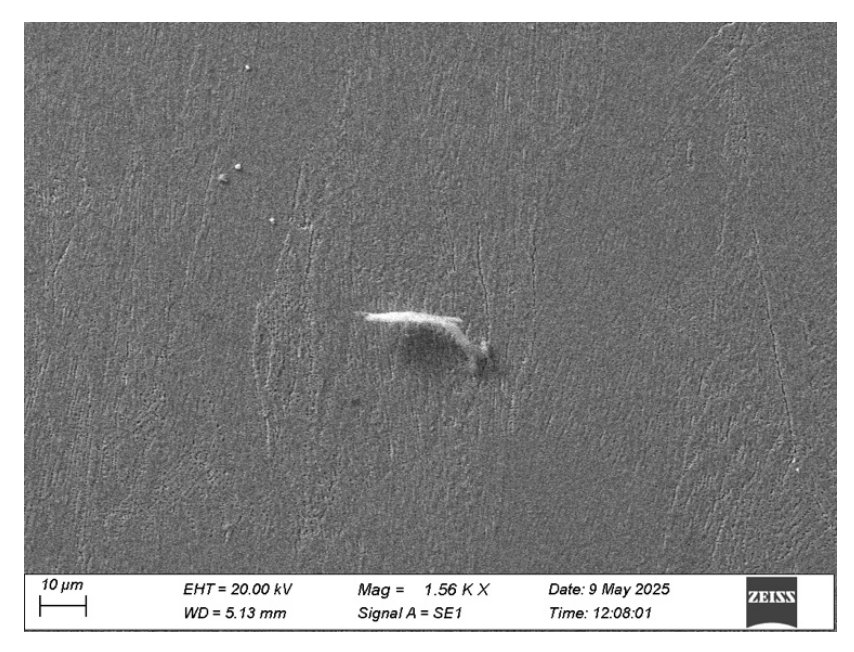


Figure 25: SEM image of sample 29 along the XZ-plane

Similarly for sample 29, EBSD analysis was carried out to try and observe a grain orientation, boundary topology and intergranular lattice distortion (Figure 26). The first map (BC+IPF+GB+GROD-ANG) showcases a heterogenoues microstructure, of different size and shape including elongated and equiaxed morphologies. The GROD-angle values do not have an uniform distribution but produce band-like zones of grains, evidencing the extension of sub grain structures of the solidification processing. The Kam distribution suggests numerous region of high local misorientation throughout the interiors of larger grains and across the grain boundaries in the second map (BC+IPF+GB+KAM). Compared with sample 28, sample 29 still has a significant percentage of misoriented regions. The ultimate map (BC+IPF+GB) confirms the concomitant elongated and equiaxed grains. The network of boundaries is made of high-angle boundaries for the most part, and low-angle boundaries presnt as sub-divisions within larcer grains.



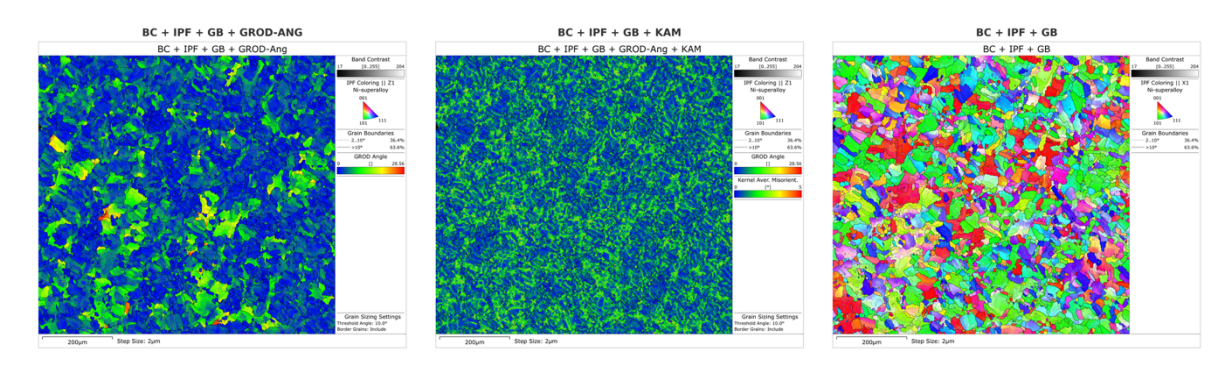


Figure 26: EBSD maps of sample 29

In continuity with the analyses performed on samples 28 and 29, the optical microscopy observations of sample 30 are presented below, both on the XY-plane and on the XZ-plane (Figure 27).

On the XY-plane the microstructure of sample 30 exhibits a network of melt track patterns that are visible and more irregular compared to the previous specimens. The overlapping of the laser passes is evident, but the tracks show variations in width and curvature. This irregularity suggests a higher sensitivity of this sample to local fluctuations in heat input and solidification. On the XZ-plane, melt pools are distinghuishable along the build direction. Compared to sample 28 and 29, the melt pools appear broader and less uniform in curvarture, suggesting differences in thermal history during layer deposition. Despite these variations the columnar structure remanis dominant, extending vertically across multiple layers.

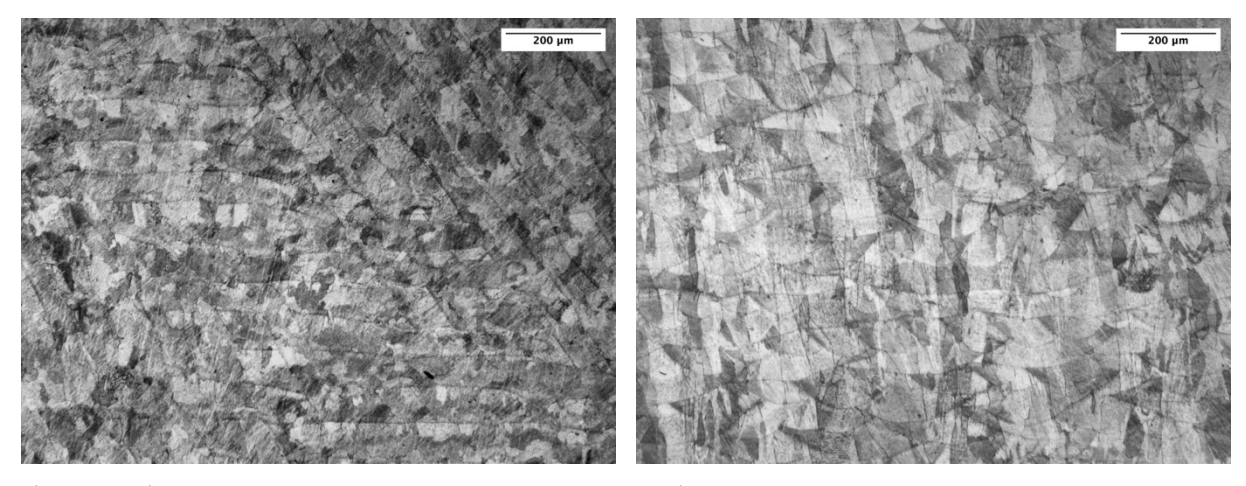


Figure 27: microstructure of sample 30 along the XY-plane (a); microstructure of sample 30 along the XZ-plane (b)

The SEM observation of sample 30 highlight a microstructure characterized by the coexistence of columnar grains at hte macroscopic scale and a cellular substructure at the microscopic level (Figure 28 a-b). At higher magnification a feature of this sample is the presence of ninely dispersed Hf oxides precipitates which decorate the cellular boundaries and the melt pool interfaces. In sample 30 this features appear more accentuated compared to the previous specimens, suggesting differences in solidification dynamics.

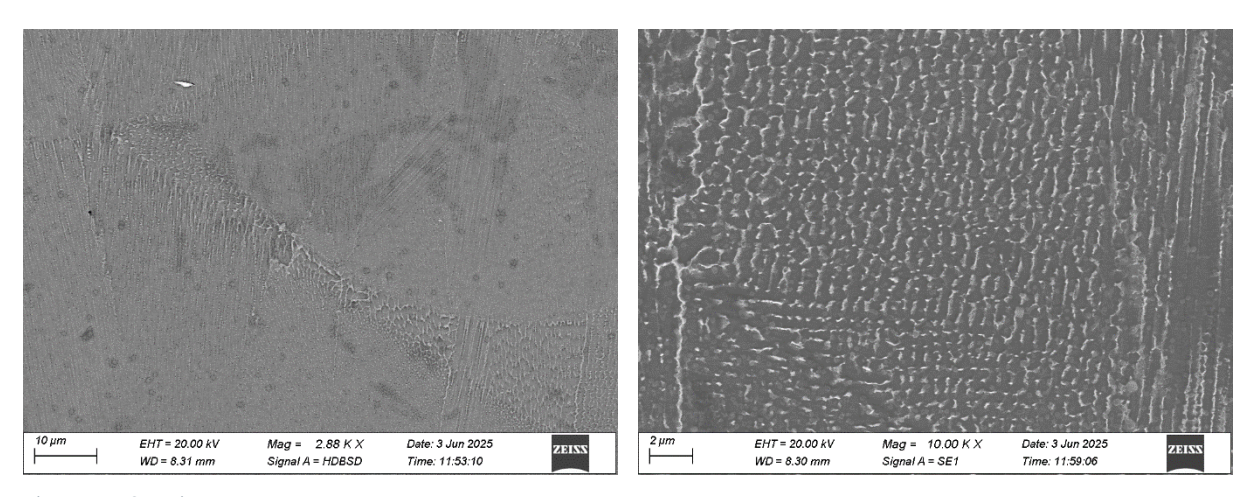


Figure 28: SEM images of sample 30 along the XZ-plane (a)-(b)

The EBSD maps of sample 30 (Figure 29) have a microstructure of irregular morphlogies of grains and high intragranular misorientation. The map 1 presents grain of mixed morohology with elongation and equiaxed shapes. The GROD-ANG distribution contains high internal misorientation of several grains. The magnitude of such distortions suggests a high amount of residual strain preserved in the as-built state. The Kam map confirms universal intragranular misorientation, and high Kam regions accumulate near boundaries and within large grains. The persistence of these attributes suggests that the microstructure has not released its stress and still contains a significant degree of heterogeneity. Map three describes sample 30's morphology as irregular and its size distribution to be large, ranging from very fine equiaxed grains up to elongated zones extending over numerous tens of microns. The network of the grain boundaries is of high-density nature and high-angle boundaries define the greater portion of the interfaces. Compared to sample 28 and 29, sample 30's morphology appears to be of a discontinuous nature.

### Sample 30

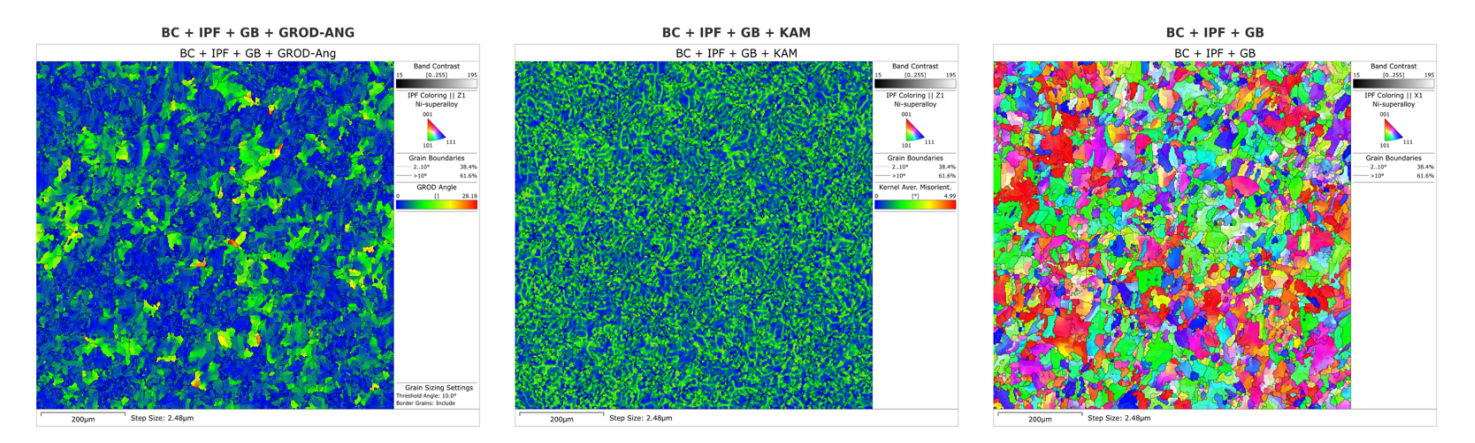


Figure 29: EBSD maps of sample 30

### 4.1.3 Cubic Samples-Melt pool

After completing the analysis of porosity and grain morphology in the microstructure, the investigation was extended to the chacarterization of the melt pools. Optical microscopy was employed to acquire images of the samples, which were subsequently processed using ImageJ. For each cubic specimen, the width and depth of ten melt pools were measured, and the profile of each melt pool was reconstructed by selecting ten equidisatn points along its corss-section. These profiles were then fitted with a second-order polynomial function of the form  $y = ax^2 +$ x + c. The obtained interpolations (Errore. L'origine riferimento non è stata trovata., Errore. L'origine riferimento non è stata trovata. and Errore. L'origine riferimento non è stata trovata.) demonstrated a high degree of accuracy, as indicated by correlation coefficients  $R^2$  very close to 1, confirming the suitability of the chosen polynomial model for describing the melt pool geometry. In addition, the polynomial fitting allowed for the extraction of the quadratic coefficient "a", which is directly related to the curvature of the melt pool profile. A higher absolte value of a corresponds to a steeper curvature, whereas lower value indicate a flatter, more open profile. Based on the experimental data, sample 29 displayed the highest mean value of "a", which implies a more open upward curvature and consequently a flatter melt pool cross-section.

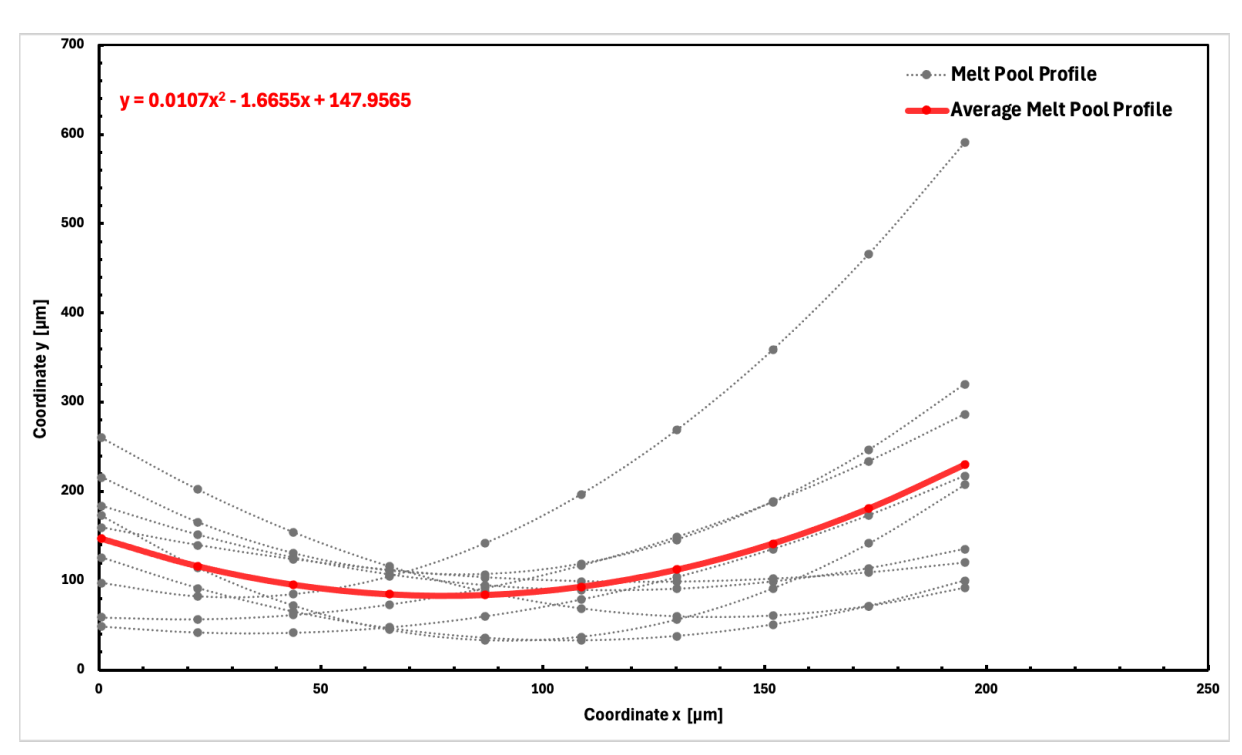


Figure 34: comparison between the individual melt pool profiles (grey) and the average profile (red) of sample 28, fitted with a second order polynomial.

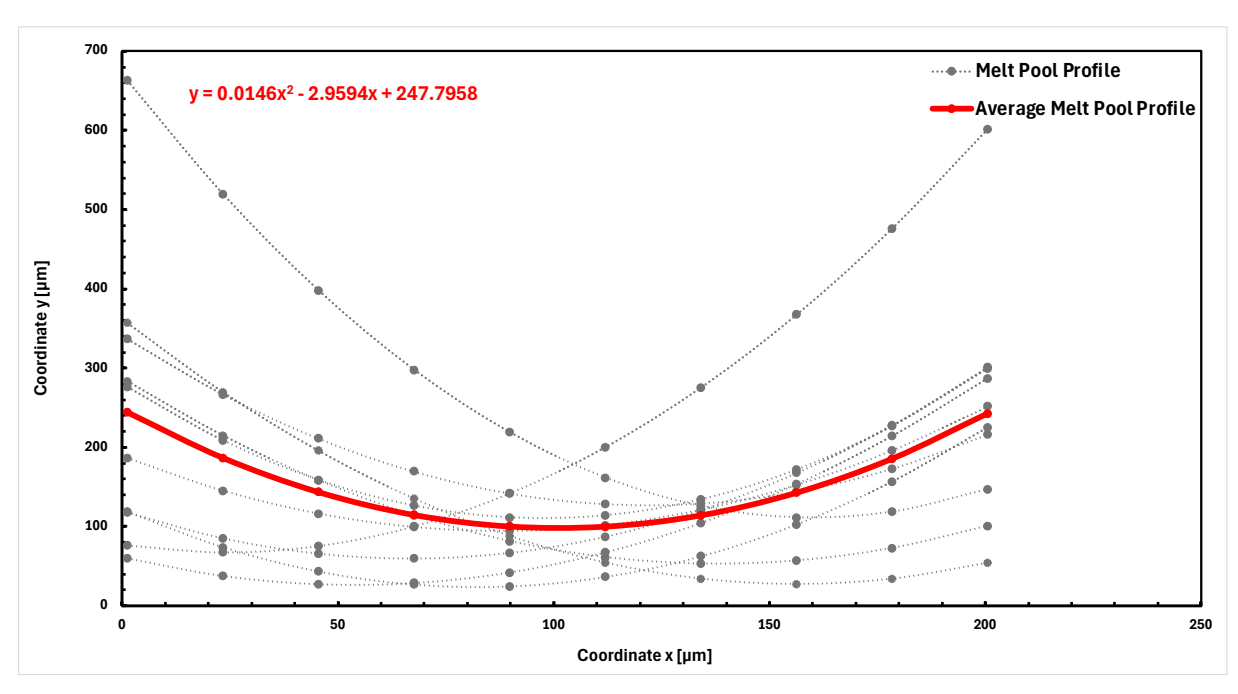


Figure 35: comparison between the individual melt pool profiles (grey) and the average profile (red) of sample 29, fitted with a second order polynomial

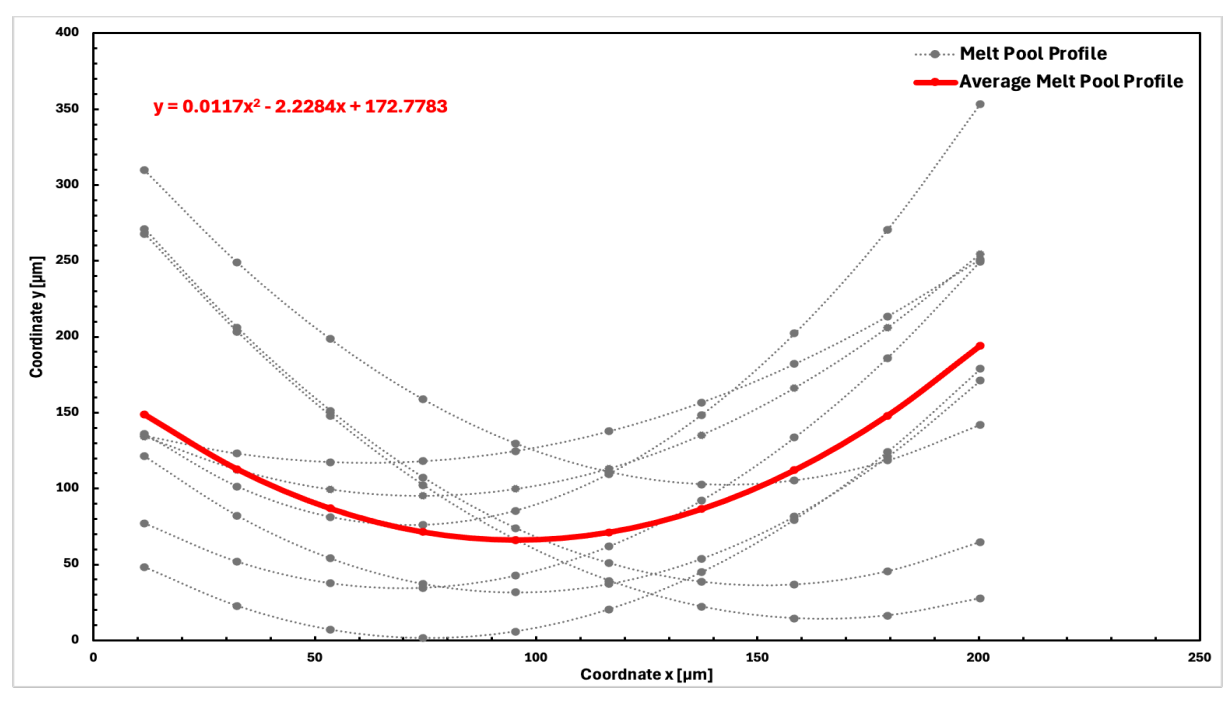


Figure 36: comparison between the individual melt pool profiles (grey) and the average profile (red) of sample 30, fitted with a second order polynomial

The boxplot in Figure 30 illustrates the distribution of melt pool width measured across the three investigated samples and it highlights clear differences in melt pool morphology between the tested conditions. Sample 29 appears to be the most stable, while Sample 30, despite producing larger widths, reveals direduced uniformity. Sample 28 falls in between, characterized by a greater dispersion.

The boxplot in Figure 31 presents the distribution of melt pool depth. Sample 28 exhibits the shalowest melt pools, while Sample 29 shows deeper melt pools than Sample 28. Sample 30 records the greates mean depth among the three but also the largest dispersion of valure. Overall, this analysis revela a clear trend of incresing melt pool depth from Sample 28 to Sample 30, accompained by an increase in variability.

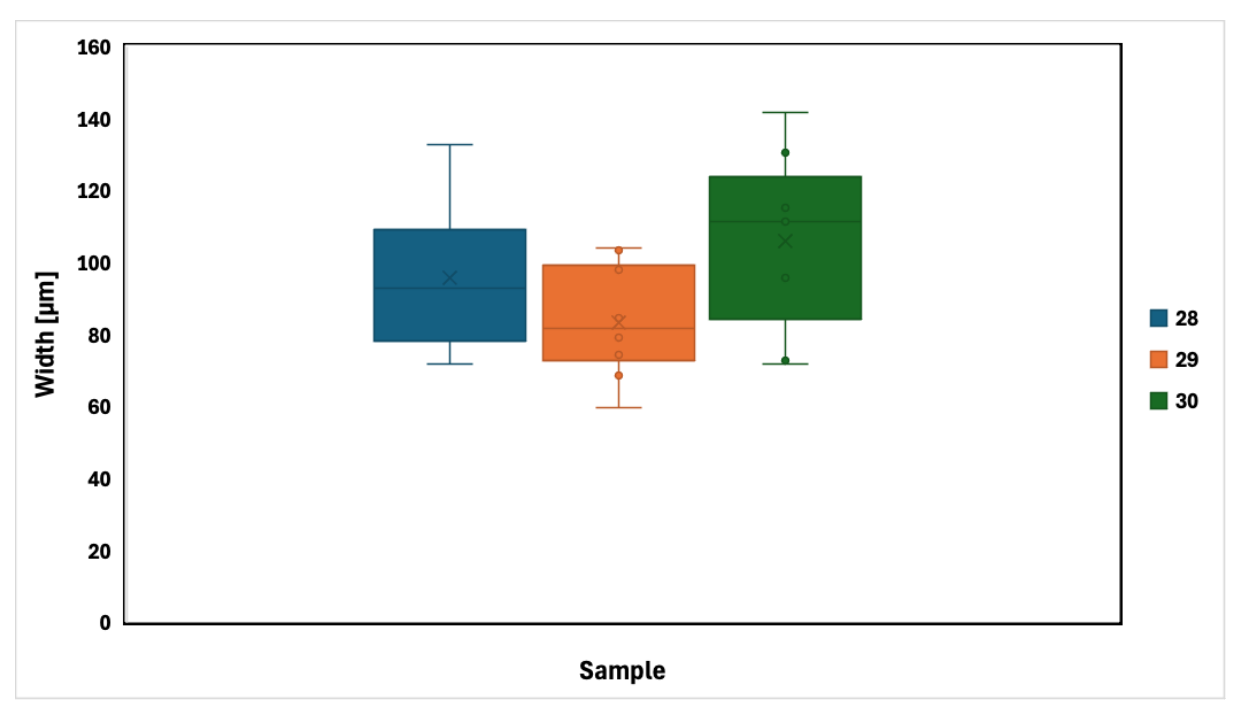


Figure 30: distribution of melt pool width measured across the three samples

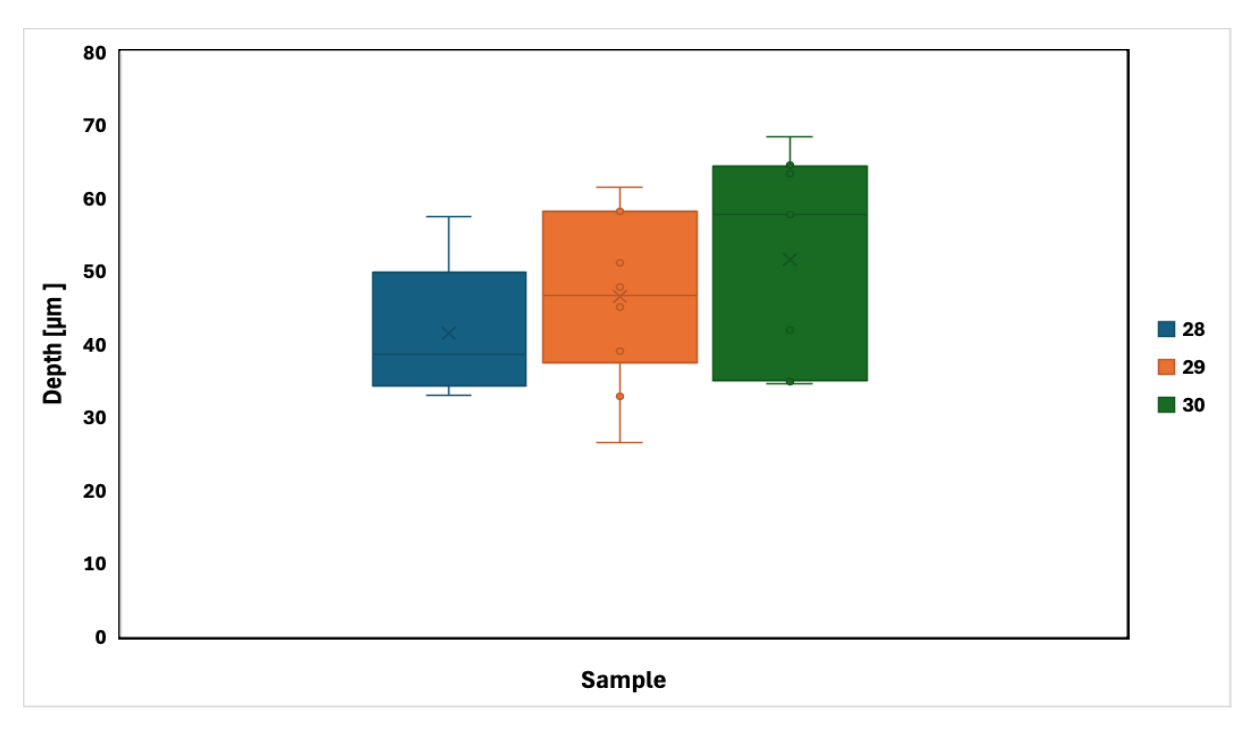


Figure 31: distribution of melt pool depth measured across the three samples

Errore. L'origine riferimento non è stata trovata. shows the width-to-depth ratio calcutaed for three samples, with error bars indicating the standard deviation. Sample 28 exhibits the highest ratio, associated with a shallower and wider morphology. Sample 29 shows the lowest ratio, reflecting a deeper and narrower profile. Sample 30 lies in between buti s characterized by higher variability, as highlighted by the wider error bars. Overall, the width-to-depth ratio complements the separate analysis of width and depth, allowing for a more comprehensive interpretation of the melt pool morphology.

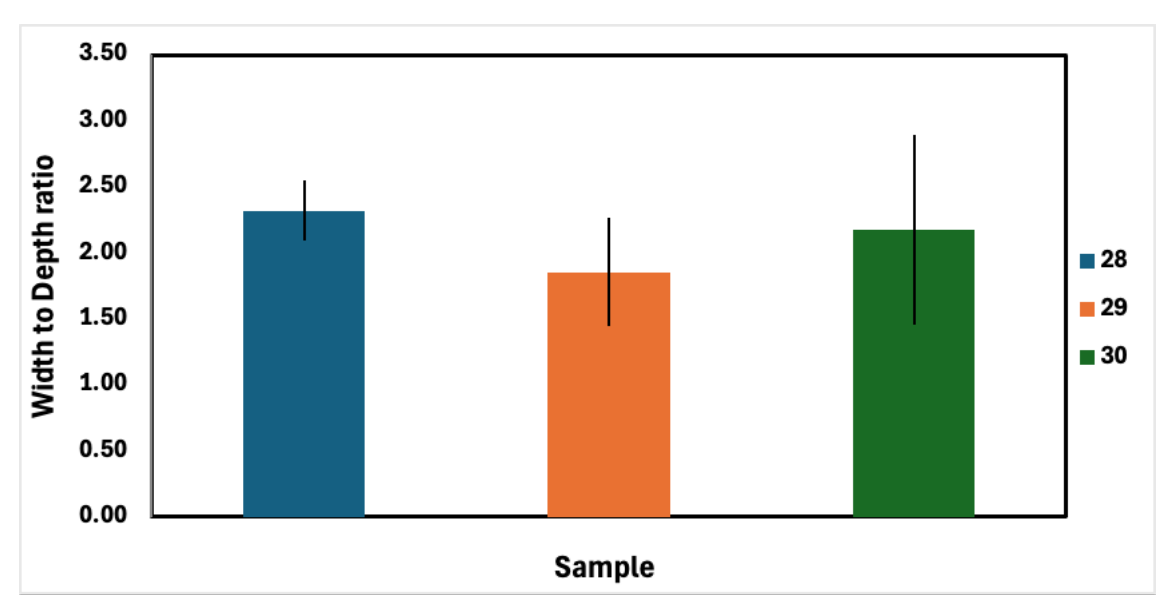


Figure 39: width to depth ratio calculated for three samples

### 4.1.4 Coal Cart Samples-Porosity

Similiarly to what was carried out for the cubic samples, a detailed porosity analysis wa salso performed on the complex-shaped samples, known as coal carts. In this case, three different specimens were examined, each of wich had undergone a distinct post-processing route. More specifically, sample 39 was investigated in the as-printed condition, sample 37 was subjected to Hot Isostatic Pressing (HIP), while sample 32 represented the fully treated condition, having been processed through the combined sequence of HIP, solution treatment, and subsequent aging.

The corresponding Volumetric Energy Density (VED) values employed during the fabrication of the three specimens are reported Table 5.

Table 5:Values of Volumetric Energy Density (VED) applied to Coal Cart samples

Sample	Type	Heat treat	VED
ID#			$J/mm^3$
39	Coal Cart	As-built	80.4
37	Coal Cart	HIP	80.4
32	Coal Cart	HIP+SolHT+Age	45.2

Due to the complex geometry of the coal cart samples, which is characterized by the simultaneous presence of both thin and thick wall sections, the analysis was primarily focused on evaluating how porosity distribution varied within these two distinct regions. This approach

allowed for a more comprehensive evaluation of the influence of geometrical features and thermal history on defect deformation and microstructural integrity.

The analysis of porosity begins with sample 39 (Figure 40). In the XY plane, a clear difference can be observed between the thick and the thin wall regions. The thick wall shows a lower porosity, with pres that appear more isolated. Conversely, the thin wall exhibits a higher porosity level, with pores that are more frequent and tendo to cluster, indicating a less compact microstructure. In the XZ plane, the same trend can be observed. The thick wall mantains a relatively homogeneous structure with limited porosity, whereas the thin wall reveals a higher concentration of pores. When comparing the XY and XZ planes, no substantial deviations are detected in terms of porosity distribution. This suggest that the porosity characteristics are not strongly dependent on the observation plane but rather on the wall thickness.

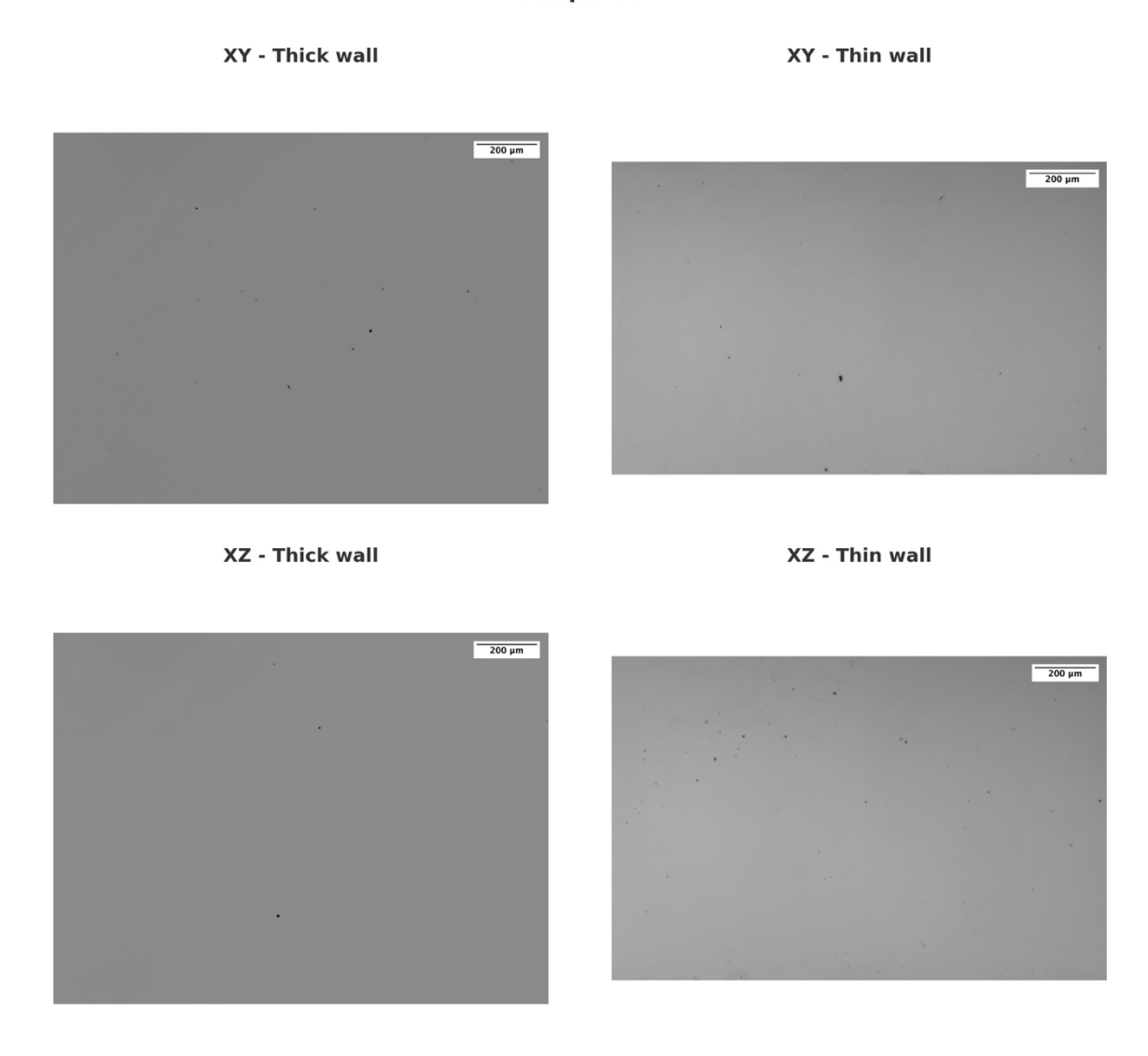


Figure 32: porosity analysis of sample 39 in thick and thin walls observed along XY and XZ planes

As observed for sample 39, porosity is more pronounced in the thin wall compared to the thick wall. The same trend is confirmed for samples 32 and 37 (Figure 33and Figure 34). For clarity and conciseness, only the images of the thick and thin walls across the XZ plane are reported for these two samples, since the observation plane does not represent a discriminating factor.



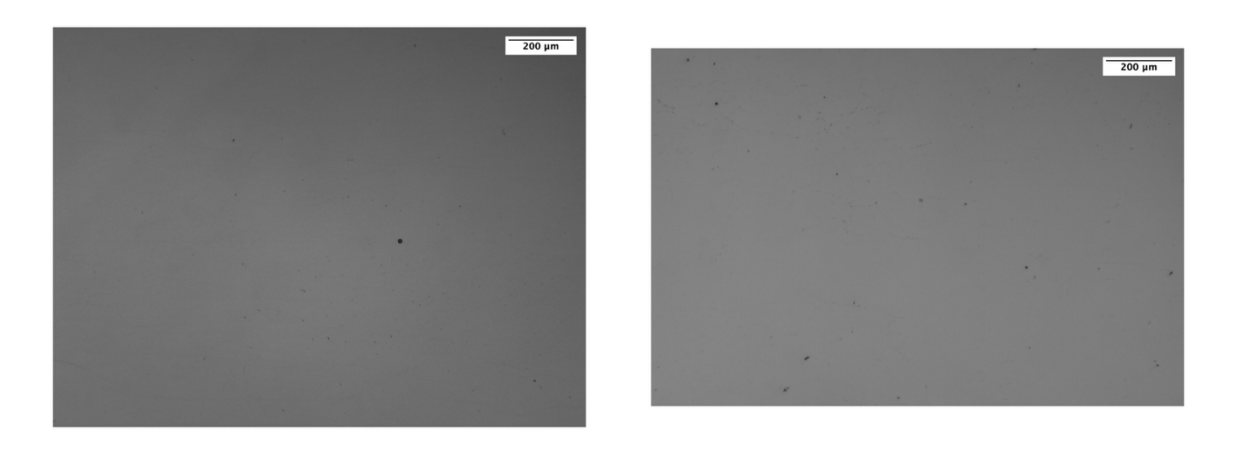


Figure 33: porosity analysis of sample 37 in thick and thin walls observed along XZ plane.

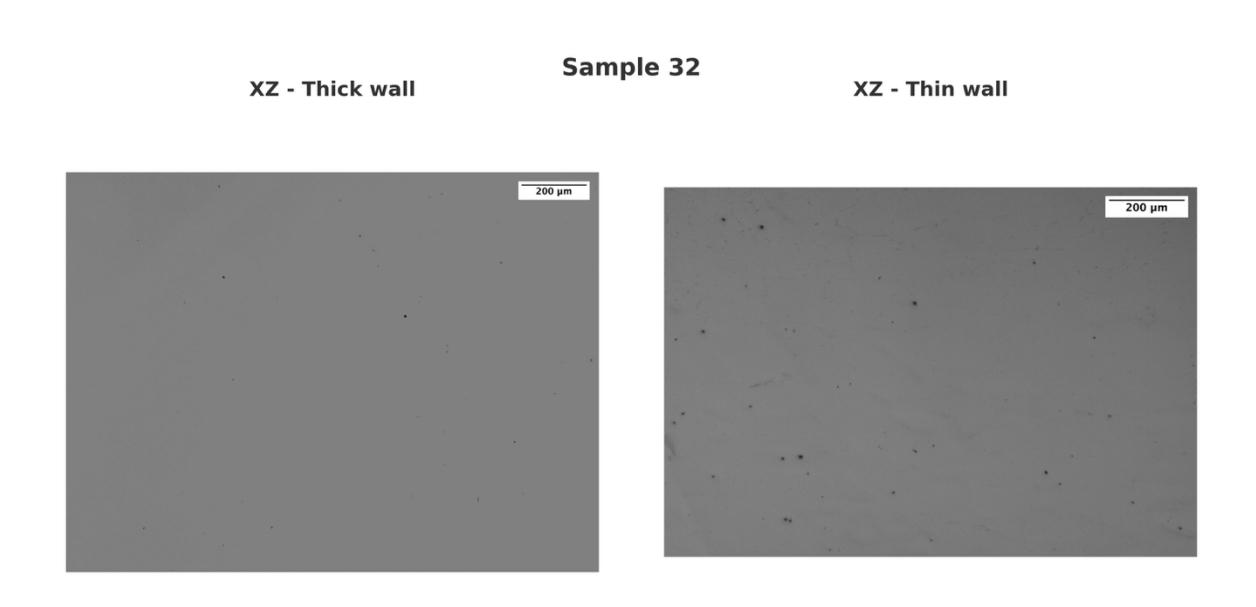


Figure 34: porosity analysis of sample 32 in thick and thin walls observed along XZ plane.

Based on the optical microscopy images, it was possible to investigate not only the distribution of pore diameters but also their aspect rario. The aspect ratio distribution of pores in the coal cart samples was analyzed on both XY and XZ planes, and results are presented in Figure 35. For sample 39 (as built), the mean aspect ratio is higher in the XY plane compared to the XZ plane, with values around 2.0 and 1.9, respectively. The associated standard deviation are moderate, indicating a variability in pore morphology.

For sample 37 (HIP), the mean aspect ratios are close to those of sample 39, with values just above 2.0 in the XY plane and slightly below 1.9 in the XZ plane. The standard deviations are lower than in sample 39, suggesting a more homogeneous pore distribution after HIP process. For sample 32 (HIP+solHT+Age), the mean aspect ratio in the XY plane is the lowest among the three samples, reaching 1.4, while in the XZ plane it is close to 1.7. The standard deviation follows the same trend, with a low value 0.3 in XY plane and reaching 0.75 in XZ plane.

A clear reduction of the porosity aspect ratio is observed when moving from sample 39 (as built) to sample 32 (HIP+SolHT+Age). This result can be attributed to the progressive effect of the thermal treatments. As a result, pores become more equiaxed and homogeneous, especially in the XY plane.

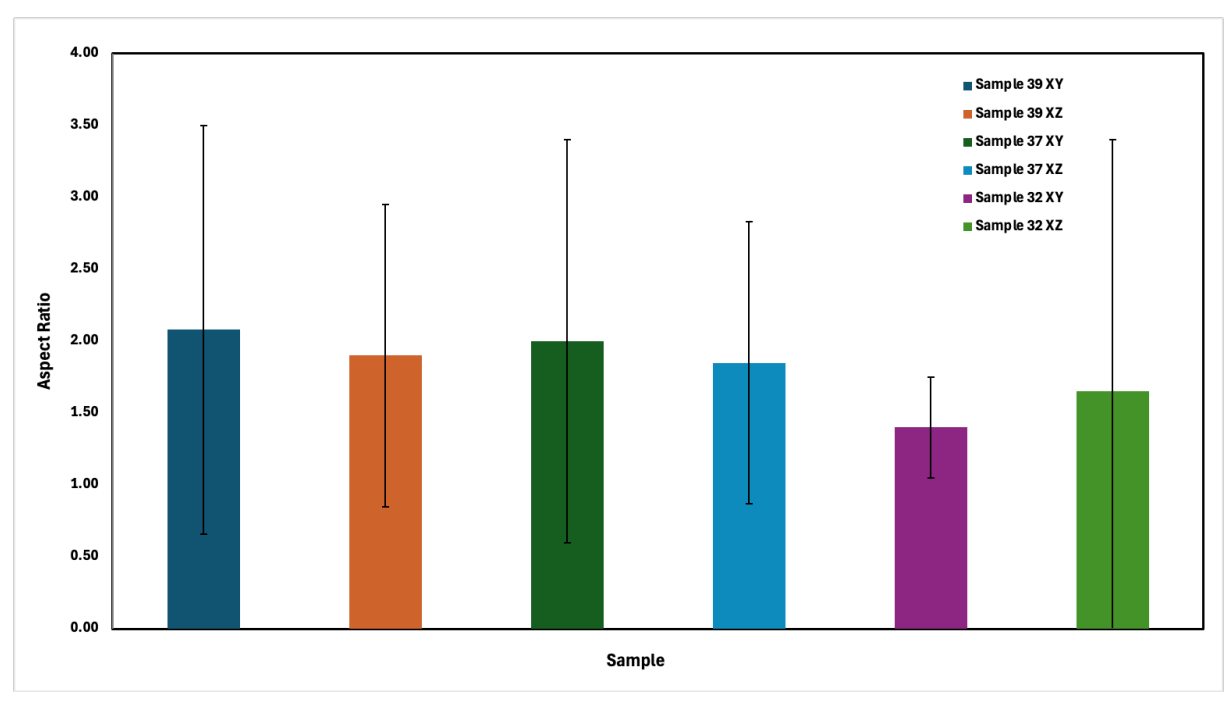


Figure 35: Mean aspect ratio and standard deviation of pores in samples 39, 37, and 32 measured along XY and XZ planes.

Following the analysis of the pore aspect ratio, further attention was dedicated to the distribution of pore diameters, as derived from optical microscopy images. Figure 36 and Figure 37 present the lognormal distributions obtained for the XY and XZ planes, respectively.

In the XY plane, all three specimens exhibit a peak in the pore size distribution within the lower diameter range, although with distinct difference depending on the processing condition. The as-printed sample 39 shows the broadest distribution, extending towards significantly larger diameters, with a main peak around 3-4  $\mu$ m but also a long tail reaching values above 15  $\mu$ m. On the other hand, the HIP-treated specimen (sample 37) displays a narrower distribution, with most pores between 2.5 and 6  $\mu$ m and a clear reduction of large size defects. In this case, the distribution differs from that of sample 39, as it does not exhibit a log-normal shape. This behavior arises from the fact that the anlysis is sensitive to the defect size. Since the overall defect count is very low, even a small scatter in the values becomes immediately apparent in the results.

The fully treated specimen (sample 32) exhibits the most refined distribution, with a peak at 3.5 µm and very few pores exceeding 8 µm.

A similar trend can be observed on the XZ plane, although with some dfferences. The as-printed sample (sample 39) present the widest distribution, characterized by a peak around 4-5  $\mu$ m and a large fraction of pores with diameter exceeding 10  $\mu$ m. The HIP-treated condition (sample 37) shows a more confined distribution, with a peak around 4  $\mu$ m and a marked reduction in large defects. Finally, the fully treated condition (sample 32) displays the narrowest and most localized distribution, with the majority of pores concentrated in the range of 3-4  $\mu$ m.

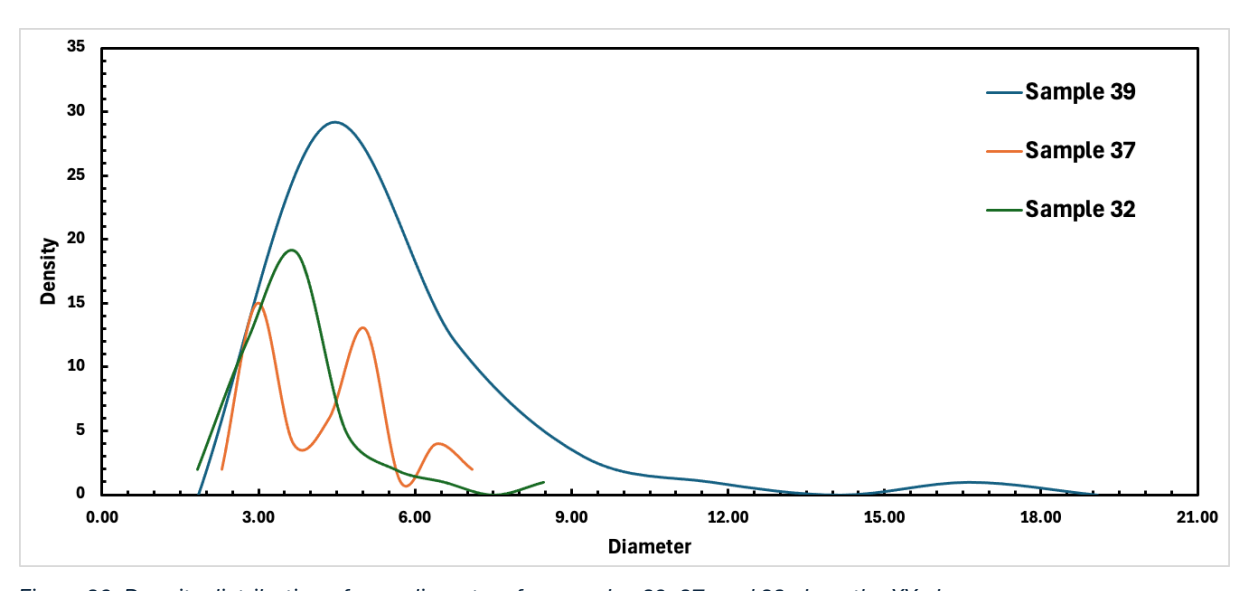


Figure 36: Density distribution of pore diameters for samples 39, 37, and 32 along the XY plane.

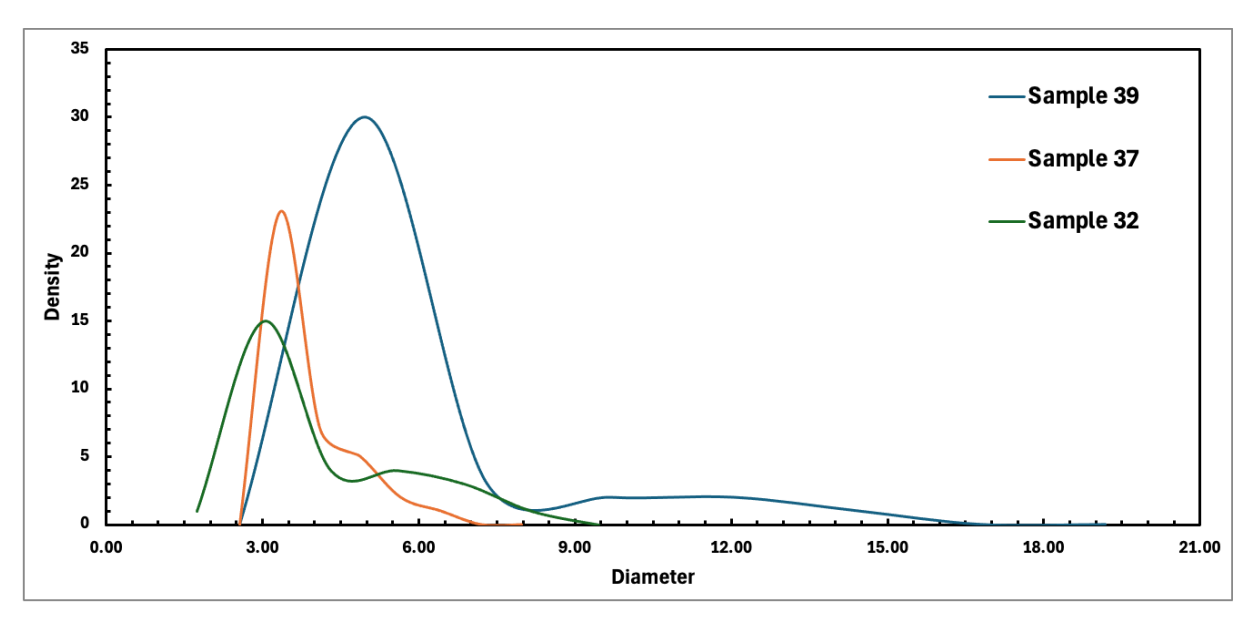


Figure 37: Density distribution of pore diameters for samples 39, 37, and 32 along the XZ plane.

The comparison between the XY and XZ planes highlights that defects tend to be more elongated aloong the building direction (XZ plane), which is consistent with the layer-by-layer nature of the additive manufacturing process. Post-processing traetments, and in particular HIP combine with solution and aging, are effective in reducing both size and the variability of defects, leading to a more homogeneous defect morphology across different orientations.

### 4.1.5 Coal Cart Samples-Microstructure

Following the same approach adopted for the cubic samples, a micorstructural analysis of the grain morphology wa salso performed on the coal cart samples. In this case, particular attention was paid to the fact that the three specimens under investigation had undergone different post-processing routes, which provide the possibility to evaluate how the grain structure evolved as a consequence of the applied treatments. Since sample 39 is in the as-built condition, its grain morpholofy is expected to be comparable to that of the cubic samples, which where also analyzed in the as-built state. For this reason, no further comparison is required for sample 39. The grain structure analysis is therefore focused on sample 37 (HIP) and 32 (HIP+SolHT+Age), in order to identify the microstructural modifications induced by the different post processing treatments.

The optical micrographs of sample 37 (Figure 38) taken along the XY and XZ planes show differences in grain morphology and orientation. In the XY plane, the microstructure is characterised by equiaxed grains with uniform size distribution. In the XZ plane, the grains exhibit a more elongated morphology, with a preferential orientation along the build direction.

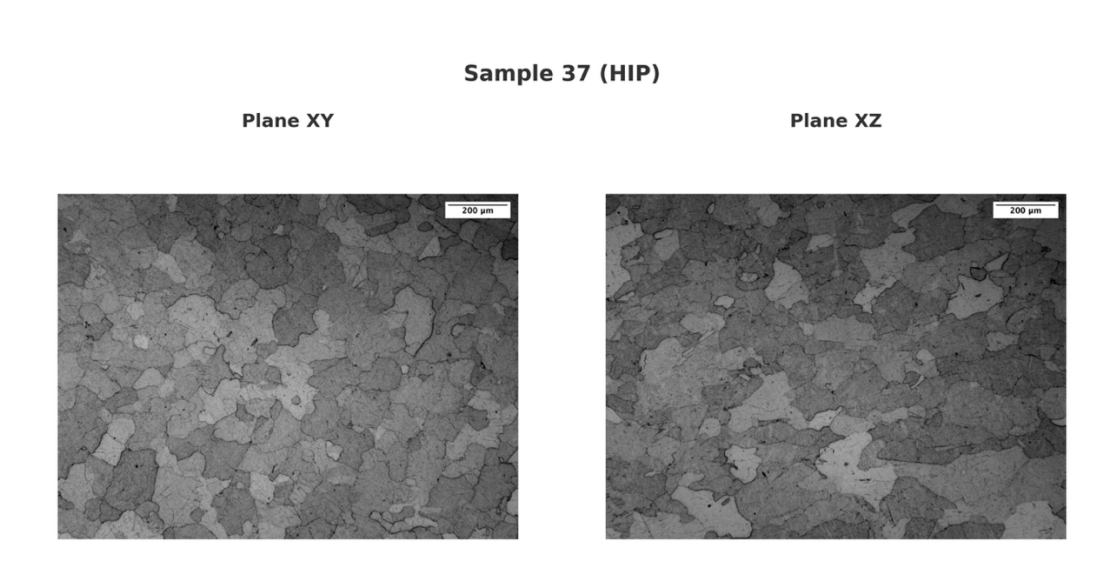
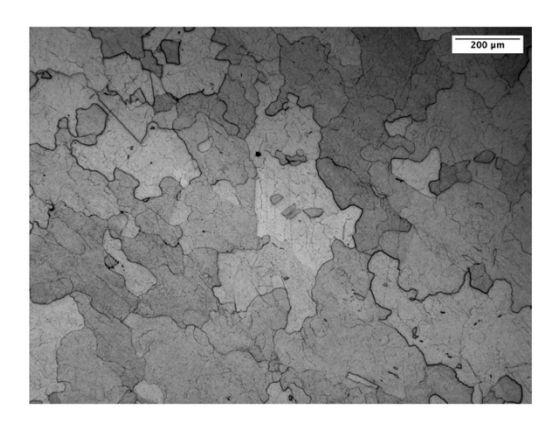


Figure 38: Optical micrographs of the grain structure of sample 37 (HIP) observed along the XY and XZ planes.

Compared to the HIP condition, the microstructure of sample 32 shows some modifications in grain morphology and orientation when observed along the XY and XZ plane (Figure 39). In the XY plane, the grains appear more equiaxed and finer with a uniform distibution across the section. In the XZ plane, the grains still show a certain elongation along the build direction although this tendency is less evident than in the HIP only condition.

Plane XY Plane XZ



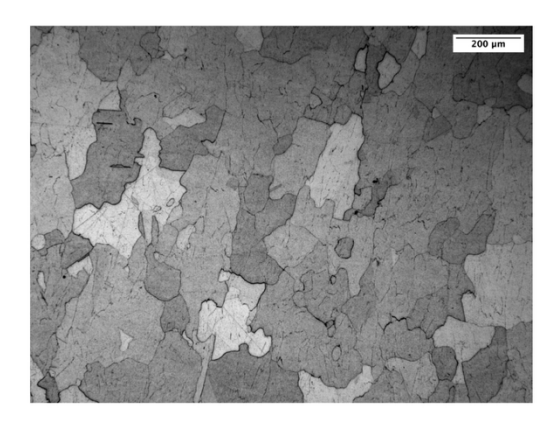


Figure 39: Optical micrographs of the grain structure of sample 32 (HIP+SolHT+Age) observed along the XY and XZ planes.

The grain size was determinated in accordance with the ASTM E112-13 (2021) standard, by employing the intercept method, which allows a quantitative and statistically analysis of grain dimension across different regions of the material. The data obtained from this analysis were subsequently used to calculate the aspect ratio of the grains, in order to evaluate their average size and to identify possible anisotropies induced by the different processing conditions. The comparison of mean aspect ratio values shows that the results for the two samples are very similar: 1.43±0.27 for sample 37 (HIP) and 1.36±0.26 for sample 32 (HIP+SolHT+Age). This small variation is negligible and indicates that the additional heat treatment has no significant influence on the aspect ratio of porosities. The principla effect of HIP is to close elongated defects, transforming them into spherical pores and driving the aspect ratio towards unity. The gently reduction of the mena value in sample 32 can be attributed to the occurence of theral induced porosity, which leads to the formation of spherical pores.

The SEM observation of sample 39 in the as-built condition (Figure 40) shows that in the thin wall region (XZ plane), the metl pool morphology is clearly visible. The rapid cooling rate leads to elemental segregation at the cell boundaries. Since the material has not undergone any post-processing treatment, the segregated phases, which are mainly Hf-rich oxides, are not allowed to re-dissolve into the matrix. A higher magnification is possible to observe the distribution of

these precipiates along the melt pool boundaries. In the thick wall (central region), the microstructure exhibits both cellular and columnar grains. The cellular substructure is still present inside the columnar grains, confirming the high cooling rates. Pricipitates are visible, mostly located at the cell boundaries.

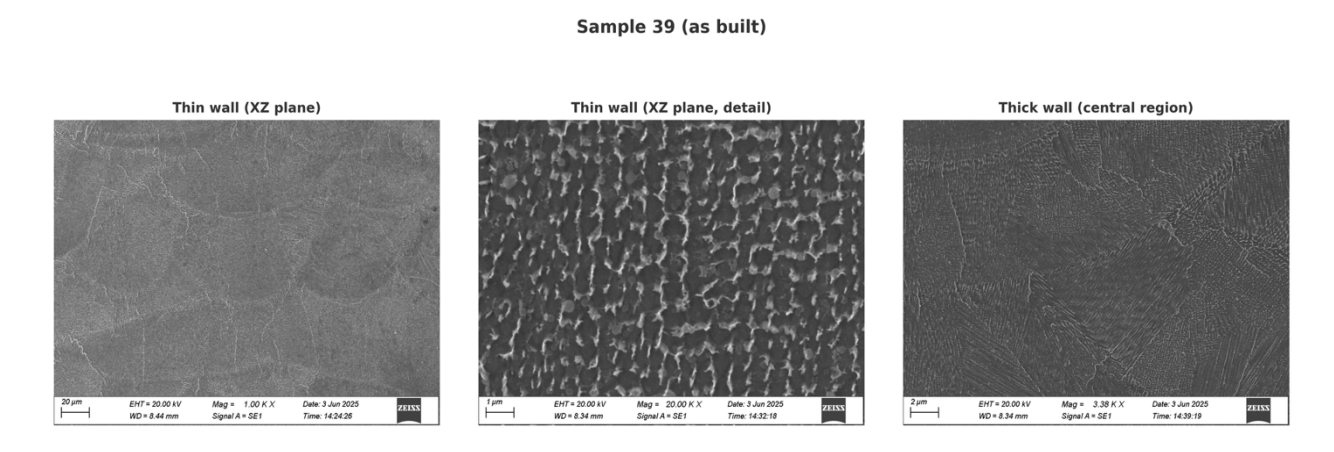


Figure 40: SEM micrographs of sample 39 (as built): thin wall observed on the XZ plane, detail of the thin wall, and thick wall in the central region.

The SEM observations of sample 37 (HIP), Figure 41, reveals distinct microstructural features between the thin wall region and the central thick wall region.

In the thin wall, the  $\gamma'$  phase does not exhibit the typical cubic morphology but instead develops into a "fan-like" arrangement, which is consistent with the lower cooling rates associated with the HIP condition. At the external boundaries of the thin wall, Hf-rich oxide precipitates are detected, indicating solute segregation during processing. A higher-magnification image further highlights the morphology of the  $\gamma'$  precipitates in this region.

In the central thick wall, the  $\gamma'$  precipitates are noticeably larger compared to those observed in the thin wall. This coarsening effect is attributed to the further reduction in cooling rates within the thicker section, where the thermal gradient is less pronounced.

#### Sample 37 (HIP)

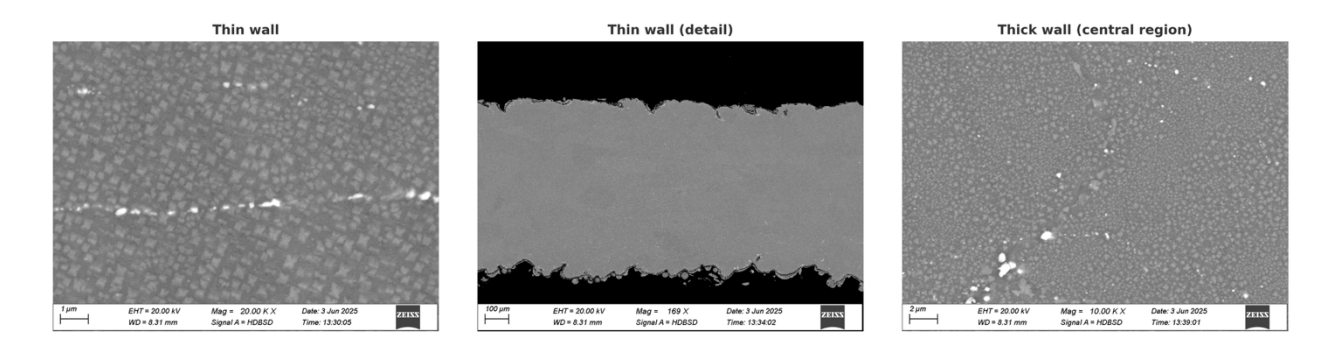


Figure 41: SEM micrographs of sample 37 (HIP): thin wall observed on the XZ plane, detail of the thin wall, and thick wall in the central region.

The application of combined HIP, solution heat treatment, and ageing to the sample 32 produces a microstructure that is differen from the HIP-only condition, both in terms of precipitate morphology and secondary phase distribution (Figure 42). In the thin wall region,  $\gamma'$  precipitates are visible along the grain boundaries and within the matrix. Their morphology is cuboidal as result of the successive thermal treatments. In addition to  $\gamma'$ , the presence of Hf oxides and Ta carbides is detected, located at the grain boundaries. In the central thick wall, the  $\gamma'$  precipitates mantain theri cuboidal morphology but appear finer and more dispersed than in the thin wall. The Hf oxides and Ta carbides are still present.

# Sample 32 (HIP + SoIHT + Age)

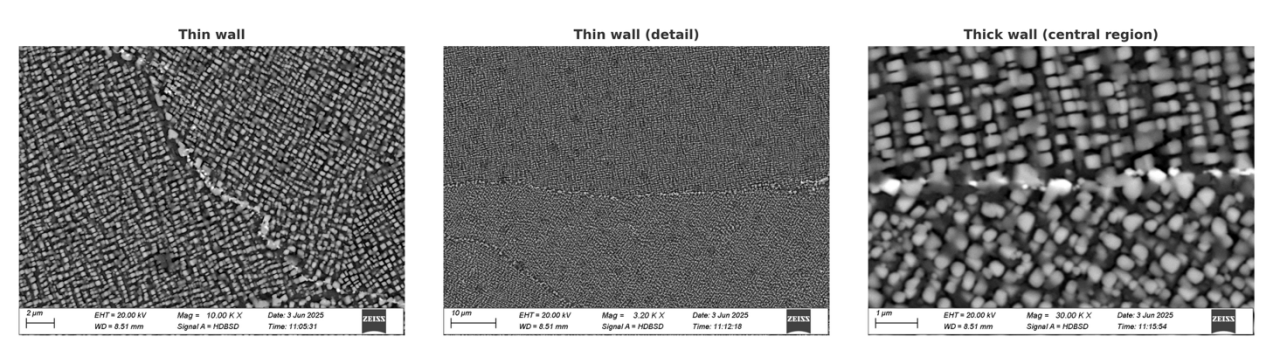


Figure 42: SEM micrographs of sample 32 (HIP+SolHT+Age): thin wall observed on the XZ plane, detail of the thin wall, and thick wall in the central region.

### 4.1.5 Coal Cart Samples-Melt pool

For the analysis of melt pools in the coal cart geometry, sample 39 in the as-built condition was employed. The melt pool profiles were reconstructed folloqing the same procedure used for the cubic samples: ten equidistant points were selected along the cross-section of each melt pool, and the corresponding profile was fitted using a second-order polynomial function of the form  $y = ax^2 + x + c$ . The purpose og this study was to investigate wheter a trasition from the thick wall to the thin wall region produces any significant variation in melt pool morphology, with particular attention to marked changes in the average value of the coefficient "a".

The melt pool profiles corresponding to the thick wall and thin wall regons are reported in **Errore. L'origine riferimento non è stata trovata.** and **Errore. L'origine riferimento non è stata trovata.** For the thick wall, the average profile shows a quadratic coefficient of a = 0.009 while for the thin wall, the corresponding value is slightly higher a = 0.013. This indicates that the curvature of the melt pools becomes more pronounced in the thin wall region. Howere the difference between the two values is negligible, suggesting that the morphology of the melt pools is not substantially affected by the transition from the thick to thin sections.

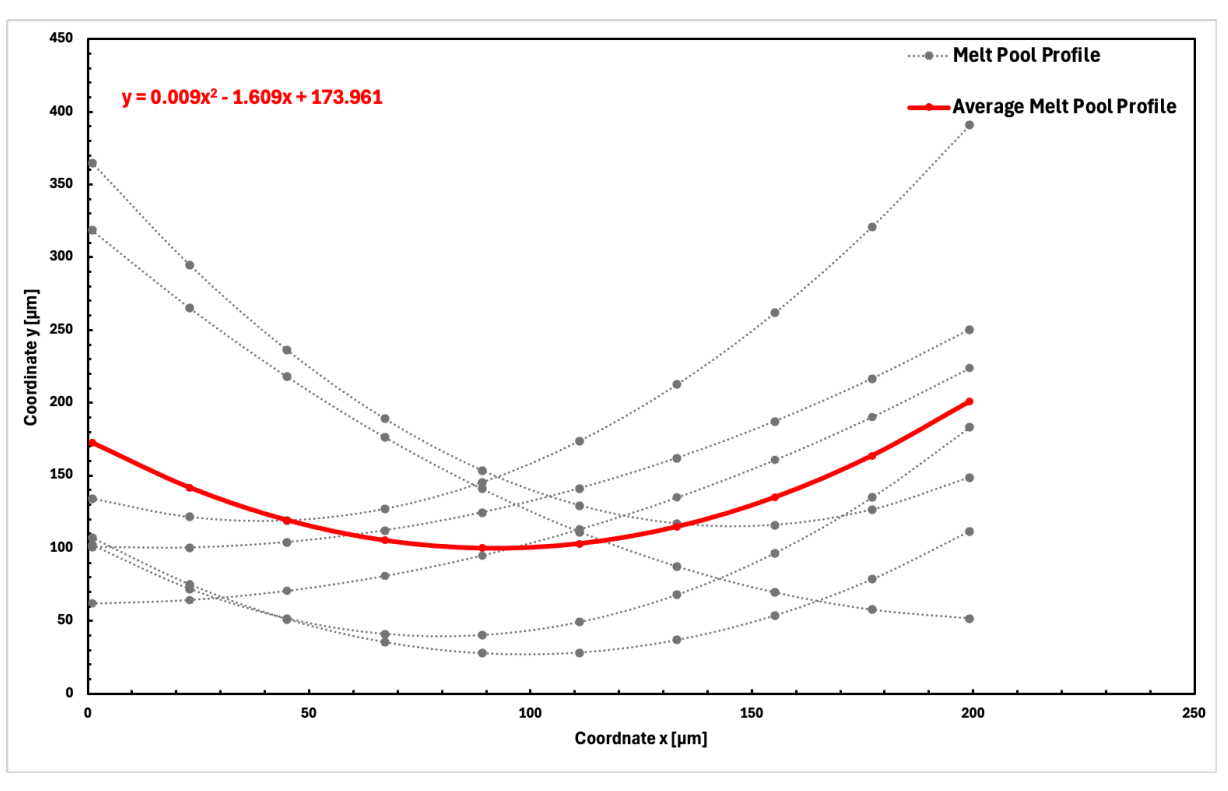


Figure 51: comparison between the individual melt pool profiles (grey) and the average profile (red) of sample 39, fitted with a second order polynomial

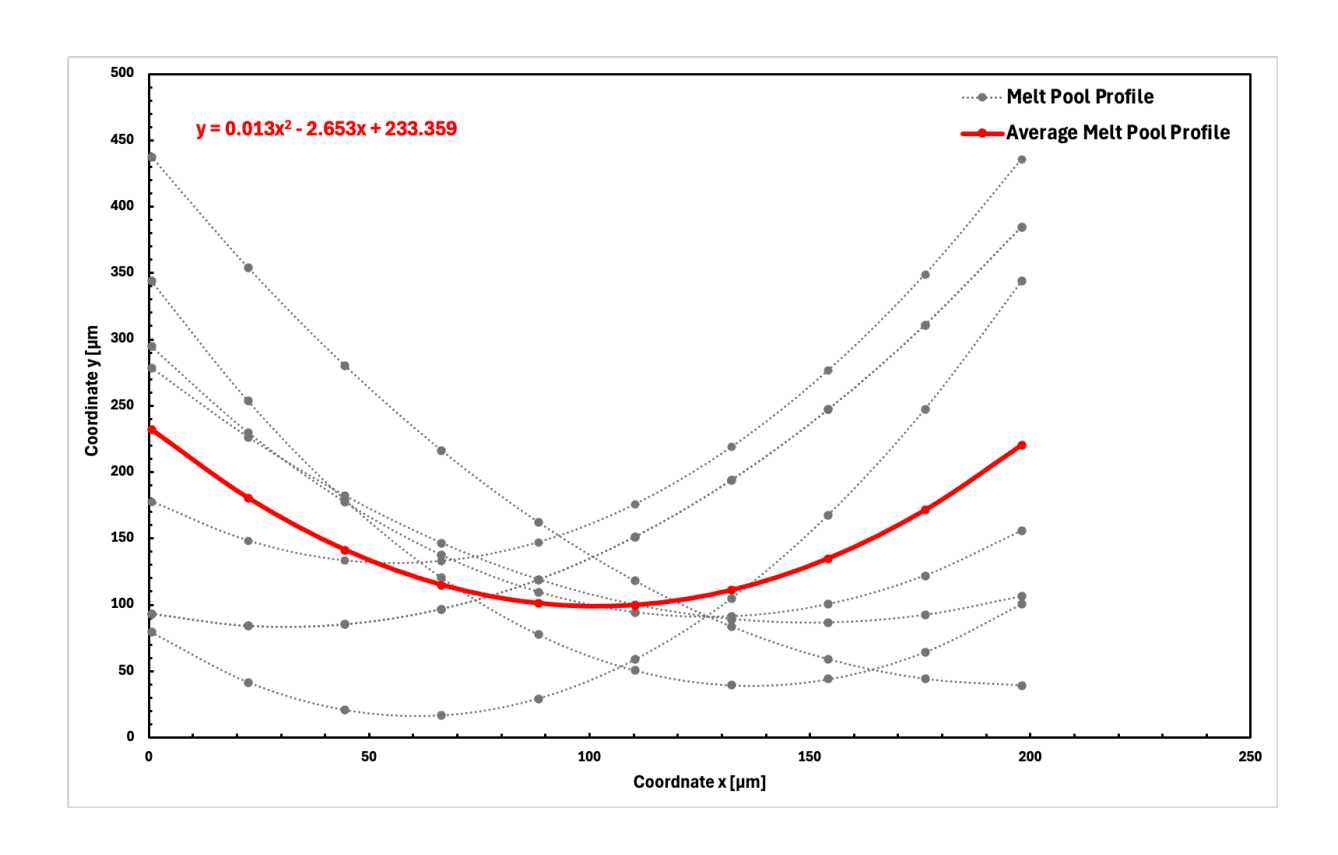


Figure 52: comparison between the individual melt pool profiles (grey) and the average profile (red) of sample 39, fitted with a second order polynomial

## 4.2 Quantitative analysis of microstructure

Though the phenomenological description of the microstructure provides a valuable understanding of the morphology of grains, distribution of boundaries and defect properties, such description will always be intrinsically qualitative. To move beyond descriptive observation, a quantitative assessment was undertaken such that the goal was to obtain quantifiable correlation between processing condition and microstructural property. This approah is essential since additive manufacturing processes are governed by complex thermal and solidification processes such that process parameters influence grain structure, defect nucleation and crystallographic orientation. By quantifying major microstructural parameters and connecting them to the major processing parameters, it is then possible to create models capable of capturing such dependencies. Such models not only broaden the extrapolation of the experimental result but provide predictive tools for designing microstructure by optimising the process. The first model was developed to correlate the quadratic coefficien "a" of the secondorder polynomial, which describes the average melt pool profile, with the Volumetric Energy Density (VED) applied during processing. The coefficent "a" quantifies the curvature of the melt pool: higher values correspond to a more pronounced concavity, i.e, deeper and narrower melt pools, qhile lower values are associated with flatter profiles. In the first attempt, only the three cubic samples 28, 29 and 30 were considered. As observed in Figure 43, the regression model calculated on this lower number of points provided a coefficient of determination  $R^2$ 0.6485 corresponding to a rather weak predictive capacity. Even if the observation showed a positive trend between "a" and VED, the lower number of points rendered the model less trustworthy. To further strengthen the correlation, two additional cubic samples (17 and 7) were incorporated in the analysis. The resulting new regression shown in Figure 44 shows a remarkable increase in the reliability such that  $R^2 = 0.9416$ . This clearly demonstrates the systematic increment in the quadratic coefficient "a" with VED. From the physical perspective, the behavior conforms to the thermal mechanisms that dictate melt pool evolution. When the VED increases, the entire energy delivered by volume widens and causes larger melt pool depths and larger penetration depths at the substrate layers. On the other hand, the lateral spreading does not scale proportionally and causes the melt pool to be relatively narrow. The outcome causes the increasing curvature of the profile described by a larger coefficient "a".

Moreover, higher values of the VED reflect larger thermal gradients along the direction of the build and reinforce the evolution of parabolic and deep melt pools.

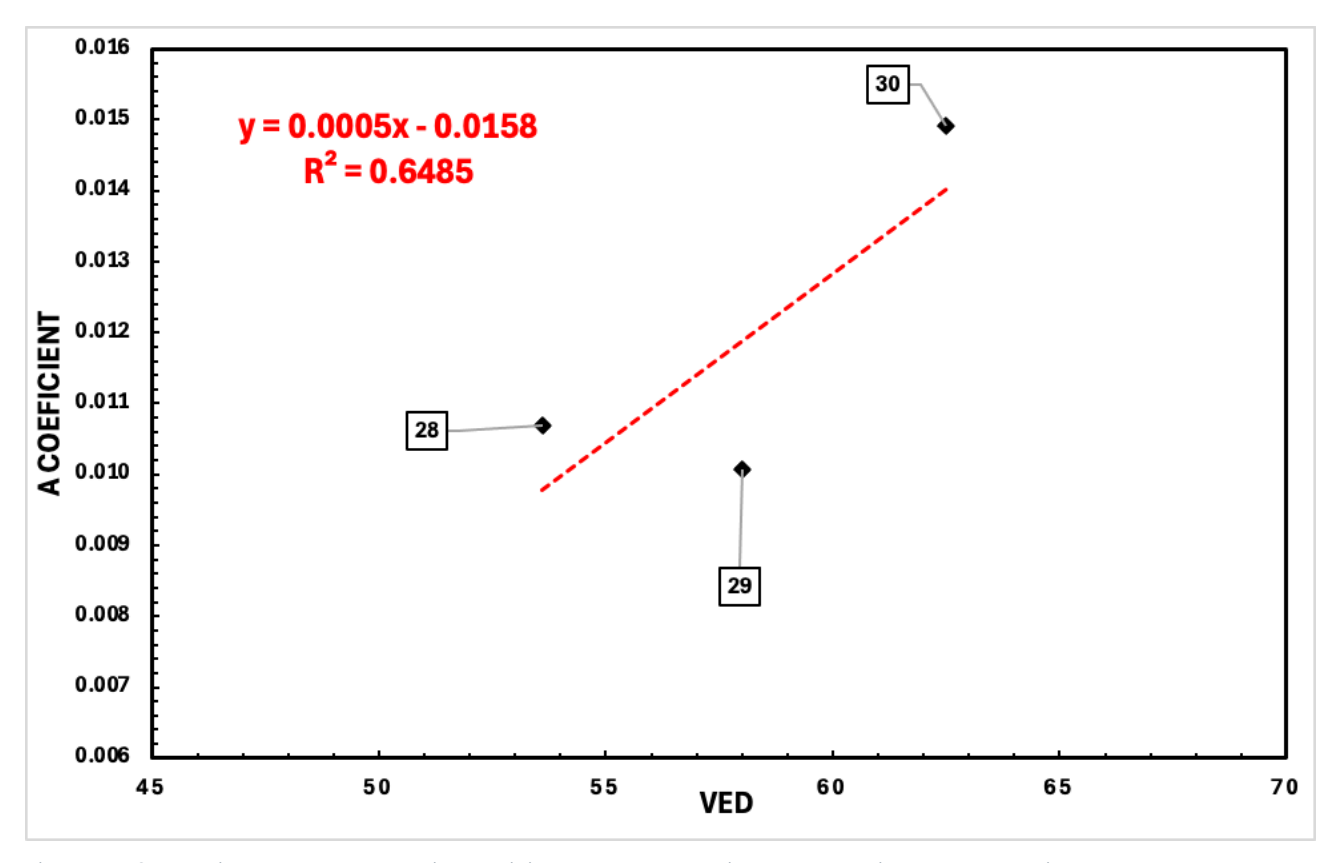


Figure 43: Correlation between quadratic coefficient a and volumetric energy density (VED) for cubic samples 28, 29, and 30. The regression shows a positive trend but limited reliability ( $R^2 = 0.6485$ ).

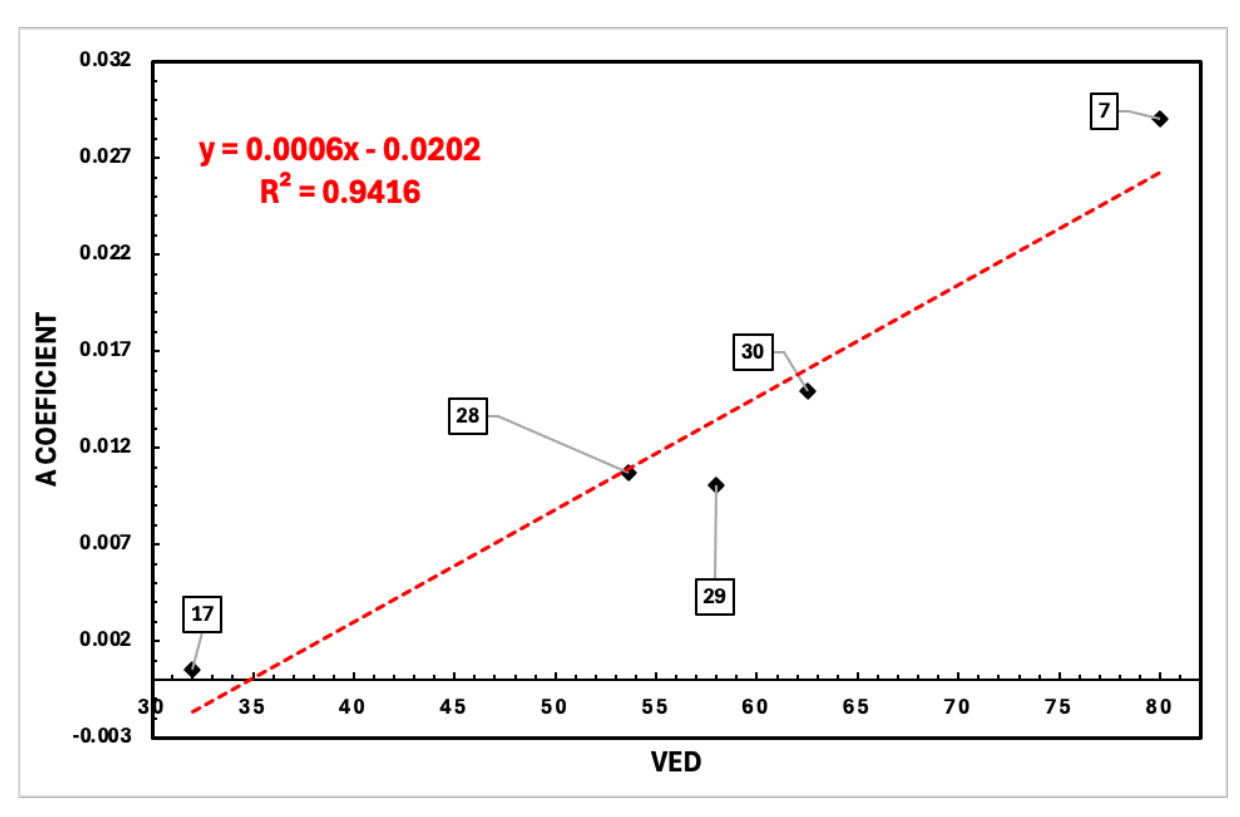


Figure 44: Correlation between quadratic coefficient a and volumetric energy density (VED) for cubic samples 28, 29, 30, 7 and 17. The regression quality improves significantly (R<sup>2</sup> = 0.9416), confirming the robustness of the model.

Following the analysis of the quadratic coefficient "a", a second model was developed to correlate the width-to-depth ratio (W/D) of the melt pool with the Volumetric Energy Density (VED). This approach is complementary to the previous one since the coefficient "a" gives the curvature of the melt pool's profile, the ratio (W/D) defines directly the geometric proportions and offers a more natural way to describe the balance relationship between the lateral expansion and the penetration depth. The regression found on the basis of the five cubic sample (28, 29, 30, 7 and 17) (Figure 45) shows a clear negative correlation between the ratio (W/D) and the VED, the coefficient of determination amounts to  $R^2 = 0.9705$ . This very high coefficient confirms the robustness of the model and defines the fact that the ratio (W/D) tends systematically to decrease when the VED increases. From a physical perspective, this behavior reflects the development of melt pool morphology with increasing energy supply. At lower values of VED, the melt pool forms with restricted penetration and larger lateral extendion, yielding high W/D ratios usually greater than 3. When the VED continues to rise, the larger energy density stimulates deeper melting through the substrate and support layers while the lateral extendion does not develop proportionally. The melt pool then reduces in breadth and deepens such that the resulting W/D ratio values decrease progressively and approach 1 at the very highest VED examined. This change interprets the essential shift in the nature of the melting process from the predominance of conduction-dominated melting, whereby energy diffusion takes the lateral route most favored by the process geometry, to the development essentially of keyhole-like melting behavior in which the concentration of energy along the vertical axis stimulates greater penetration. The linear relation seen thus provides a reliable and physically meaningful account of the manner by which energy density dictates melt pool geometry.

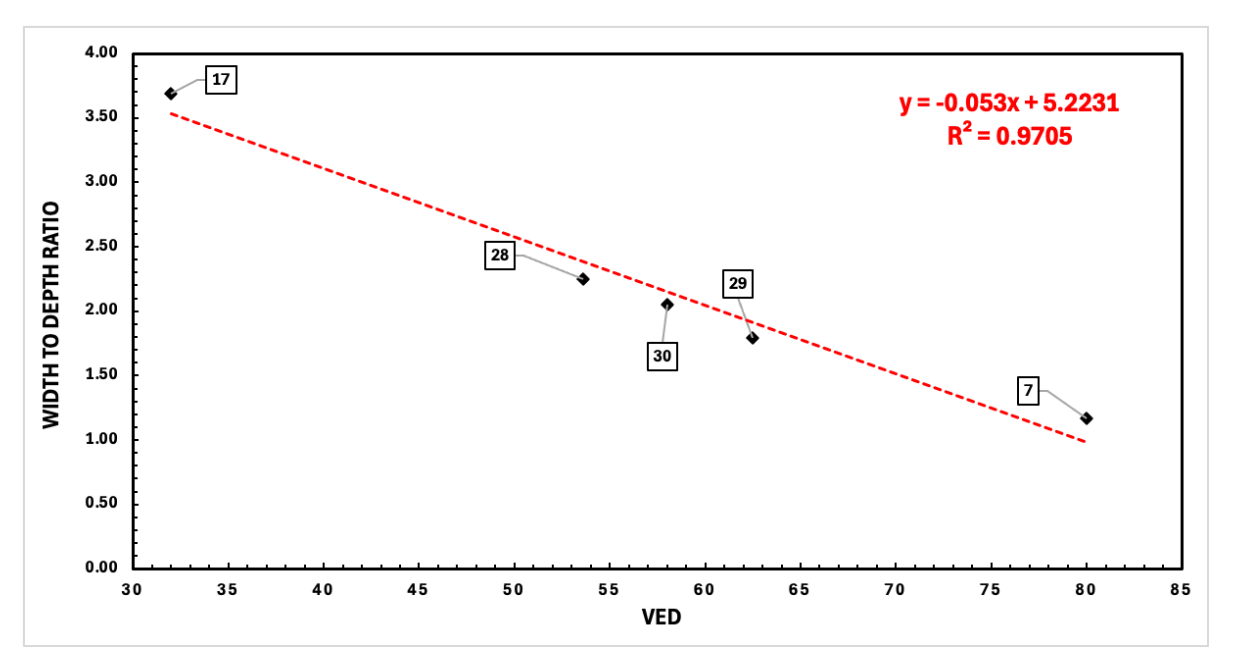


Figure 45: Correlation between melt pool width-to-depth ratio and VED for samples 28, 29, 30, 7, and 17. A strong negative trend is observed ( $R^2 = 0.9705$ ), indicating deeper and narrower pools at higher VED.

The analysis may be extended by considering a third model that consisted in the correlation of the mean quadratic coefficient a and the Linear Energy density (LED). Differently than the VED-based models the correlation resulted statistically weak since the lower coefficient of determination shown by the Figure 56 attestes. The regression line does not mark the data variability and the diffusely spread points indicate that LED alone cannot be a good melt pool curvature descriptor. The model weakness may be explained by the physical meaning of LED. Defined as the ratio between laser power and scanning speed LED provides the energy input per unit length of scan track. However it neglects two major process variables: hatch spacing and lalyer thickness. Such parameters affect strongly the energy distribution inside the melt volume and control both the lateral diffusion and the melt pool penetrataion deepness. Consequently LED provides only a one dimensional approximation for the energy put in and not extending to the three dimensional trasfer condition that both dominate the melt pool morphology. This semplification justifies the fact the the regresion does not drive for a

significant trend and that the values are not the best. The result also shows the evidence of a fundamental conceptual difference: LED may be used in order to compare scanning methods at constant hatch spacing and lalyer thickness values. However it cannot fit the case when such parameters change and cannot predict the meltl pool curvature evolution provided by changing different process. The poor performance by the a-LED model then shows the fact that volumetric descriptors such as VED must be utilised in order to obtain robust correlation and melt pool geometry.

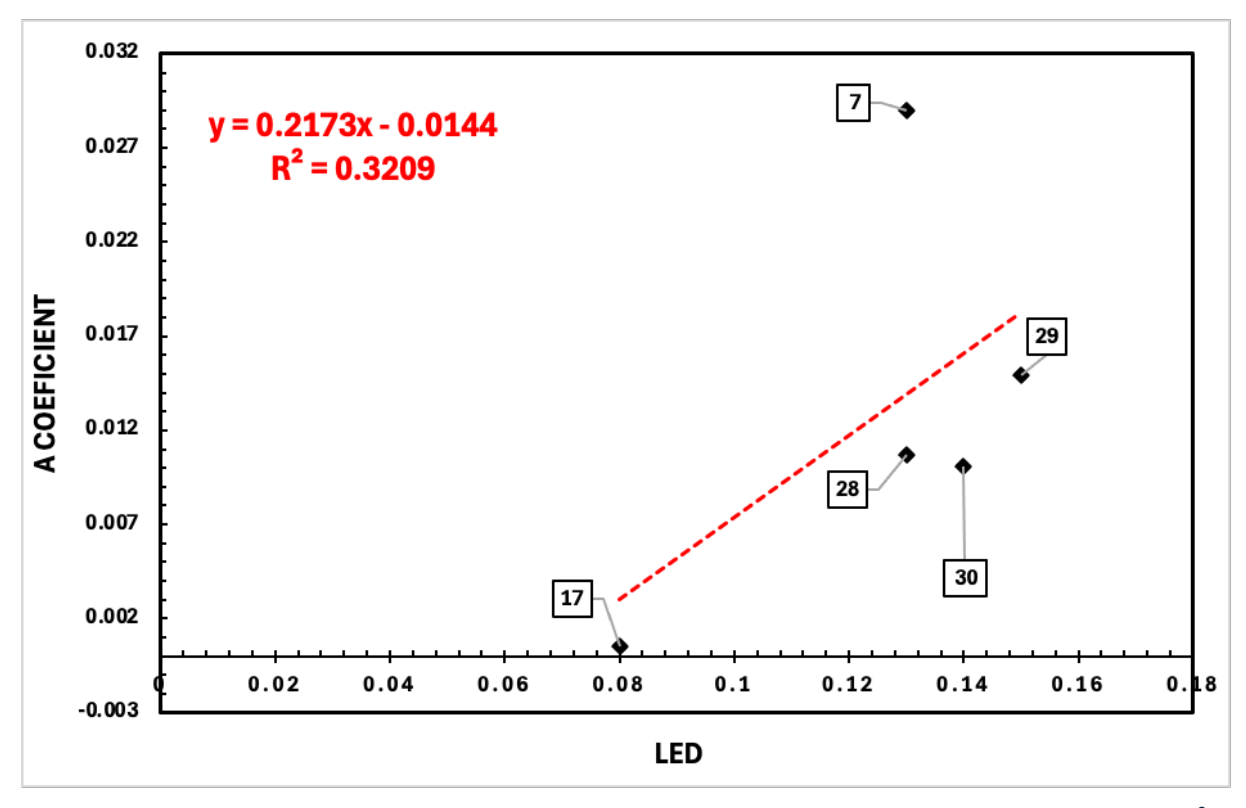


Figure 46: Correlation between quadratic coefficient a and linear energy density (LED). The low regression quality ( $R^2 = 0.3209$ ) highlights the inadequacy of LED as a predictor of melt pool curvature.

A fourth attempt was made to correlate the average quadratic coefficient a, describing the curvature of the melt pool profile, with the applied laser power (W). The regression only yields a coefficient of determination  $R^2 = 0.3192$  (Figure 47), indicating the predictive accuracy is exceedingly bad. Though the regression slope shows weak positive tendency, the widespread scattering in the experiment points evidently demonstrates laser power cannot adequately account for the melt pool geometry variations. Power put in by the laser reflects the natural energy source in the process, but it constitutes only part of the energy balance that typifies the melt pool. Melt pool shape and, critically, curvature specified by the coefficient a are governed by the distribution of supplied power onto the surface that is being scanned and through the

build volume. Scanning speed and hatch spacing and resulting layer thickness in particular govern such distribution by controlling the effective energy per unit volume. Power, then, cannot by itself be said to explain the melt pool depth-to-width ratio or curvature. For instance, the increase in power can allow for larger melt pool penetration and if not complemented by the corresponding change in the scanning speed, the effect can be excessive energy delivery and anomalous melt dynamics in the keyhole or spattering porosity. But when the power increases and the scanning and hatch spacings are varied too, the net volumetric energy input can be held effectively constant and melt pools of similarly curved shapes are obtained. This explains why for the samples produced at similar values for the power, the resulting values for the a coefficient may be very different by looking at the scattering of the experimental points.

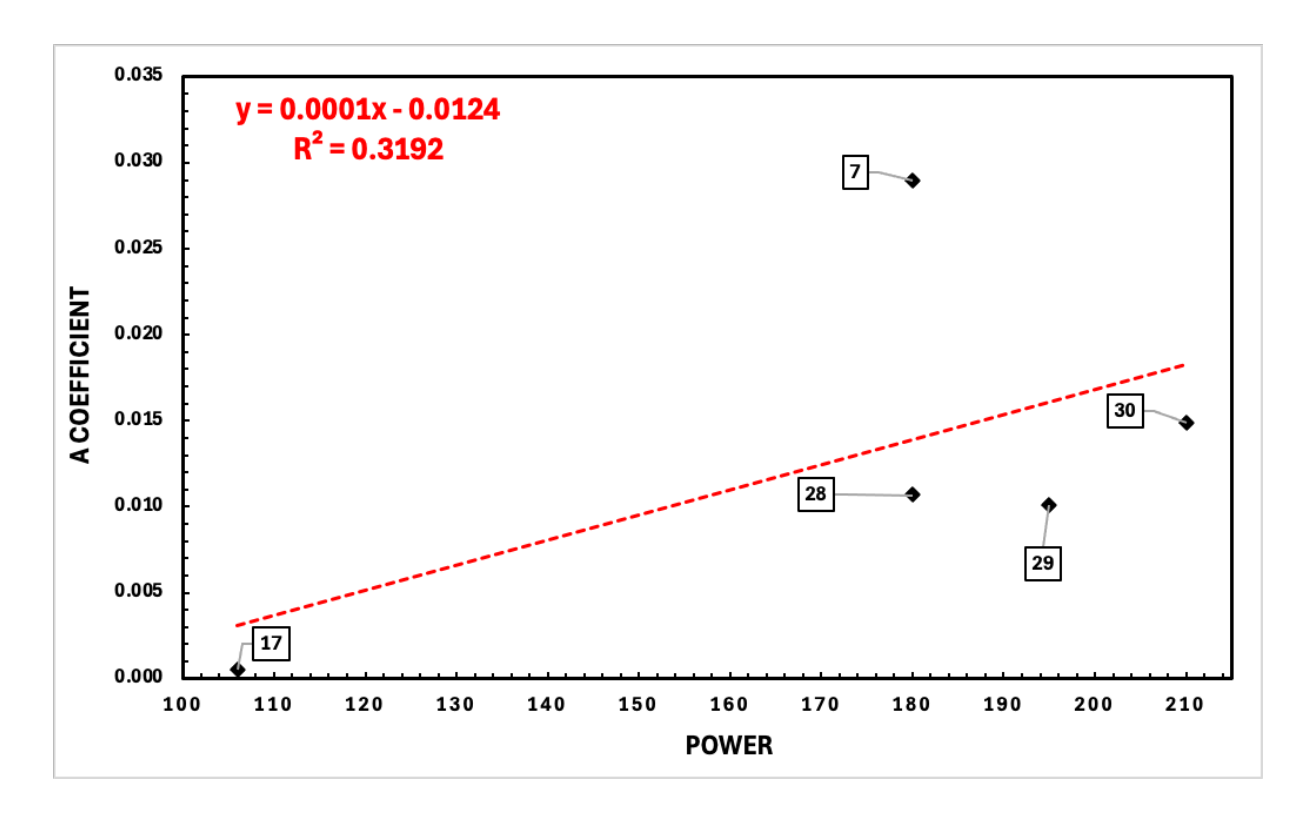


Figure 47: Correlation between quadratic coefficient a and laser power. The weak regression ( $R^2$  = 0.3192) confirms that power alone is not sufficient to describe melt pool geometry.

## **Chapter 5. Conclusion**

The experimental campaign conducted in this study provided a comprehensive overview of microstructural evolution in both cubic (standard) and coal cart-shaped (complex geometry) samples manufactured using LPBF, under various processing and post-processing conditions. The discussion is structured into two complementary parts: a qualitative description of the observed microstructural features, and a quantitative analysis aimed at developing predictive models linking process parameters with melt pool geometry.

From a phenomenological standpoint, the porosity analysis revealed clear correlations between wall thickness, processing condition, and defect morphology. In the cubic samples (28, 29, 30), defects appeared in the form of gas pores and lack-of-fusion defects, with morphology varying depending on the observation plane. Porosity is significantly affectd by the metallurgical orientation. More specifically pores appear to be more elongated along the build direction, while in others, they show more spherical shapes. This difference in defects shape may introduce different mechanical resistance along the metallurgical orientations leading to mechanical anisotropy. This feature may be mainly impactant during crack propagation. In terms of pore size and distribution, samples 28 and 29 contained finer and more uniform pores, while sample 30 shows a broader range of defect sizes, indicating less uniform melting and solidification conditions.

The analysis of the coal cart samples further highlighted the combined effects of geometry and post-processing treatments. In sample 39 (as-built), porosity was considerably higher in thin walls compared to thick walls, a trend also observed in samples 37 (HIP) and 32 (HIP + Solution Heat Treatment + Aging). The HIP treatment significantly reduced both the size and variability of pores. In the fully treated condition, the pore population was further refined, yielding small. After the heat treatment pores were mostly spherical in both orientations and homogeneously dispersed. From the comparison of the three samples, it clearly appears that HIP is particularly effective in closing elongated pores making them more spherical which is indeed a big improvement especially for fatigue resistance. On the other hand, the heat treatment leads to a very stable microstructure containing a balanced mixture of fine gamma prime and carbides.

Secondly, grain size analysis, carried out using optical microscopy, SEM, and EBSD, provided additional insights. In the as-built condition, both cubic and coal cart samples displayed columnar grains aligned with the build direction, characterized by a cellular substructure and elemental segregation at melt pool boundaries. HIP promoted a partial recrystallization and some grain coarsening. This was particularly evident in the XY plane. The additional solution annealing and aging treatments applied to sample 32 further refined the microstructure, producing larger equiaxial grains with a more uniform distribution. Furthermore, EBSD maps confirmed high misorientation and residual stress levels in the as-built samples, which were gradually reduced in the HIP-treated and fully treated samples. This phenomenon is consistent with stress relaxation and defect healing during this post-processing.

SEM observations of precipitates revealed the presence of Hf-rich carbo-oxides in all the observed conditions. This element preferentially was segregating preferentially at melt pool or grain boundaries. More specifically, in the HIP-only samples,  $\gamma'$  precipitates exhibited fan-like shape due to the lower cooling rate, whereas in the fully heat-treated state, they changed to cuboidal shape. The formation of Ta carbides in the most advanced treatment condition further emphasized the role of heat treatments in promoting precipitation phenomena.

In this thesis work some quantitative anlysis were performed, more specifically, four models were evaluated. The first, correlating the quadratic coefficient a with VED, showed a strong positive trend when additional data points were included, with  $R^2$  values above 0.94. This indicates that higher volumetric energy densities lead to deeper, narrower melt pools with more pronounced curvature—consistent with increased penetration and vertical heat flow. The second model, which linked the width-to-depth (W/D) ratio to VED, also showed a strong negative correlation ( $R^2 \approx 0.97$ ). This confirmed that increasing VED reduces the W/D ratio, indicating a transition from conduction-dominated melting (wide and shallow pools) to keyhole-like melting regimes (deep and narrow pools).

Finally, porosity and grain morphology are strongly influenced by both geometry and post-processing: thinner walls are more prone to defects, and HIP is highly effective in reducing them. Secondly, melt pool morphology can be effectively described by our VED-based models. On the other hand, single parameters such as LED and Power purely relates with melt pool morphology.

In conclusion, this integrated phenomenological—quantitative approach highlights that a proper understanding and control of LPBF microstructures can only be achieved by combining direct experimental observations with predictive modeling. The findings demonstrate that a robust microstructural design requires moving beyond single parameters such as power or scan speed, and instead adopting volumetric descriptors that more faithfully capture the underlying process physics. This dual strategy provides both a deep understanding of microstructural phenomena and a practical framework for tailoring process conditions to optimize material integrity.

### **BIBLIOGRAFIA**

- [1] B. Blakey-Milner *et al.*, "Metal additive manufacturing in aerospace: A review," *Mater Des*, vol. 209, Nov. 2021, doi: 10.1016/j.matdes.2021.110008.
- [2] G. J. R. B. A. D. I. G. T. P. H. R. L. X. M. A. S. G. P. W.-S. A. Ott E. A., "Superalloy 718 and Derivatives Proceedings of the 7th International Symposium on Superalloy 718 and Derivatives, October 10-13, 2010 Pittsburgh, PA," 2010, *The Minerals, Metals & Materials Society (TMS)*. [Online]. Available: https://app.knovel.com/hotlink/khtml/id:kt011OOMV4/superalloy-718-derivatives/superalloy-introduction
- [3] J. R. . Davis, Nickel, cobalt, and their alloys. ASM International, 2000.
- [4] C. Varvenne, G. P. M. Leyson, M. Ghazisaeidi, and W. A. Curtin, "Solute strengthening in random alloys," *Acta Mater*, vol. 124, pp. 660–683, Feb. 2017, doi: 10.1016/J.ACTAMAT.2016.09.046.
- [5] M. J. Donachie and S. J. Donachie, *Superalloys: A Technical Guide*. ASM International, 2002. doi: 10.31399/asm.tb.stg2.9781627082679.
- [6] X.-X. Wu and C.-Y. Wang, "Influence of alloying elements upon the theoretical tensile strength of Ni-based model superalloy: γ-Ni/γ'-Ni3Al multilayer," *Comput Mater Sci*, vol. 119, pp. 120–129, 2016, doi: https://doi.org/10.1016/j.commatsci.2016.04.001.
- [7] A. Jena, S. E. Atabay, A. Gontcharov, P. Lowden, and M. Brochu, "Laser powder bed fusion of a new high gamma prime Ni-based superalloy with improved weldability," *Mater Des*, vol. 208, p. 109895, 2021, doi: https://doi.org/10.1016/j.matdes.2021.109895.
- [8] B. Geddes, H. Leon, and X. Huang, *Superalloys: Alloying and Performance*. ASM International, 2010. doi: 10.31399/asm.tb.sap.9781627083133.
- [9] T. M. Pollock and S. Tin, "Nickel-Based Superalloys for Advanced Turbine Engines: Chemistry, Microstructure and Properties," *J Propuls Power*, vol. 22, no. 2, pp. 361–374, 2006, doi: 10.2514/1.18239.
- [10] G. Ganji Dileep Kumar and Rajyalakshmi, "Influence of Alloying Compositions on the Properties of Nickel-Based Superalloys: A Review," in *Recent Advances in Mechanical Engineering*, P. K. Kumar Harish and Jain, Ed., Singapore: Springer Singapore, 2020, pp. 537–555.
- [11] R. Nunes et al., "Volume 2 Publication Information and Contributors."
- [12] J. Belan, "GCP and TCP Phases Presented in Nickel-base Superalloys," *Mater Today Proc*, vol. 3, no. 4, pp. 936–941, 2016, doi: https://doi.org/10.1016/j.matpr.2016.03.024.
- [13] S. Birosca and S. Kolisnychenko, *Superalloys II* . in Specialized Collections; Volume 11. Baech, Switzerland: Trans Tech Publications Ltd, 2020.
- [14] B.H. Kear, Scientific American . 1986.
- [15] L. H. X. Geddes Blaine, *Superalloys Alloying and Performance*. ASM International, 2010. [Online]. Available: https://app.knovel.com/hotlink/toc/id:kpSAP0000H/superalloys-alloying
- [16] A. Tomaszewska, "Primary microstructure characterization of Co-20Ni-9Al-7W-3Re-2Ti superalloy," *Journal of Mining and Metallurgy, Section B: Metallurgy*, vol. 58, no. 1, pp. 43–49, Jan. 2022, [Online]. Available: https://aseestant.ceon.rs/index.php/jmm/article/view/31234
- [17] R. T. Holt, W. Wallace, T. Nb, Ai·, and T. F. Fe, "Impurities and trace elements in nickel-base superalloys," *International Metals Reviews*, vol. 21, pp. 1–24, 1976, [Online]. Available: https://api.semanticscholar.org/CorpusID:136697806

- [18] B. Blakey-Milner *et al.*, "Metal additive manufacturing in aerospace: A review," *Mater Des*, vol. 209, p. 110008, 2021, doi: https://doi.org/10.1016/j.matdes.2021.110008.
- [19] D. Herzog, V. Seyda, E. Wycisk, and C. Emmelmann, "Additive manufacturing of metals," *Acta Mater*, vol. 117, pp. 371–392, 2016, doi: https://doi.org/10.1016/j.actamat.2016.07.019.
- [20] F. Kerstens, A. Cervone, and P. Gradl, "End to end process evaluation for additively manufactured liquid rocket engine thrust chambers," *Acta Astronaut*, vol. 182, pp. 454–465, 2021, doi: https://doi.org/10.1016/j.actaastro.2021.02.034.
- [21] H. Bikas, P. Stavropoulos, and G. Chryssolouris, "Additive manufacturing methods and modelling approaches: a critical review," *The International Journal of Advanced Manufacturing Technology*, vol. 83, no. 1, pp. 389–405, 2016, doi: 10.1007/s00170-015-7576-2.
- [22] H. C. Zhou Kun, *Metal Powder-Based Additive Manufacturing*. John Wiley & Sons, 2023. [Online]. Available: https://app.knovel.com/hotlink/toc/id:kpMPBAM001/metal-powder-based-additive/metal-powder-based-additive
- [23] P. D. Enrique, T. Minasyan, and E. Toyserkani, "Laser powder bed fusion of difficult-to-print γ' Ni-based superalloys: a review of processing approaches, properties, and remaining challenges," *Addit Manuf*, p. 104811, 2025, doi: https://doi.org/10.1016/j.addma.2025.104811.
- [24] S. CS. Prager M, Welding of Precipitation-Hardening Nickel-Base Alloys. . 1968.
- [25] C. E. Cross, "On the Origin of Weld Solidification Cracking," in *Hot Cracking Phenomena in Welds*, H. Böllinghaus Thomas and Herold, Ed., Berlin, Heidelberg: Springer Berlin Heidelberg, 2005, pp. 3–18. doi: 10.1007/3-540-27460-X 1.
- [26] S. Kou, "Solidification and liquation cracking issues in welding," *JOM*, vol. 55, no. 6, pp. 37–42, 2003, doi: 10.1007/s11837-003-0137-4.
- [27] "Weld Metal Solidification Cracking," in *Welding Metallurgy*, John Wiley & Sons, Ltd, 2002, ch. 11, pp. 263–300. doi: https://doi.org/10.1002/0471434027.ch11.
- [28] John N. Dupont, John C. Lippold, and Samuel D. Kiser, *Welding Metallurgy and Weldability of Nickel-Base Alloys* . 2009.
- [29] C. Qiu *et al.*, "Influence of processing conditions on strut structure and compressive properties of cellular lattice structures fabricated by selective laser melting," *Materials Science and Engineering: A*, vol. 628, pp. 188–197, 2015, doi: https://doi.org/10.1016/j.msea.2015.01.031.
- [30] H. Attar, M. Calin, L. C. Zhang, S. Scudino, and J. Eckert, "Manufacture by selective laser melting and mechanical behavior of commercially pure titanium," *Materials Science and Engineering: A*, vol. 593, pp. 170–177, 2014, doi: https://doi.org/10.1016/j.msea.2013.11.038.
- [31] A. V Gusarov, I. Yadroitsev, Ph. Bertrand, and I. Smurov, "Heat transfer modelling and stability analysis of selective laser melting," *Appl Surf Sci*, vol. 254, no. 4, pp. 975–979, 2007, doi: https://doi.org/10.1016/j.apsusc.2007.08.074.
- [32] S. A. Khairallah, A. T. Anderson, A. Rubenchik, and W. E. King, "Laser powder-bed fusion additive manufacturing: Physics of complex melt flow and formation mechanisms of pores, spatter, and denudation zones," *Acta Mater*, vol. 108, pp. 36–45, 2016, doi: https://doi.org/10.1016/j.actamat.2016.02.014.
- [33] S. Pang, W. Chen, J. Zhou, and D. Liao, "Self-consistent modeling of keyhole and weld pool dynamics in tandem dual beam laser welding of aluminum alloy," *J Mater Process Technol*, vol. 217, pp. 131–143, 2015, doi: https://doi.org/10.1016/j.jmatprotec.2014.11.013.
- [34] B. Li, J. Du, Y. Sun, S. Zhang, and Q. Zhang, "On the importance of heat source model determination for numerical modeling of selective laser melting of IN625," *Opt Laser*

- *Technol*, vol. 158, p. 108806, 2023, doi: https://doi.org/10.1016/j.optlastec.2022.108806.
- [35] S. A. Khairallah, A. T. Anderson, A. Rubenchik, and W. E. King, "Laser powder-bed fusion additive manufacturing: Physics of complex melt flow and formation mechanisms of pores, spatter, and denudation zones," *Acta Mater*, vol. 108, pp. 36–45, 2016, doi: https://doi.org/10.1016/j.actamat.2016.02.014.
- [36] M. J. Matthews, G. Guss, S. A. Khairallah, A. M. Rubenchik, P. J. Depond, and W. E. King, "Denudation of metal powder layers in laser powder bed fusion processes," *Acta Mater*, vol. 114, pp. 33–42, 2016, doi: https://doi.org/10.1016/j.actamat.2016.05.017.
- [37] S. Das, "Physical Aspects of Process Control in Selective Laser Sintering of Metals," *Adv Eng Mater*, vol. 5, no. 10, pp. 701–711, 2003, doi: https://doi.org/10.1002/adem.200310099.
- [38] W. E. King *et al.*, "Observation of keyhole-mode laser melting in laser powder-bed fusion additive manufacturing," *J Mater Process Technol*, vol. 214, no. 12, pp. 2915–2925, 2014, doi: https://doi.org/10.1016/j.jmatprotec.2014.06.005.
- [39] Y. Lee, M. Nordin, S. S. Babu, and D. F. Farson, "Effect of Fluid Convection on Dendrite Arm Spacing in Laser Deposition," *Metallurgical and Materials Transactions B*, vol. 45, no. 4, pp. 1520–1529, 2014, doi: 10.1007/s11663-014-0054-7.
- [40] W. Kurz, B. Giovanola, and R. Trivedi, "Theory of microstructural development during rapid solidification," *Acta Metallurgica*, vol. 34, no. 5, pp. 823–830, 1986, doi: https://doi.org/10.1016/0001-6160(86)90056-8.
- [41] S. Kou and John Wiley & Sons, "Welding Metallurgy 2nd edition," 2003.
- [42] A. Saboori, A. Aversa, G. Marchese, S. Biamino, M. Lombardi, and P. Fino, "Microstructure and Mechanical Properties of AISI 316L Produced by Directed Energy Deposition-Based Additive Manufacturing: A Review," *Applied Sciences*, vol. 10, no. 9, 2020, doi: 10.3390/app10093310.
- [43] D. Dai and D. Gu, "Effect of metal vaporization behavior on keyhole-mode surface morphology of selective laser melted composites using different protective atmospheres," *Appl Surf Sci*, vol. 355, pp. 310–319, 2015, doi: https://doi.org/10.1016/j.apsusc.2015.07.044.
- [44] B. AlMangour, D. Grzesiak, and J.-M. Yang, "Selective laser melting of TiB2/316L stainless steel composites: The roles of powder preparation and hot isostatic pressing post-treatment," *Powder Technol*, vol. 309, pp. 37–48, 2017, doi: https://doi.org/10.1016/j.powtec.2016.12.073.
- [45] L. Sheridan, J. E. Gockel, and O. E. Scott-Emuakpor, "Primary Processing Parameters, Porosity Production, and Fatigue Prediction for Additively Manufactured Alloy 718," J Mater Eng Perform, vol. 28, no. 9, pp. 5387–5397, 2019, doi: 10.1007/s11665-019-04305-7.
- [46] J. Risse, "Additive Manufacturing of Nickel-Base Superalloy IN738LC by Laser Powder Bed Fusion," 2019.
- [47] L. N. Carter *et al.*, "Process optimisation of selective laser melting using energy density model for nickel based superalloys," *Materials Science and Technology*, vol. 32, no. 7, pp. 657–661, 2016, doi: 10.1179/1743284715Y.0000000108.
- [48] G. Marchese *et al.*, "The Influence of the Process Parameters on the Densification and Microstructure Development of Laser Powder Bed Fused Inconel 939," *Metals (Basel)*, vol. 10, no. 7, 2020, doi: 10.3390/met10070882.
- [49] L. N. Carter, C. Martin, P. J. Withers, and M. M. Attallah, "The influence of the laser scan strategy on grain structure and cracking behaviour in SLM powder-bed fabricated nickel superalloy," *J Alloys Compd*, vol. 615, pp. 338–347, 2014, doi: https://doi.org/10.1016/j.jallcom.2014.06.172.

- [50] M. Vilanova, F. Garciandia, S. Sainz, D. Jorge-Badiola, T. Guraya, and M. San Sebastian, "The limit of hot isostatic pressing for healing cracks present in an additively manufactured nickel superalloy," *J Mater Process Technol*, vol. 300, p. 117398, 2022, doi: https://doi.org/10.1016/j.jmatprotec.2021.117398.
- [51] X. Hu *et al.*, "Liquid-induced healing of cracks in nickel-based superalloy fabricated by laser powder bed fusion," *Acta Mater*, vol. 267, p. 119731, 2024, doi: https://doi.org/10.1016/j.actamat.2024.119731.
- [52] K.-S. Kim, S. Yang, M.-S. Kim, and K.-A. Lee, "Effect of post heat-treatment on the microstructure and high-temperature oxidation behavior of precipitation hardened IN738LC superalloy fabricated by selective laser melting," *J Mater Sci Technol*, vol. 76, pp. 95–103, 2021, doi: https://doi.org/10.1016/j.jmst.2020.11.013.
- [53] K. Miao *et al.*, "Mechanisms of Heat-Treatment-Induced Cracking in Additively Manufactured IN738 Alloy," *Materials*, vol. 16, no. 23, 2023, doi: 10.3390/ma16237316.
- [54] R. Engeli, T. Etter, S. Hövel, and K. Wegener, "Processability of different IN738LC powder batches by selective laser melting," *J Mater Process Technol*, vol. 229, pp. 484–491, 2016, doi: https://doi.org/10.1016/j.jmatprotec.2015.09.046.
- [55] M. Cloots, P. J. Uggowitzer, and K. Wegener, "Investigations on the microstructure and crack formation of IN738LC samples processed by selective laser melting using Gaussian and doughnut profiles," *Mater Des*, vol. 89, pp. 770–784, 2016, doi: https://doi.org/10.1016/j.matdes.2015.10.027.
- [56] Zhengrong Yu, Xianfei Ding, Lamei Cao, Yunrong Zheng, and Qiang Feng, " Transient liquid phase bonding of second and third generation ni-based single crystal superalloy with hf-containing interlayer alloy," 2016.
- [57] Yunrong Zheng, Behaviour of Hf in solidification of cast Ni-base superalloys. 1986.
- [58] Z. Yu *et al.*, "The effect of Hf on solidification cracking inhibition of IN738LC processed by Selective Laser Melting," *Materials Science and Engineering: A*, vol. 804, p. 140733, 2021, doi: https://doi.org/10.1016/j.msea.2021.140733.
- [59] Siemens Energy, "Nickel-based superalloy SAM chemical composition".